

AD-A208 647

THIS FILE COPY

4

SMALL SCALE MODEL TESTS IN
SMALL WIND AND WATER TUNNELS AT HIGH
INCIDENCE AND PITCH RATES

VOLUME I - TEST PROGRAM AND
DISCUSSION OF RESULTS

Atlee M. Cunningham, Jr.
Todd Bushlow
John R. Mercer
Tim A. Wilson
Steve N. Schwoerke

GENERAL DYNAMICS
Fort Worth Division

Contract Number N00014-85-C-0419

DTIC
ELECTE
JUN 05 1989
S D & D

April 1989

FINAL REPORT

DISTRIBUTION STATEMENT A

Approved for public release;
Distribution Unlimited

Prepared For The
OFFICE OF NAVAL RESEARCH

89 6 02 095

SMALL SCALE MODEL TESTS IN
SMALL WIND AND WATER TUNNELS AT HIGH
INCIDENCE AND PITCH RATES

VOLUME I - TEST PROGRAM AND
DISCUSSION OF RESULTS

Atlee M. Cunningham, Jr.
Todd Bushlow
John R. Mercer
Tim A. Wilson
Steve N. Schwoerke

GENERAL DYNAMICS
Fort Worth Division

Contract Number N00014-85-C-0419

April 1989

FINAL REPORT

Prepared For The
OFFICE OF NAVAL RESEARCH

Unclassified

SECURITY CLASSIFICATION OF THIS PAGE

ADA208647

REPORT DOCUMENTATION PAGE				Form Approved OMB No. 0704-0188	
1a. REPORT SECURITY CLASSIFICATION Unclassified			1b. RESTRICTIVE MARKINGS None		
2a. SECURITY CLASSIFICATION AUTHORITY			3. DISTRIBUTION / AVAILABILITY OF REPORT A		
2b. DECLASSIFICATION / DOWNGRADING SCHEDULE					
4. PERFORMING ORGANIZATION REPORT NUMBER(S)			5. MONITORING ORGANIZATION REPORT NUMBER(S)		
6a. NAME OF PERFORMING ORGANIZATION General Dynamics Fort Worth Division		6b. OFFICE SYMBOL (if applicable)	7a. NAME OF MONITORING ORGANIZATION Office of Naval Research		
6c. ADDRESS (City, State, and ZIP Code) P.O. Box 748 Fort Worth, Texas 76101		7b. ADDRESS (City, State, and ZIP Code) 800 N. Quincy Street Arlington, Virginia 22217			
8a. NAME OF FUNDING / SPONSORING ORGANIZATION Office of Naval Research		8b. OFFICE SYMBOL (if applicable) None	9. PROCUREMENT INSTRUMENT IDENTIFICATION NUMBER N00014-85-C-0419		
8c. ADDRESS (City, State, and ZIP Code) 800 N. Quincy Street Arlington, Virginia 22217		10. SOURCE OF FUNDING NUMBERS			
		PROGRAM ELEMENT NO.	PROJECT NO.	TASK NO.	WORK UNIT ACCESSION NO.
11. TITLE (Include Security Classification) Small Scale Model Tests in Small Wind and Water Tunnels at High Incidence and Pitch Rates, Volume I - Test Program and Discussion of Results					
12. PERSONAL AUTHOR(S) Cunningham, A.M., Jr., Bushlow, T., Mercer, J.R., Wilson, T.A., and Schwoerke, S.N.					
13a. TYPE OF REPORT Final		13b. TIME COVERED FROM 9/1985 TO 9/1988	14. DATE OF REPORT (Year, Month, Day) 1989 April 10		15. PAGE COUNT 145
16. SUPPLEMENTARY NOTATION <i>Keywords:</i>					
17. COSATI CODES			18. SUBJECT TERMS (Continue on reverse if necessary and identify by block number)		
FIELD	GROUP	SUB-GROUP	Aerodynamics; Unsteady Flows; Vortex Flows; Wind Tunnel Testing, Water Tunnel Testing tests, etc.		
19. ABSTRACT (Continue on reverse if necessary and identify by block number)					
<p>The force testing of small-scale models in either a small wind tunnel or a water tunnel was investigated as an inexpensive and quick means to obtain meaningful dynamic force and moment data representative of rapidly maneuvering full-scale aircraft. Force tests of flat-plate semi-span models were conducted in the General Dynamics Aerodynamic Development Facility (ADF) which is a small 14x14 in² low speed wind tunnel. Oscillatory model motions up to 48 in (peak to peak) amplitude were tested at frequencies of 1 to 3 Hz. Force tests of flat and three-dimensional full span models were conducted in the General Dynamics Hydroflow Facility (HFF) which is a horizontal flow water tunnel with a 24x24 in² test section. Pitch/pulse model motions were tested for conditions similar to those tested in the ADF.</p> <p style="text-align: right;">(continued)</p>					
20. DISTRIBUTION / AVAILABILITY OF ABSTRACT <input checked="" type="checkbox"/> UNCLASSIFIED/UNLIMITED <input checked="" type="checkbox"/> SAME AS RPT. <input type="checkbox"/> DTIC USERS			21. ABSTRACT SECURITY CLASSIFICATION Unclassified		
22a. NAME OF RESPONSIBLE INDIVIDUAL Dr. Spiro Lekoudis			22b. TELEPHONE (Include Area Code) (202) 696-4405		22c. OFFICE SYMBOL ONR

19. ABSTRACT (contd.)

ADF. The test velocities were 100 fps in the ADF and 0.8 fps in the HFF which yielded nominal Reynolds numbers of 0.6×10^6 and 0.06×10^6 respectively (based on root chord). Frequencies of motion in the HFF were scaled with velocity to maintain constant non-dimensional frequencies and pitch rates. Thus, frequencies for the HFF tests were nominally 0.01 and 0.03 Hz. Specific objectives of this investigation were: (1) verify static and dynamic force and moment measurements from the small scale tests with results from reliable or multiple sources; (2) determine time history effect for various frequencies, amplitudes, starting angles and peak angles; (3) evaluate the effects of test medium; (4) determine Reynolds number effects; (5) demonstrate the importance of model three-dimensionality; and (6) evaluate the effects of planform geometry variations.

This Volume I presents the test program, correlations with other data, and discussions of the specific objectives of this investigation. In general it was shown that the small scale wind tunnel and water tunnel test techniques do provide reasonable dynamic force and moment data for a wide variety of planforms and conditions.

(to p 1)

FORWARD

The small scale wind and water tunnel tests discussed in this report were sponsored by the Office of Naval Research under Contract Number N00014-85-C-0419 and performed by the Fort Worth Division of General Dynamics. The investigation spanned the period from 16 September 1985 through 15 September 1988. The program was monitored by Dr. Robert E. Whitehead, Dr. T. C. Tai and finally Dr. Spiro Lekoudis all of ONR.

The program manager and principle investigator was Dr. Atlee M. Cunningham, Jr. of the Computational Fluid Dynamics Group who was assisted by Todd Bushlow and Steve Schwoerke of the Aeroanalysis Group as well as Tim Wilson and John Mercer of the Aerospace Technology Labs.



Accession For	
NTIS CRA&I	<input checked="" type="checkbox"/>
DTIC TAB	<input type="checkbox"/>
Unannounced	<input type="checkbox"/>
Justification	
By <i>AB</i>	
Distribution/	
Availability Codes	
Dist	Avail and/or Special
<i>A-1</i>	

TABLE OF CONTENTS

	Page
LIST OF FIGURES	vi
LIST OF TABLES	xiii
1.0 BACKGROUND AND INTRODUCTION	1
2.0 SYMBOLS	4
3.0 TEST PROGRAM	6
3.1 GENERAL DYNAMICS TEST TUNNELS	6
3.2 BALANCE AND SUPPORT SYSTEMS	7
3.3 DATA ACQUISITION PROCEDURES	8
3.4 TEST PLANS	9
3.5 MODELS	10
3.6 TEST PROCEDURES	11
3.7 DATA REDUCTION	14
4.0 TEST RESULTS	17
4.1 DATA BASE FORMAT	17
4.2 VOLUME II - ADF WIND TUNNEL DATA BASE	18
4.3 VOLUME III - HFF WATER TUNNEL DATA BASE	18
5.0 CORRELATIONS WITH LARGE SCALE DATA	20
5.1 STATIC CORRELATIONS	20
5.2 DYNAMIC CORRELATIONS	24
5.2.1 Correlation of Dynamic Normal Force Data	24
5.2.2 Correlation of Dynamic Pitching Moment Data	27

TABLE OF CONTENTS (continued)

	Page
6.0 DISCUSSION OF RESULTS	30
6.1 TIME HISTORY EFFECTS	30
6.2 TEST MEDIUM	35
6.3 REYNOLDS NUMBER EFFECTS	41
6.4 THREE-DIMENSIONAL EFFECTS	44
6.5 PLANFORM EFFECTS	46
7.0 CONCLUSIONS	49
REFERENCES	52
APPENDIX	120

List of Figures

Figure		Page
3-1	General Dynamics Aerodynamic Development Facility (ADF)	54
3-2	General Dynamics Hydroflow Facility (HFF)	55
3-3	ADF Dynamic Drive and Support System For Semi-Span Models	56
3-4	HFF Dynamic Drive and Support System For Full-Span Models	57
3-5	ADF Flat Plate Semi-Span Models	58
3-6	HFF Flat Plate Full Span Models	59
3-7	Three Dimensional and Flat E-7 Models for the HFF	60
3-8	Pitch/Pulse Incidence Time History for Water Tunnel Models at Various Pitch Rates	61
4-1	Time History Presentation of a Pitch/Pulse for the Straked Wing	62
4-2	C_N vs α Presentation of a Pitch/Pulse for the Straked Wing	62
4-3	Multiple Plot Format for Increasing Peak Angles with a Fixed Starting Angle at Two Frequencies	63
4-4	Multiple Plot Format for Increasing Starting Angle with a Fixed Peak Angle at Two Frequencies	64
4-5	Example of the Static Data Format (55° Delta) for Volume II - ADF Wind Tunnel Data Base	65
4-6	Example of the Dynamic Data Format (55° Delta) for Volume II - ADF Wind Tunnel Data Base	66
4-7	Example of the Static Data Format (55° Delta) for Volume II - HFF Water Tunnel Data Base	67

List of Figures (continued)

Figure		Page
4-8	Example of the Dynamic Data Format (55° Delta) for Volume II - HFF Water Tunnel Data Base	68
5-1	Wing Planform and Instrumentation for the NLR Straked Wing Model	69
5-2	Dynamic Drive and Support System for the NLR Model	70
5-3	Comparison of Steady Straked Wing Force and Moment Data for the ADF Test ($R_e = 0.55 \times 10^6$) and NLR Test in Wires ($R_e = 1.4 \times 10^6$)	71
5-4	Comparison of Steady Straked Wing Force and Moment Data for the HFF Test ($R_e = 0.06 \times 10^6$) and NLR Test ($R_e = 4.5 \times 10^6$)	72
5-5	Comparison of Steady 55° Delta Wing Force and Moment Data for the ADF Test ($R_e = 0.45 \times 10^6$), the HFF Test ($R_e = 0.05 \times 10^6$) and Wentz ($R_e = 0.58 \times 10^6$)	73
5-6	Comparison of Steady 70° Delta Wing Force and Moment Data for the ADF Test ($R_e = 0.6 \times 10^6$), HFF Test ($R_e = 0.066 \times 10^6$), Wentz ($R_e = 1.1 \times 10^6$) and Chang and Muirhead ($R_e = 0.7 \times 10^6$)	74
5-7	Comparison of Steady Force and Moment Data for the Small and Large Disks in the HFF Test and the Results from Hoerner	75
5-8	Comparison of Steady 3-D E-7 Force and Moment Data for the HFF Test ($R_e = 0.052 \times 10^6$) and 1/9 - Scale Test ($R_e = 6.5 \times 10^6$)	76
5-9	Comparison of Unsteady Straked Wing Normal Force Data for the ADF and HFF Tests with NLR Results over the Incidence Range of 8° to 40°	77

List of Figures (continued)

Figure		Page
5-10	Comparison of Unsteady Straked Wing Normal Force Data for the ADF and HFF Tests with NLR Results over the Incidence Range of 22° to 42°	78
5-11	Comparison of Unsteady Straked Wing Normal Force Data for the ADF and HFF Tests with NLR Results over the Incidence Range of 24° to 38°	79
5-12	Comparison of Unsteady Straked Wing Normal Force Data for the ADF and HFF Tests with NLR Results over the Incidence Range of 24° to 56°	80
5-13	Comparison of Unsteady Straked Wing Normal Force Data for Two HFF Runs at Different Incidences but of Identical Dynamic Conditions	81
5-14	Comparison of Unsteady Straked Wing Pitching Moment Data for ADF and HFF Tests with Shifted NLR Results Over the Incidence Range of 8° to 40°	82
5-15	Comparison of Unsteady Straked Wing Pitching Moment Data for ADF and HFF Tests with Shifted NLR Results Over the Incidence Range of 22° to 56°	83
6-1	Repeatability of Straked Wing Dynamic Data in the ADF at Two Frequencies	84
6-2	Repeatability of 55° Delta Dynamic Data in the ADF at Two Frequencies	85
6-3	Repeatability of Straked Wing Dynamic Data in the HFF at Two Frequencies	86
6-4	Repeatability of 55° Delta Dynamic Data in the HFF at Two Frequencies	87
6-5	Comparison of Oscillatory and Pitch/Pulse Normal Force Data for the Straked Wing in the ADF at One Frequency	88

List of Figures (continued)

Figure		Page
6-6	Effect of Frequency for the Straked Wing in ADF and HFF Tests	89
6-7	Effect of Frequency for the 55° Delta in ADF and HFF Tests	90
6-8	Effect of Frequency for the 70° Delta in ADF and HFF Tests	91
6-9	Effect of Frequency for the 70°/30° Cranked Wing in ADF and HFF Tests	92
6-10	Effect of Peak Angle for a Fixed Starting Angle in ADF Tests of the Straked Wing	93
6-11	Effect of Starting Angle for a Fixed Peak Angle in ADF Tests of the Straked Wing	94
6-12	Effect of Peak Angle for a Fixed Starting Angle in ADF Tests of the 70°/30° Cranked Wing	95
6-13	Effect of Starting Angle for a Fixed Peak Angle in ADF Tests of the 70°/30° Cranked Wing	96
6-14	Time History Effects in ADF Tests of the Straked Wing at Similar $\bar{\alpha}$ Values and an Incidence Range of 8° to 56°	97
6-15	Time History Effects in HFF Tests of the Straked Wing at Similar $\bar{\alpha}$ Values and an Incidence Range of 8° to 56°	98
6-16	Time History Effects in HFF Tests of the Straked Wing at Similar $\bar{\alpha}$ Values and an Incidence Range of 16° to 64°	99
6-17	Comparison of HFF Data at High Amplitude and Frequency with NLR Results (Ref. 5) at Similar $\bar{\alpha}$ Values at Two Frequencies	100
6-18	Time History of Pitching Moment for an 86.2 sec Pitch/Pulse of the Straked Wing in the HFF for V = 0 FPS	101

List of Figures (continued)

Figure		Page
6-19	Time History of Pitching Moment for a 28.7 sec Pitch/Pulse of the Straked Wing in the HFF for $V = 0$ FPS	101
6-20	Time History of Pitching Moment for a 15.3 sec Pitch/Pulse of the Straked Wing in the HFF for $V = 0$ FPS	102
6-21	Time History of C_m for an 87.7 sec Pitch/Pulse of the Straked Wing in the HFF for $V = 0.8$ FPS	102
6-22	Time History of C_m for a 30.0 sec Pitch/Pulse of the Straked Wing in the HFF for $V = 0.8$ FPS	103
6-23	Time History of C_m for a 16.7 sec Pitch/Pulse of the Straked Wing in the HFF for $V = 0.8$ FPS	103
6-24	Comparison of Steady ADF and HFF C_N Results for the Straked Wing	104
6-25	Comparison of Steady ADF and HFF C_N Results for the $70^\circ/30^\circ$ Cranked Wing	104
6-26	Comparison of ADF and HFF Results for the Straked Wing at Two Amplitudes and Two Frequencies	105
6-27	Comparison of ADF and HFF Results for the 55° Delta Wing at Two Amplitudes and Two Frequencies	106
6-28	Comparison of ADF and HFF Results for the 70° Delta Wing at Two Amplitudes and Two Frequencies	107
6-29	Comparison of ADF and HFF Results for the $70^\circ/30^\circ$ Cranked Wing at Two Amplitudes and Two Frequencies	108
6-30	Straked Wing Steady Results for NLR Test at Different Speeds and with Different Supports	109

List of Figures (continued)

Figure		Page
6-31	Comparison of Steady HFF Results for the 3-D and Flat Plate E-7 Models	110
6-32	Comparison of Unsteady HFF Results for the 3-D and Flat Plate E-7 Models, $k = 0.0333$	111
6-33	Comparison of Unsteady HFF Results for the 3-D and Flat Plate E-7 Models, $k = 0.0882$	112
6-34	Comparison of Unsteady ADF Results for the 70° and 55° Delta Wings at Two Frequencies - Unshifted	113
6-35	Comparison of Unsteady ADF Results for the 70° and 55° Delta Wings at Two Frequencies - Shifted ($\alpha_{\min} = 8^\circ$ for 55° Delta and $\alpha_{\min} = 16^\circ$ for the 70° Delta)	114
6-36	Comparison of Unsteady HFF Results for the 70° and 55° Delta Wings at Two Frequencies - Shifted ($\alpha_{\min} = 8^\circ$ for 55° Delta and $\alpha_{\min} = 16^\circ$ for 70° Delta)	115
6-37	Comparison of Unsteady ADF Results for the 70° Delta and Cranked Wings at Two Frequencies - Unshifted ($\alpha_{\min} = 8^\circ$)	116
6-38	Comparison of Unsteady HFF Results for the 70° Delta and Cranked Wings at Two Frequencies - Unshifted ($\alpha_{\min} = 16^\circ$) but Shifted in C_N	117
6-39	Comparison of Unsteady ADF and HFF Results for the Straked and 55° Delta Wings at the High Frequency	118
6-40	Comparison of Unsteady ADF and HFF Results for the Straked and 55° Delta Wings at Mixed Frequencies (Low Frequency for 55° Delta and High Frequency for Straked)	119
A-1	Uncorrected HFF Results for the Large Disk as Compared with Hoerner	128

List of Figures (continued)

Figure		Page
A-2	Uncorrected HFF Results for the Small Disk as Compared with Hoerner	129
A-3	Uncorrected HFF Results for the 3-D E-7 Model as Compared with 1/9-Scale Data	130
A-4	Effect of Planform Blockage on Normal Force Measured at 90° in the HFF	131

List of Tables

Table		Page
3-1	Smoke Tunnel Test Conditions	53
A-1	Results for Normal Force Correlations at $\alpha = 90^\circ$ ($V_0 \approx 0.8$ FPS)	126
A-2	Pitching Moment Effects Due to Balance/ Support Interference	127

THIS PAGE LEFT BLANK

1.0 BACKGROUND AND INTRODUCTION

Interest in flying at very high angles of attack beyond the static stall conditions has been kindled by proposals to exploit this flow regime to improve fighter aircraft maneuverability (Refs. 1 and 2). Herbst's concept to fly into the post-stall regime to achieve quicker turns (Ref. 1) and the use of unsteady aerodynamics at high incidence discussed by Lang and Francis (Ref. 2) open a Pandora's box of new aerodynamic problems. Since these ideas require flying at incidences as high as 90° or beyond, a single maneuver could cover attached flows, vortex and burst vortex flows as well as totally stalled flows. In addition, the more highly separated flows are increasingly sensitive to unsteady and time history effects, hence maneuver dynamics become very important under such conditions. The understanding of these flow fields and dynamic effects is needed in order to design aircraft to exploit the above concepts, however this represents several quantum jumps over current aerodynamic technology.

A fact that has long been common knowledge among both fighter and stunt pilots, is that dynamic maximum lift coefficients can be achieved with high positive pitch rates that exceed the static values by significant margins. Under such conditions, higher pitch rates lead to higher dynamic overshoot. Numerous studies have also been conducted with regard to the dynamic lift characteristics of airfoil sections for application to the design of helicopter rotors. One of the more significant publications presents a wide variety of dynamic two dimensional results for eight advanced airfoil sections (Ref. 3). Lift, drag and pitching moments as well as pressure data are plotted for different amplitudes of oscillation and mean angles of attack up to a maximum total incidence of 25° . In these data, it is apparent that dynamic drag polars show significant improvement for positive pitch rate and degradation for negative pitch rate. There are also many cases in which the dynamic maximum lift coefficient approaches almost twice the static value.

Much less is known, however, about three-dimensional unsteady flows at high incidence. These flows involve streamwise oriented vortex systems as opposed to the cross flow oriented vortices of two-dimensional flows. This is an important distinction that characterizes the flow fields produced by current and near future fighter designs that make use of strakes, vortex flaps and/or highly swept leading edges. With such flows, the influence of pitch rate on vortex break-down and total flow separation is of prime importance. Also, these configurations achieve static C_{Lmax} in the 40° incidence range which means that dynamic C_{Lmax} may be achieved at incidences approaching 90° . Evidence from YF-16 flight test (Ref. 4) shows that hysteresis loops in lift vs angle-of-attack exist that are similar to those

observed in the two-dimensional flow studies. These results also indicate that the static values of C_{Nmax} at $\alpha = 40^\circ$ can be increased dynamically by 50% at $\alpha = 65^\circ$ with pitch rates on the order of 50° per second.

The development of unsteady aerodynamic flow fields and forces for rapidly maneuvering aircraft can be studied with dynamic wind tunnel testing techniques. Model motions which are either transient or oscillatory can be used to simulate aircraft maneuvers and provide the needed information for aircraft design purposes as well as analysis development and validation. A simple transient (1-cos) wave provides an incidence time history that simulates a rapid pull-up/push-over (or pitch/pulse) maneuver starting at a steady minimum angle, pulling up to a peak angle then returning to the original minimum and holding. Incidence change during the pitch/pulse can be quite large ranging from 5° up to 90° . Oscillatory motion between the minimum and peak angles is representative of the (1-cos) wave where the frequency is the inverse of the maneuver time. That is, if a full-scale pitch/pulse requires 4 seconds to complete, then the corresponding oscillatory frequency is 0.25 Hz. A tenth scale model motion is dynamically similar for the same free stream velocity with a pitch/pulse time of 0.4 sec or a frequency of 2.5 Hz. The scaling is also affected by velocity so that if the model is tested at 1/2 of the full-scale velocity, the pitch/pulse time is increased to 0.8 sec or 1.25 Hz.

In order to better understand the development of aerodynamic loads for fighter aircraft maneuvering beyond stall, a low speed ($M = 0.2$) wind tunnel test was performed during August-September 1986 in a cooperative program between General Dynamics and the National Aerospace Laboratory (NLR) of The Netherlands (Ref. 5). This effort was funded by the Flight Dynamics Laboratory of the Air Force Wright Aeronautical Laboratories. The model was designed and built at NLR with funds provided by General Dynamics and NLR. The test conditions, described in more detail in Ref. 5, were based on a matrix of conditions for mean angles ranging from -8° to 50° , amplitudes of pitch oscillation from $\pm 2^\circ$ to $\pm 18^\circ$ and frequencies from 0 Hz to 16 Hz. The model had a straked wing planform and was instrumented with an array of in situ pressure transducers and accelerometers in addition to a six-component force balance. Force and pressure results were recorded in the form of time history and harmonic component data. Vortex flow-visualization data from smoke flow illuminated by a chopped laser light sheet were also recorded with a still photo camera and a video camera. With over 1200 test points and 3600 flow-visualization photos, the data base generated by this test is quite extensive.

As an extension to the General Dynamics/NLR investigation, force testing of small-scale models in a small wind tunnel and a water tunnel was investigated as an inexpensive and quick means

to obtain meaningful dynamic force and moment data representative of rapidly maneuvering full-scale aircraft. Force tests of flat-plate semi-span models were conducted in the General Dynamics Aerodynamic Development Facility (ADF) which is a small 14x14 in² low speed wind tunnel. Oscillatory model motions up to 48° (peak to peak) amplitude were tested at frequencies of 1 to 3 Hz. Force tests of flat and three-dimensional full span models were conducted in the General Dynamics Hydroflow Facility (HFF) which is a horizontal flow water tunnel with a 24x24 in² test section. Pitch/pulse model motions were tested for conditions similar to those tested in the ADF. The test velocities were 100 fps in the ADF and 0.8 fps in the HFF which yielded nominal test Reynolds numbers of 0.6×10^6 and 0.06×10^6 respectively (based on root chord). Frequencies of motion in the HFF were scaled with velocity to maintain constant non-dimensional frequencies and pitch rates. Thus, frequencies for the HFF tests were nominally 0.01 and 0.03 Hz.

Specific objectives of this investigation were: (1) verify static and dynamic force and moment measurements from the small scale tests with results from reliable or multiple sources; (2) determine time history effects for various frequencies, amplitudes, starting angles and peak angles; (3) evaluate the effects of test medium; (4) determine Reynolds number effects; (5) demonstrate the importance of model three-dimensionality; and (6) evaluate the effects of planform geometry variations. This Volume I presents a description of the test program, correlations with other data, and discussions of the specific objectives of this investigation. A supporting data base is provided in Volume II for the ADF results and Volume III for the HFF results.

2.0 SYMBOLS

A_{mt}	A_m/A_t
A_m	Model Planform Area, ft^2
A_t	Tunnel Test Section Area, ft^2
C_l	$M_l/(qA_ms)$, Rolling Moment Coefficient
C_m	$M_m/(qA_mC_r)$, Pitching Moment Coefficient
C_N	$F_N/(qA_m)$, Normal Force Coefficient
C_{Nmax}	Maximum Steady Value of C_N
c_r	Root chord, ft
f	Frequency, Hz
F_K	Kinematic Force, lbs
F_N	Normal Force, lbs
F_V	Viscous Force, lbs
k	$\pi f c_r/V$, Reduced Frequency
MAC	Mean Aerodynamic Chord, ft
M_l	Rolling Moment, ft-lbs
M_m	Pitching Moment, ft-lbs
q	$\rho V^2/2$, Dynamic Pressure
q_0	Value of q for Model at $\alpha = 0$
Re	$\rho V c_r/\mu$, Reynolds Number
s	Semi-span, ft
V	Free Stream Velocity, ft/sec
α	Angle of Attack, deg
$\dot{\alpha}$	Pitch Rate, deg/sec
$\bar{\alpha}$	$\Delta\alpha k \pi/180$, Non-Dimensional Pitch Rate
$\ddot{\alpha}$	Angular Acceleration, deg/sec ²

α_{\min}	Minimum Angle, deg
$\Delta\alpha$	Oscillatory or Pitch/Pulse Half Amplitude, deg
α_{ts}	Value of α Where Wing Totally Stalls (or separates), deg
δ	Boundary Layer Thickness, ft
ρ	Fluid Density, slugs/ft ³
μ	Fluid Viscosity, lbsec/ft ²

3.0 TEST PROGRAM

In this section, a description is provided of the equipment and procedures used to perform small scale dynamic testing in the General Dynamics small low speed wind tunnel and water tunnel. The two tunnels, balance and support systems, data acquisition procedures, test plans, models, test procedures and data reduction will all be described.

3.1 GENERAL DYNAMICS TEST TUNNELS

The small low-speed wind tunnel used in this investigation is referred to as the General Dynamics Aerodynamic Development Facility (ADF). This is a small open-circuit low speed wind tunnel which is schematically shown in Fig. 3-1. This tunnel was originally designed as a flow visualization tool and therefore has a very low turbulence level. It has since been modified to permit semi-span force testing with a 5-component strain gage balance that is connected through the tunnel floor. All components are measured except for side force. The test section is 14x14 in² with a splitter plate located 0.625 in. above the tunnel floor for minimizing boundary layer buildup in the vicinity of the model. The tunnel velocities range from 100 to 165 fps which give a maximum Reynolds number capability of 1×10^6 per foot. Air is drawn into the tunnel from the large room where it is located which provides close control of the test environment. Energy loss through the entrance screens was assumed to be negligible, thus total pressure in the test section was taken to be the atmospheric pressure. Pressure differential was measured with an inclined manometer which along with atmospheric pressure, temperature and humidity was used to calculate test section velocity.

The water tunnel used in this investigation is referred to as the General Dynamics Hydroflow Facility (HFF). The HFF is a horizontal flow water tunnel with continuous return that was designed and built by Fluidyne (See Figure 3-2). The test section is 2 ft x 2 ft with a variable velocity capability ranging from 0.1 to 1.0 fps and can be operated with either a closed or open upper surface. All force testing, however, utilized the open surface capability for both ease of operation and hopefully a reduction of wall interference effects. This latter consideration is based on the conformal effect produced by the free upper surface. Flow visualization capability is provided with up to six colored dyes and more recently, hydrogen bubble generation. Flow-viz recording is accomplished with several video cameras and still photo cameras from three sides of the model as well as from downstream.

The HFF is equipped with a turbine type flowmeter for monitoring velocity. This meter was calibrated in the vicinity

of an indicated velocity of 1.0 fps ranging from 0.6 to 1.4. At 1.0 fps indicated, the actual velocity was found to be 0.81 fps. The calibration was accomplished in two ways by measuring drag force on a 2 in. flat disk and timing the passage of drops of dye over a distance of 5 ft.

3.2 BALANCE AND SUPPORT SYSTEMS

The balance and support system used for semi-span testing in the ADF wind tunnel is shown in Fig. 3-3. This system was developed as an adaptation to dynamic testing of the existing static test support setup for the ADF. The balance adapter, bearings, support plate, motor plate and stepper motor were added to accomplish this conversion. The existing balance was unmodified and had an accuracy of at least $\pm 1\%$ for all components.

Instantaneous angle of attack was measured with a rotary pot that was attached to the balance adapter shaft and mounted on the bearing plate. The only error that was involved was angular deflection due to balance torsional twist. This was small however since the balance was designed for tests at two to three times the dynamic pressure levels that were used in the current investigation.

The balance and support system use for full-span testing in the HFF water tunnel was developed at General Dynamics (Ref. 6 and is shown schematically in Fig. 3-4. The balance was designed to measure all forces and moments with exception of side force and to permit rotation from 0° to 90° incidence. Incidence control was provided by a programable stepper motor mounted outside of the water tunnel through a crank and driving strut as shown in Fig. 3-4. The driving strut rotated the pitch yoke which was pivoted on the stationary support struts also shown in the figure. The balance then transmitted the angular position from the pitch yoke to the balance housing attached to the model. Bending and torsional deformations were measured with miniature strain gages which, along with their lead wires, were water proofed.

The balance was calibrated only for normal force and pitching and rolling moments as described in Ref. 6. A known force range was applied at five different locations on a calibration plate that was bolted to the balance. A matrix of coefficients was obtained which was verified with a full set of load checks to be within $\pm 1\%$ accuracy. Model incidence change due to pitching moment and normal force was also checked and found to be $+0.7^\circ$ per in-lb and no detectable change due to pure normal force. The range of pitching moments encountered in the current investigation was on the order of 0.25 in-lb or less.

The support and drive struts were formed of stainless steel tubing with provisions made for adjustment to permit model alignment. The driving strut was also adjustable and set to provide minimum error between the stepper motor and model angular positions. The maximum error observed was 2° where the model indicated a change of 88° compared to a stepper motor change of 90° . Since the error was shown to have a linear variation from 0° to 90° , corrections were possible with a simple calibration run. An M.C. clinometer (Hilger and Watts) was used to measure model angles. This clinometer had an accuracy of 1 min. of arc and the procedure used to determine model angle had a repeatability of within about $\pm .125$ degrees.

Indications of model incidence were obtained in different ways depending on whether static or dynamic force runs were being made. For static runs, stepper motor commands were used to generate data for model incidence. For dynamic runs, a Spectron angle sensor, mounted on the stepper motor driving arm, was used to generate dynamic model incidence. This sensor had an accuracy of ± 3 mins. of arc and had sufficient response to track the types of angular velocities required for dynamic testing in the water tunnel. In both cases, the above mentioned angle calibration was used to correct stepper motor position for true model position.

3.3 DATA ACQUISITION PROCEDURES

The higher frequency requirements for dynamic testing in the ADF necessitated the use of analog recording with a frequency response of at least 1000 Hz. A seven channel analog recorder was used to record five strain gage bridge outputs from the balance along with angle-of-attack. IRIG time was also included on the analog tapes. The analog tapes were digitized at 1000 samples per second and the digital data written on a MASSCOMP magnetic tape in a format that could be read on the VAX.

Programs were developed on the TEKTRONIX 4052 to accomplish various tasks. One program drove the stepper motor at desired frequencies, amplitudes and incidence ranges in either single pulse (1-coswt) motions or continuous oscillatory motions. Other programs were written to relate test conditions such as tunnel velocity, atmospheric pressure, model pitch amplitude and frequency of oscillation to key parameters such as Reynolds number and non-dimensional pitch rate and frequency. Close control of these and other parameters was exercised in order to simplify data analysis and maximize usefulness of the results.

Digital data for the HFF water tunnel tests were directly acquired with a Hewlett Packard 3497A Data Acquisition Unit (DAU) from the balance strain gage bridges and the angle sensor in the case of dynamic testing. Communications were established between

the DAU and an IBM personal computer clone, the SUN-ST PC. Because of time required for data communication between the DAU and PC, the maximum data sample rate was one complete reading of all channels every 0.4 seconds for static testing (4 channels) and every 0.7 seconds for dynamic testing (5 channels). Three channels were required for the balance output, one for strain gage excitation voltage and one for the angle sensor.

The SUN-ST PC was programmed to process data output from the DAU and store on a 5 1/4 in. floppy disk for transmittal to the General Dynamics VAX cluster through a Zenith P.C. The software was coded in IBM Basic to form separate programs which were used to: (1) record zero condition voltages and store for force data processing; (2) drive model incidence and record water-off ($v=0$) tare balance outputs for an incidence sweep as well as record and store incidence calibration data; (3) drive model incidence and record water-on balance outputs for static or dynamic tests with incidence information; and finally (4) process and store on the floppy disk, final corrected force, moments and incidence data. The forces and moments were calculated from the balance output voltages with the balance matrix of coefficients discussed in the previous subsection. The excitation voltage was continuously monitored by the DAU and if it deviated more than ± 1 mv, the recorded data were rejected and set at either 0 volts or 10^{13} volts.

3.4 TEST PLANS

The primary objective of this investigation was to evaluate the testing of small scale models in small low-speed wind tunnels or water tunnels as a means of obtaining meaningful dynamic force and moment data that are representative of rapidly maneuvering full-scale aircraft. In order to fulfill this objective, a plan was developed for conducting both static and dynamically similar tests in the ADF wind tunnel and HFF water tunnel located at General Dynamics Fort Worth Division. Four different flat plate models (see Subsection 3.5) were used with a common test plan for both tunnels. Test conditions were established to cover all types of flow fields including attached, vortex, burst vortex and completely stalled or separated flows.

The test plan to obtain static baseline data was slightly different for the ADF and HFF tests. In the ADF, a coarse grid of incidences was used starting at 0° and increasing at 10° increments to the maximum allowable incidence. Data were obtained only for increasing angle, and wind speed was maintained at a nominal 100 fps for all tests. The HFF test plan also used a simple α -sweep going from -0° to 90° to 0° model incidence with data measured more frequently at 2.5° increments. The α -sweep included both increasing and decreasing incidence so as to determine static hysteresis effects. Water velocity was held

constant at a nominal 1.0 fps indicated with the model at zero incidence which provided an actual velocity of 0.81 fps. The models were not tested in yaw since this test was aimed at longitudinal force testing only.

The basic dynamic test plan used is shown in Table 3-1 as a matrix of dynamic conditions. This matrix was based on 8° increments to the minimum angle during oscillation (or pitch/pulse) and $\pm 8^\circ$ amplitude increments (16° peak-to-peak) to the dynamic motion. Two non-dimensional frequency values were used as listed in Table 3-1, however, the corresponding values for the straked wing model were slightly lower as also noted. The cut-off in peak angle for the straked wing was imposed by the fact that the model nose hit the wind tunnel wall at about 68° .

As an important aspect of testing in both tunnels, static and dynamic tare forces were required for zero air or water velocity. The full matrix in Table 3-1 was not needed for the dynamic tare runs, however, a full set of amplitude/frequency runs were made up to the maximum amplitude. Static tare runs were made in both tunnels, and, because of the low frequencies in the water tunnel, dynamic tares were obtained only in the wind tunnel.

3.5 MODELS

Four basic flat plate models were tested in both the ADF and HFF tunnels. These were the straked wing model, 55° delta, 70° delta and a $70^\circ/30^\circ$ cranked wing. The pitch axes were all located at 58.33% of the root chord except for the straked wing which was at 74.6%. The models were different sizes since semi-span models were used in the ADF and full span models were used in the HFF. Therefore, descriptions of each set of models will be presented separately.

The four semi-span ADF models are shown in Fig. 3-5. The pitch axes are also shown for each model. All models were fabricated from 0.060 in. thick aluminum sheet and attached to the balance at the pitch axis. Leading edges were rounded to that they were all cylindrical normal to the leading edge. Side and trailing edges were left square. The only exception was that the straked wing model had a symmetric sharp edge along the strake leading edge as shown in Fig. 3-5.

The corresponding four models tested in the HFF are shown in Fig. 3-6. The pitch axes are also shown for each model. All models were fabricated from aluminum sheet, where the straked wing and 70° delta were 0.060 in. thick and the 55° delta and cranked wing were 0.050 in. thick. All model edges were treated in the same way as those for the ADF models.

Two additional models were tested in the HFF water tunnel as shown in Fig. 3-7. The three-dimensional E-7 model was a 1/40-scale model of a STOVL configuration being developed at General Dynamics. The flat plate model was a plan view "cut-out" of the E-7 3-D model fabricated from 0.050 in. thick sheet aluminum with rounded leading edges on the nose and wing. The side and trailing edges were left square. The 3-D E-7 un-cambered wing model was produced in the display model shop at General Dynamics with an accuracy of ± 0.0001 in. The 3-D E-7 model was ballasted to be neutrally buoyant and modified on the lower surface as shown by the dashed line in Fig. 3-7 to accommodate the water tunnel balance.

The philosophy behind the choice of models was mostly based on availability of test data from either reliable or multiple sources for purposes of validating the small scale force testing techniques. The straked wing was chosen because of the recently available steady and unsteady data base from a test conducted at NLR (Ref. 5). The two delta wings were chosen so as to investigate the effects of wing sweep and compare results with the data of Wentz (Ref. 7) as well as Chang and Muirhead (Ref. 8). The cranked wing was chosen so as to investigate the effect of adding a 30° swept tip panel to the 70° delta, although no correlating data were available from other sources. A very important set of steady HFF data were generated with two flat disks in Ref. 6. These data are discussed in this report as part of the validation procedure through comparison with data available from Hoerner (Ref. 9). Finally, the E-7 model was tested as both a scaled 3-D model and a flat plate "cut-out" model to investigate the effects of three-dimensionality on dynamic forces. The steady 3-D model data were correlated with 1/9-scale force data available from a low speed test in the NASA Ames 12 foot wind tunnel (Ref. 10).

3.6 TEST PROCEDURES

Because of the large difference in test velocities, the procedures followed in the ADF and HFF tests were likewise quite different. In the ADF, dynamic testing was the more difficult problem due to high model accelerations. In the HFF, both static and dynamic testing presented difficulties.

Static testing in the ADF was accomplished at a constant velocity of about 100 fps and was straight forward with one exception. The use of semi-span models always encounters problems associated with side wall boundary layer contamination of the flow-fields over the wing. A practice that has been followed at General Dynamics for some years, seems to eliminate most of these problems where a small gap is maintained between the model root and the sidewall. This gap size is about 0.06 in. which is about one half of the boundary layer displacement

thickness on the splitter plate at the model position. The same gap size was determined independently by two researchers at General Dynamics on the basis of flow visualization results in one case and force data in the other case.

Dynamic testing in the ADF was complicated by the presence of significant inertia forces and moments in the recorded balance data as a results of the high frequencies of model oscillation. The test procedure included recording air-off data for dynamic tare values of force and air-on data for two different time histories. Test velocity was held constant at about 100 fps. The first time history was a simple pitch/pulse as represented by a single cycle $(1-\cos\omega t)$ wave starting at α_{\min} (illustrated in Table 3-1). The second time history included 20 cycles of continuous oscillatory motion. Point numbers were recorded on an audio track on the analog tape along with an IRIG time. During the first test with the straked wing, dynamic tares were recorded for each comparable air-on condition, including both the two types of motion and different α_{\min} values. However, for later tests dynamic tares were recorded only for motion amplitude and frequency and continuous oscillation. During dynamic testing in the ADF, it was noticed that significant structural motion was excited for the two higher frequencies. These motions were identified as approximately the first torsion and first bending modes of the model on the balance. Also, stepper motor torque was insufficient to drive some models at the higher amplitudes and higher frequencies. Therefore the better data were obtained at the lower three frequencies (which physically correspond to about 1, 2 and 3 Hz).

Test procedures for static force testing in the water tunnel were established in Ref. 6 to minimize the effects of model motion time history but still maintain reasonably rapid data acquisition. It was expected in the beginning that the low test velocities on the order of 1.0 fps would necessitate excessive dwell times at data points to obtain accurate static forces. These times would scale with the inverse of the velocity so that if 5 sec. were adequate for a dwell time at 100 fps in air, 500 sec. would be needed at 1 fps in water. Hopefully, such excessive times would not be necessary.

Initial static tests described in Ref. 6 were conducted with a pitch/pause schedule of 5 sec. delay and 5 sec. record times at every 5° of incidence. A full sweep was made from 0° to 90° back to 0° so as to monitor static hysteresis effects. Changes of incidence with an increment of 5° were made with the stepper motor programmed to rotate at the rate of 0.1 rad per sec. Results from these initial tests showed significant static hysteresis as well as other undesirable features.

A study was conducted as described in Ref. 6 to determine the effect of stepper motor pitch rate, incidence step size,

delay time and record time. A pitch rate of 0.01 rad per sec. was found to eliminate excessive model vibration and yet not slow the data acquisition significantly. Incidence step sizes were found to have no significant influence with the lower stepper motor pitch rate. Delay/record times were found to have a significant effect, however, especially on "static" hysteresis. A systematic variation of delay/record times was investigated with the flat disk for the values 10 sec/10 sec, 20 sec/20 sec, 40 sec/20 sec and 40 sec/40 sec respectively, where the hysteresis was reduced with increase in both delay and record times. Finally, it was found that the differences between 40 sec/20 sec and 40 sec/40 sec were insignificant, hence the former was chosen as the standard.

The model incidence profile for static water tunnel testing that was programmed into the driving software used the 40 sec/20 sec delay/record times, 2.5° increments and 0.01 rad per sec stepper motor pitch rate. Incidence sweeps could be varied, however, the standard sweeps for all tests used 0° to 90° and 90° to 0° .

Dynamic test procedures in the water tunnel were fairly simple since the problems faced in static testing were of no concern for a moving model. One problem that was encountered during dynamic tests was the occurrence of large amplitude oscillations in force and moment data that seemed to scale with frequency as described in Ref. 6. This was attributed to vortex shedding at the very low fluid velocities and placed an upper limit on test frequencies of about 0.03 Hz. Further discussion of this phenomenon will be given in Section 6.0. Because of the very low frequencies, it was not necessary to record dynamic model tare forces at zero velocity because the inertial forces due to model accelerations were essentially zero.

The low test frequencies used in the water tunnel that eliminated dynamic inertial forces, however, introduced another problem related to model incidence time history as discussed in Ref. 6. A lower limit on stepper motor pitch rate, as well as integer multiples of that value, was found to significantly affect the pitch/pulse profiles, particularly in the case of low amplitude and low frequency. Time histories of pitch/pulse incidence for the low and high frequency cases (periods of 107.0 sec and 38.6 sec respectively) are shown in Fig. 3-8 for amplitudes of 16° , 32° and 48° with a starting angle of 8° . The profile is a (1-cos) wave-form also shown in the figure, which is well represented with the high frequency 48° amplitude case. As amplitude is diminished at high frequency, the actual wave-form continuously departs from the ideal shape. At 16° amplitude, the pitch rate at high frequency is close to the 48° amplitude at low frequency, hence these two wave-forms are very similar. As amplitude decreases at low frequency, the wave-form deteriorates to a triangular shape at 16° . This last case represents the

minimum pitch rate available for the stepper motor used in this investigation. Fortunately, the more important high frequency, high amplitude wave-forms are accurately represented.

The final test procedure used in the HFF for either static or dynamic testing consisted of six steps: (1) record balance output voltages with water off and model at zero incidence; (2) record balance output voltages with water off and the standard incidence sweep (10 sec. delay, 10 sec. record); (3) record model incidence calibration data (nominally four angles over the incidence sweep) and generate correction terms; (4) record balance output voltages with water on (velocity set for model at zero incidence and left unchanged for both static and dynamic conditions); (5) convert balance voltages to forces and moments and write on a floppy disk; and (6) transfer data from floppy disk to the General Dynamics VAX cluster for final processing into force and moment coefficients, plotting in the desired format and further analysis.

3.7 DATA REDUCTION

The digitized force and moment data obtained from both the ADF and HFF tests were processed on the General Dynamics Fort Worth Division VAX cluster using essentially the same software. The raw forces and moments were converted into normal force, pitching moment and rolling moment coefficients as defined in the Symbols section. Several steps were taken, however, to arrive at the final form. First, the data had to be filtered to remove undesirable high frequency oscillations due to model dynamics in the case of ADF testing and the viscous oscillatory fluid forces for HFF testing. Next, the inertia forces had to be determined from zero velocity data and subtracted from the data obtained at the standard test velocity. Finally, the wall interference and blockage effects had to be removed. Each of these steps will be briefly discussed in the following paragraphs.

The low pass digital filter used for either ADF or HFF data processing was the same in which only the frequency had to be changed. The form of this filter was

$$y_i = (1-a) x_i - a y_{i-2}$$

where at the i th digitized point in time

y_i = output

x_i = input

$a = e^{-\Delta t(2\pi f)}$, f = cut-off frequency, Hz

Δt = incremental time per digital step

In order to increase the sharpness of this filter, four passes were used for the HFF data and six passes for the ADF data. By

making half of the passes forward in time and the other half reverse in time, it was also possible to eliminate time lag introduced by the filter. The cut-off frequency used for ADF data was 25 Hz and for the HFF data, 0.25 Hz.

Static inertia forces were not present for the ADF model since its plane was oriented in the vertical direction. Dynamic inertial forces were present, however, and had to be removed from the air-on data. The effective dynamic mass for each component of force was determined directly from air-off data through the relation

$$M \approx -\frac{1}{\ddot{\alpha}} \text{ (air-off balance output)}$$

where M is the effective mass and $\ddot{\alpha}$ is the model angular acceleration which is known from the model position time history. This was accomplished for normal force, pitching moment and rolling moment, then the raw force/moment data were corrected according to

$$\begin{aligned} (F_N)_{\text{corr}} &= (F_N)_{\text{unc}} - M_{FN} \ddot{\alpha} && \text{(normal force)} \\ (M_P)_{\text{corr}} &= (M_P)_{\text{unc}} - M_{MP} \ddot{\alpha} && \text{(pitching moment)} \\ (M_L)_{\text{corr}} &= (M_L)_{\text{unc}} - M_{ML} \ddot{\alpha} && \text{(rolling moment)} \end{aligned}$$

The corrected data then represented aerodynamically induced forces and moments.

Static inertial forces were present in the HFF force and moment data since the model pitch axis was horizontal. Because of the low test frequencies in water, the dynamic forces were zero, hence static inertia corrections were all that were needed in the dynamic water tunnel data. These were simply measured with zero water velocity, fit with smoothing curves and subtracted from water on data in either case of static or dynamic tests.

Correction techniques for wall interference and model blockage effects were applied over the entire incidence range up to 90° to both ADF and HFF force/moment data. A simple correction which has been recently experimented with at General Dynamics was implement to account for these effects in the ADF data. This technique simply involves non-dimensionalizing force and moment data at all incidences by a constant value of the dynamic pressure, q_0 , measured with model incidence set at zero. This approach ignores the variation of q with incidence since that variation tends to be inversely proportional to wall interference and blockage. The cancellation effect works best in the ADF for model planform areas on the order of 10% to 20% of the test section area. Hence, q_0 was measured at $\alpha = 0$ for a particular model and test condition and the remaining test was

conducted without changing tunnel velocity or motor speed. The q_0 value was then used for all data reduction of that particular run.

The "constant q_0 " technique was also used in the HFF data reduction. Again, q_0 was measured at $\alpha = 0$, then the water tunnel driving motor speed was left untouched and the velocity allowed to vary as the blockage dictated. The water tunnel was also used with the upper surface open so as to simplify model changes and hopefully obtain a lower wall interference through a conformal free surface. This apparently was the case in the HFF since it was found that the "constant q_0 " technique seemed to work well for smaller models with 5% blockage as opposed to 10% minimum blockage in the ADF.

Additional corrections were found necessary in the HFF at incidences beyond static C_{Nmax} . These were required as a result of a significant expansion of the wing wake when the wing stalls. The correction was developed in Ref. 6 as a semi-empirical relationship based only on planform blockage and angle of attack. The equation used was of the form

$$(C_N)_{corr} = (C_N)_{unc} (1 - C_W A_{mt} \sin \alpha')^2, \alpha \geq \alpha_{ts}$$

where

C_W = 1.57 (empirically determine coefficient)
 A_{mt} = ratio of model planform area to test section area
 α_{ts} = incidence at which the wing totally stalls

$$\alpha' = 90^\circ \left(\frac{\alpha - \alpha_{ts}}{90^\circ - \alpha_{ts}} \right)$$

This equation is for C_N , however, it was also applied to C_m in the same manner. A discussion of the development of this correction is given in the Appendix as an excerpt from Ref. 6.

It was not possible to apply a similar correction technique to the ADF results. A consistent trend could not be found on which the relationship could be based in contrast to what was observed in the water tunnel. However, as will be seen in normal force comparisons to be discussed later in this report, the effect of such a correction on ADF results would not be significant.

After all corrections were applied to the force and moment coefficients, the data were averaged for multiple time histories. For the ADF oscillatory data at least five consecutive cycles were used to obtain averaged final results, however, in some cases as many as twenty cycles were used. The three-pitch/pulses made in the water tunnel for each test point were likewise averaged together in a similar manner.

4.0 TEST RESULTS

The results of the test program described in the previous section are presented in both plotted and tabulated form in Volume II of this report for tests in the ADF wind tunnel and in Volume III for tests in the HFF water tunnel. Because of the large number of parameters, the resulting data base became quite extensive and hence a format was developed which would compress the data as much as possible and yet follow a rational logic for presentation. The purpose of this section is to describe the format followed in Volumes II and III of this report and the logic behind its development for both the wind tunnel and water tunnel data sets.

4.1 DATA BASE FORMAT

Both static and dynamic data as well as model geometry are presented in the two data base volumes. The static data are in the standard format of force and moment coefficients vs angle of attack. The aerodynamic coefficients, C_N , C_m and C_l , are normal force, pitching moment and rolling moment and are defined in the Symbols section. The static data format requires no special attention, however, because of the interplay of incidence, amplitude and frequency in the dynamic data sets, the format developed for their display does require some discussion.

A time history plot of α and C_N vs time is shown in Fig. 4-1 for a pitch-pulse motion of the straked wing model in the ADF wind tunnel. The dynamic C_N data are shown by the solid line and the "static" data at equivalent α 's are shown by the dashed line. The purpose of this format is to emphasize the influence of model motion on the aerodynamic forces. Although it provides a graphic demonstration of the dynamic effects, it is not convenient for showing comparisons with other conditions. A more appropriate form is shown in Fig. 4-2 where the dynamic data are plotted in the standard C_N vs α format with arrows used to depict increasing time for the dynamic data.

In addition to the use of arrows to show increasing time, another format is employed where two different types of lines are used to denote increasing or decreasing angle. An example of this format is shown in Fig. 4-3 where the effect is demonstrated for holding the starting angle and frequency constant while increasing the peak angle on the straked wing. A second example is shown in Fig. 4-4 where the starting angle is varied and the peak angle and frequency are held constant. (These results were obtained in the ADF wind tunnel for single pitch-pulse motions at the low and high frequencies of 0.95 and 2.5 Hz.) This format is used exclusively in the data volumes since several conditions are shown in the same plot as was done in Figs. 4-3 and 4-4.

However, the tabulated data that are also included in the data volumes, provide a means for distinguishing between various trends when needed. For discussions of the effects of frequency, planform, etc., the use of arrows will usually be employed in this Volume I.

4.2 VOLUME II - ADF WIND TUNNEL DATA BASE

Results for oscillatory tests of the four basic models, the straked wing, 55° delta, 70° delta and cranked wing, are given in plotted and tabulated form in Volume II. Those data were obtained as the averages of at least five cycles of oscillation and are shown as single data sets. In addition, selected plots are shown for un-averaged data over many consecutive cycles in order to demonstrate repeatability.

The static data are presented in the format shown in the example in Fig. 4-5. Since the ADF models were semi-span, valuable information was also available with regard to wing root bending moment in the form of the rolling moment coefficient, C_l . Thus, the ADF data plots include C_l results as well as C_N and C_m . Also shown in the static format is a brief description of the flat plate model. Planform shape, area and dimensions, plate thickness, leading and trailing edge shape and pitch axis location as a fraction of root chord are included.

The dynamic C_N , C_l and C_m data are presented in the format shown in the example in Fig. 4-6. This example illustrates the effect of fixed starting angle and varying peak angle for the low and high frequency values. Static data for reference are shown as the short dashed lines and the dynamic data are shown as solid lines for increasing angle and long dashed lines for decreasing angle. Arrows are added to this example for clarification. With exception of the pitching moment the different curves are easily distinguishable; however, in other cases such as for the lower frequencies, this is not the case and need for tabulated data becomes obvious. The tabulated data for averaged results follow the plotted results for each model in Volume II.

4.3 VOLUME III - HFF WATER TUNNEL DATA BASE

Results for the pitch-pulse tests of the four basic models, the straked wing, 55° delta, 70° delta and cranked wing, are given in plotted and tabulated form in Volume III. In addition, data are also given for the E-7 three-dimensional and flat plate models. All data are for the averages of three separate pitch-pulses and are shown as single data sets. Selected plots are also shown for un-averaged data from the three pitch-pulses to demonstrate repeatability for all models including the two E-7 models.

The static data are presented in a format similar to that for the ADF wind tunnel data as shown in the example in Fig. 4-7. In this case, C_l is not included since the models are full span as emphasized by the model sketch. Also shown in Fig. 4-7 are the static results for both increasing and decreasing model incidence to demonstrate static hysteresis effects. Although this is not too pronounced in the example, it is significant for some of the other models, especially the E-7 three-dimensional model.

The dynamic C_N and C_m data are presented in the format, which is also similar to that for the ADF wind tunnel data, as shown in the example in Fig. 4-8. The only difference between this and the format shown in Fig. 4-6, is the absence of C_l data in Fig. 4-8. Comparing Figs. 4-6 and 4-8, it is seen that the C_N results agree fairly well, however, the C_m results are quite different but do show similar trends. The ADF and HFF C_m data have similar loop structure for the higher amplitude cases although they are more open for the latter case. The comparison of ADF and HFF data will be discussed in more detail in the Discussion section.

5.0 CORRELATIONS WITH LARGE SCALE DATA

In order to verify that forces and moments measured on the small scale models are representative of those configurations, comparisons were made with results that were obtained from larger scale models or tests in which high confidence could be placed. For static data, reliable or multiple sources were available for the flat disk, straked wing, 55° delta, 70° delta and the three-dimensional E-7 models. For dynamic data, reliable sources were limited to the straked wing model, however test conditions were sufficiently varied for this model so that the effects of frequency, amplitude and mean angle could be considered in the correlations. The small scale results used in the following correlations have been adjusted for the corrections as outlined in the subsection on Data Reduction. All correlations pertaining to static tests in the water tunnel were taken from Ref. 6.

5.1 STATIC CORRELATIONS

One of the best sources of data for correlating with the small scale static results is the straked wing test as reported in Ref. 5. The model which was of fairly large scale as shown in Fig. 5-1, was tested in the $2.25 \times 3.00 \text{ m}^2$ Low Speed Tunnel at the National Aerospace Laboratory (NLR) in The Netherlands. This model was statically tested at speeds of 25 m/sec and 66 m/sec suspended by wires to provide minimum support interference. It was both static and dynamically tested at 80 m/sec mounted on the dynamic support and driving mechanism as shown in Fig. 5-2. Therefore the effects of Reynolds Number and support interference could be separated for this model.

A comparison of ADF wind tunnel data for the straked wing static test is made in Fig. 5-3 with static NLR data from Ref. 5 for the test in wires at 25 m/sec. This comparison seems appropriate since the semi-span model mounting in the ADF has a minimum of support interference (see descriptions of the ADF wind tunnel, models and support). Also, the velocity is about the same although due to model size differences, the Reynolds Number is only about 0.55×10^6 for the ADF test but about 1.4×10^6 for the NLR test. As can be seen in Fig. 5-3, C_N data track well up to vortex burst at about 18° , however, the ADF data show a similar but lower level characteristic up to the point of crossing at about 40° . This difference is similar to that seen between the NLR test in wires data at speeds of 25 m/sec and 66 m/sec and is therefore attributed primarily to Reynolds Number effects. The C_m data do not match well, either in magnitude or trend except that both show a general pitch-up trend with increasing angle. Similar disagreements between ADF semi-span

model results and HFF full span model results were observed on the other models which suggests that this difference is due primarily to (1) semi-span type flow fields and (2) wall interference which is greater for the larger models in the ADF test. Some influence due to Reynolds Number effects probably exists in the range between vortex burst and maximum C_N as will be evident in the following discussion of HFF/NLR correlations.

Since the HFF water tunnel models were mounted on a support structure similar to that used in the NLR test, HFF results were compared with NLR data taken for the model mounted on the dynamic support (Ref. 6). This comparison is shown in Fig. 5-4 where water tunnel data were obtained for both increasing and decreasing angle at $Re = 0.06 \times 10^6$ and the NLR data were taken at 80 m/sec for $Re = 4.5 \times 10^6$. Agreement between the C_N results is remarkable considering the difference in Reynolds Number. The low level for HFF data up to vortex burst is attributed to higher interference of the balance on the lower surface as discussed earlier under Data Reduction. Beyond that point, the differences are attributed to Reynolds Number effects in the same manner as discussed above for the ADF data. The C_m results also show remarkable agreement up to vortex burst after which the lower level for the HFF data is attributed to Reynolds Number effects. The C_m data merge back together at about 40° and tend to track each other as far as possible.

Comparing the correlations shown in Figures 5-3 and 5-4 provides evidence for separating out the effects of semi-span testing. The ADF models were placed so that about 1/16 inch space existed between the wing root and the wind tunnel splitter plate. This distance was about one half of the theoretical wall boundary layer displacement thickness in the vicinity of the model. In an earlier investigation, this practice was arrived at based on monitoring vortex bursting for a 70° delta wing while varying the spacing. If the space was either greater than 1/16 inch or zero, vortex burst tended to occur at a lower angle than that reported in many sources. With zero spacing, it was postulated that the wall boundary layer tended to weaken the leading edge vortex near the nose which led to early breakdown. For a larger space, such as 1/8 inch, a strong counter rotating vortex was formed along the root which likewise tended to weaken the leading edge vortex and led to early burst. The fact that the C_N results agree very well between the small scale tests and the appropriate NLR tests with differences that can be attributed to Reynolds Number verifies that the proper overall flow fields exist over both the HFF and ADF models. The differences in C_m , however, tend to point directly to semi-span testing as a significant source of such error. The space between the model and splitter plate in the ADF would tend to have more influence near the wing vertex and hence lead to reduced nose-up pitching moments. Thus, it can be concluded that semi-span testing as

described in this report will produce representative normal forces but centers of pressure that are too far aft.

A three way comparison of ADF wind tunnel data, HFF water tunnel data and results obtained by Wentz (Ref. 7) is shown for a 55° delta wing in Figure 5-5 for C_N and C_m vs α . The C_N data from the ADF test agree very well with Wentz's results as might be expected based on the Reynolds Number similarity. The HFF C_N data also agree very well up to C_{Nmax} but show an earlier break and a lower level after that point which are both felt to be attributable to Reynolds Number effects (Ref. 6). The C_m comparisons were made on the basis of modified values of Wentz's data where a C_{m0} value of -0.04 was subtracted out before transferring moments to the pitch axis in the current study (see Figure 5.3.1 in Ref. 7). As in the case for the straked wing, excellent agreement is shown between the HFF C_m data and the modified Wentz data (Ref. 6). Likewise, the ADF C_m data show a less nose-up characteristic, however, the angle at which the nose down break occurs, 26° , is very similar. Thus, the ADF semi-span test produced representative normal forces but centers of pressure which were too far aft; and the HFF full span test produced normal forces that were slightly low but centers of pressure that were about right.

A four way comparison of ADF wind tunnel data, HFF water tunnel data and two other experimental data sets is shown for a 70° delta wing in Fig. 5-6 for C_N vs α . Chang and Muirhead (Ref. 8) tested a 70° delta model at low speed with a trailing edge sting support and compared C_N data with Wentz's results (Ref. 7) for an identical model which was supported with struts attached to the lower surface. These two data sets, which are shown in Fig. 5-6, were used by Chang and Muirhead to illustrate the effect of support system interference since both models were the same and both were tested at similar Reynolds Numbers. Comparing these data sets with the ADF and HFF results likewise tends to confirm the dominant effect of support interference on the 70° delta. The HFF data with the under wing mounted balance and strut supports agrees quite well with the Wentz data in spite of a large difference in Reynolds Number (Ref. 6). On the other hand, the ADF data with minimum support structure interference agrees quite well with Chang and Muirhead. In this latter case the Reynolds numbers are almost identical, however, considering the difference in the former case, Reynolds number does not seem to play an important role for this model in contrast with the straked wing and 55° delta models. This is not surprising since the 70° delta will develop better organized vortex flows than the other two planforms.

The C_N comparisons in Fig. 5-6 offer another interesting possibility. Up to C_{Nmax} , the ADF and HFF data sets agree very well with each other and the same is observed for the Chang/Muirhead and Wentz data sets. In all cases the models were

thin and un-cambered, however the ADF and HFF models had rounded (cylindrical) leading edges where as the Chang/Muirhead and Wentz models had symmetric sharp leading edges of identical shape. Based on the root chord, the former models were slightly thinner at 0.66% for the HFF and 0.5% for the ADF models whereas the latter models were identical size and shape with a thickness of 0.73%. Therefore, thickness and size as well as support interference, test facility, Reynolds number, or medium do not seem to provide any suggested trend. This leaves the leading edge shape as the remaining parameter. Based on these results, it appears that the sharper edge develops a stronger vortex flow but not necessarily a higher value of C_{Nmax} . However, a slightly lower C_{Nmax} for the HFF results at low Reynolds number is consistent with the previous observations on the straked wing and 55° delta wing models. Thus, it can be concluded that leading edge shape has at least a second-order effect on the development of vortex lift on flat, thin, highly swept wings.

Also shown in Fig. 5-6 are the C_m results vs α from the ADF and HFF tests of the 70° delta. Similar data were not available from Ref. 8. Comparison of C_m data obtained by Wentz (Ref. 7) with large scale tests of related configurations showed that his results were not representative and were therefore not used in the comparisons. It is possible that the correction procedures he applied to account for support interference worked well for the 55° delta but failed for the higher swept 70° delta. Therefore only a comparison between the ADF and HFF data sets was possible for this model. As can be seen in Fig. 5-6, the C_m results reflect similar trends noted earlier. Where the semi-span model had a more aft center of pressure, however the differences are not as pronounced in this case for the 70° delta.

Turning to a more fundamental planform, the circular disk was used in development of the water tunnel balance (Ref. 6). This was one of the major configurations used for determining wall and support interference as well as blockage effects, particularly at high angles near 90°. An excellent source of data for C_N vs α was obtained from Hoerner's well known book (Ref. 9). HFF water tunnel results were obtained for two different sized models, a small disk of 7.02 in. diam. and a larger disk of 8.54 in. diam. The respective blockages in the 24 x 24 in² water tunnel were 0.0668 and 0.0994. The C_N and C_m data from the HFF test are shown in Figure 5-7 plotted vs α for both models along with C_N vs α data obtained from Hoerner. As can be seen, the large disk C_N data agree very well with Hoerner's data. The small disk results show a slightly lower level which is attributed to interference produced by the balance housing being mounted very close to the lower surface leading edge. It is postulated that this mounting, which is not the case for the large disk, has the effect of blunting the leading edge and thereby reducing vortex induced lift. This idea is further supported by the lower level of C_m produced by the small disk

which is less than what one would expect to be produced on the basis of reduced C_N . It is unfortunate that moment data from other sources could not be located, however the excellent agreement achieved with C_N is very encouraging for further development of water tunnel force testing techniques.

The final static correlation to be presented is for water tunnel tests of the 1/40-scale E-7 three-dimensional uncambered model (Ref. 6) as compared with a 1/9-scale model wind tunnel test (Ref. 10). In addition to the flat disks just discussed, the E-7 model was used in the development described in Ref. 6 for the water tunnel balance. The model as shown in Fig. 3-7 was fabricated to an accuracy of ± 0.001 in. and was thus very representative of the 1/9-scale model of Ref. 10. Comparisons of the HFF water tunnel and 1/9-scale test results are shown in Fig. 5-8 for both C_N and C_m vs α . With exception of a higher C_{Nmax} obtained with the 1/9-scale model, the HFF C_N results show excellent agreement. Consistent with previous discussions, this disagreement is attributed to Reynolds Number effects. With regard to the C_m comparison, the trends are very similar where displacement of the HFF data below 30° was attributed to cutting away of the body to accommodate mounting to the balance (See Fig. 3-7). Above 30° , the data agree remarkably well in both trend and magnitude.

In summary, the static correlation of ADF wind tunnel and HFF water tunnel force and moment results with other reliable sources of data has shown that both test techniques give reasonable results. In general full-span testing in the HFF provides very good force and moment data that may be slightly low, particularly near C_{Nmax} , as a result of Reynolds Number effects. Semi-span testing in the ADF provides better normal force data because of a higher Reynolds number capability, but pitching moment data are off as a result of centers of pressure which are too far aft.

5.2 DYNAMIC CORRELATIONS

In addition to model and tunnel geometry as well as flow parameters, the aerodynamic force and moment correlations just discussed above are further complicated in the case of dynamic test conditions due to the effects of time history. This means that for large amplitude model motions in which the changes in forces are no longer small in relation to the mean forces, the point at which motion begins, the rapidity of the motion and its amplitude are all important parameters. In addition, various combinations of these parameters are important which formed the basis for the dynamic testing of the large scale straked wing model at low speeds as reported in Ref. 5. This data base was therefore used as the standard by which to measure the ability of

small scale testing to produce representative estimates of non-linear dynamic forces and moments.

5.2.1 Correlation of Dynamic Normal Force Data

The philosophy that was followed in making the dynamic normal force correlations was to relate the dynamic characteristics back to a common steady base. In this way, bias due to miss-match in steady characteristics could be minimized. Dynamic data were also correlated on the basis of the incidence time histories encompassing similar major steady flow transition points such as strake vortex burst and C_{Nmax} .

An example of shifting to a common steady characteristic is shown in Fig. 5-9 where a three-way comparison is made between ADF, HFF and NLR (large scale) C_N vs α results. The common steady curve was chosen as that from the ADF test. In Fig. 5-9a, the unshifted dynamic loops are shown for similar non-dimensional maximum pitch rates, $\dot{\alpha}$, and similar starting and peak angles that straddle vortex burst and reach close to static C_{Nmax} . Fig. 5-9b shows the results after all loops are shifted to start on the ADF static curve. As can be seen the correlations are significantly improved where the HFF data shows better agreement with the NLR results.

A second example of shifting to the ADF static curve is shown in Fig. 5-10 for a higher incidence range between vortex burst and static C_{Nmax} . In this case the NLR data are for a larger amplitude motion and hence a higher $\dot{\alpha}$ value since all sets have about the same reduced frequency, k . Fig. 5-10a shows the unshifted data where the correlation is again not very good. In Fig. 5-10b, the data are all shifted to the ADF static curve and the correlation is definitely improved. In fact both ADF and HFF loops fall inside of the larger NLR loop as they should. Again, the HFF loop appears to show better agreement with the NLR data. Comparison with a smaller amplitude NLR loop at the same $\dot{\alpha}$ is shown in Fig. 5-11b for shifted data. In this case, the NLR loop is enclosed by the HFF loop but not by the ADF loop thus further indicating better agreement for the HFF data.

A third case is shown in Fig. 5-12 for a higher amplitude motion similar to that in Fig. 5-9, which starts above vortex burst and extends well beyond static C_{Nmax} . The $\dot{\alpha}$ values are also similar to those for the runs shown in Fig. 5-9. In this case, the unshifted data show the best correlation, however, the HFF and ADF loops show excellent agreement with each other. The pitch-up portion of the shifted NLR data is in line with but lower than the small scale data, whereas the pitch-down portion shows a lower level for minimum dynamic C_N . Since both small scale test results agree and each has a different support system as well as a different motion time history (pitch/pulse for the

HFF data and oscillatory for the ADF data), this phenomenon for negative pitch rate could be attributable to Reynolds number effects; however, this is not believed to be the case.

Returning to the unshifted data in Fig. 5-12a, it will be noticed that the dynamic maximum and minimum values of C_N tend to agree very well between all three data sets. It has been shown with the NLR data (Ref. 5) that increasing Reynolds number tends to produce an increased static level of C_N between vortex burst and C_{Nmax} . Thus, shift of the NLR dynamic loop to match the static ADF curve in Fig. 5-12b is a result of Reynolds number differences between the large and small scale data. The implication of Fig. 5-12a is that the absolute levels of dynamic maximum and minimum values of C_N for a given configuration are constant if (1) the non-dimensional pitch and incidence amplitude are equal, (2) the starting angle occurs between vortex burst and static C_{Nmax} and (3) the peak angle exceeds static C_{Nmax} angle. If this is the case then two different loops from the same test that have different starting and peak angles but satisfy the above three conditions, should have very similar loops. This is indeed the case for the HFF model as shown in Fig. 5-13, where the unshifted and shifted dynamic C_N data are presented in Fig. 5-13a and Fig. 5-13b respectively. The only difference between the two data sets is that the starting angle is 24° in one case and 32° in the other as shown in Fig. 5-13a. When the second set for the higher starting angle is shifted 8° to coincide with the first set in Fig. 5-13b, it is seen that the loops are almost identical with exception of the starting point.

On the bases of the above observation, it is postulated that under these flow conditions where the flow is still vortical but the vortex structure has begun to break down, kinematic effects of the dynamic flowfield created by model motion tend to dominate over viscous effects. In addition, the effects due to semi-span testing, balance/support interference, wall interference and blockage which are important in static testing in this flow regime, are not so important for dynamic testing under these flow conditions.

The dominance of kinematic effects for separated flows can be demonstrated on the basis of order-of-magnitude analysis for flow over the upper wing surface. The viscous force magnitude can be defined as

$$F_v \approx \mu \frac{V}{\delta} \quad \text{for attached flow}$$

$$\approx \mu \frac{V}{MAC} \quad \text{for separated flow}$$

where μ is the fluid viscosity, V is the free-stream velocity, δ is the nominal boundary layer thickness on the upper surface and MAC is the wing mean aerodynamic chord. The unsteady kinematic force magnitude due to model motion can be defined as

$$F_K \approx \rho V \dot{\alpha} \quad \text{for attached or separated flow}$$

where ρ is the fluid density and $\dot{\alpha}$ is the model pitch rate. The ratio of unsteady kinematic and viscous forces is therefore

$$(F_K/F_V)_A \approx \frac{\delta^2 \rho \dot{\alpha}}{\mu} \quad \text{for attached flow} \quad (5-1a)$$

$$(F_K/F_V)_S \approx \frac{MAC^2 \rho \dot{\alpha}}{\mu} \quad \text{for separated flow} \quad (5-1b)$$

where it is apparent that a significant difference exists between attached and separated flows. In fact the ratio of the parameter for attached and separated flows becomes

$$\left(\frac{F_K}{F_V}\right)_A / \left(\frac{F_K}{F_V}\right)_S \approx \left(\frac{\delta}{MAC}\right)^2$$

which indicates that viscous forces are very unimportant for unsteady forces produced by rapidly moving models in separated flows. However, this analysis also points out that since δ is on the order of wing thickness in attached flow, the dominance of viscous forces is as great in attached flow as that of kinematic forces in separated flow. This concept will be very useful in discussing the effect of various parameters on unsteady airloads produced on moving wings in the remainder of this report.

In summary, good agreement has been demonstrated between dynamic C_N results obtained with the small scale models and the NLR model. Correlations were made at the higher frequency of the small scale tests at various incidence ranges and amplitudes based on matching the starting point static conditions. In general, the HFF results tended to agree better with the NLR data than did the ADF results at the lower incidence ranges. At the higher range where the model motion was confined to separated flows, good agreement was achieved between all three results without shifting to match the starting point static conditions. This change in characteristic was attributed to the change in the relationship between kinematic and viscous forces for dynamic model motion.

5.2.2 Correlation of Dynamic Pitching Moment Data

The comparisons of dynamic pitching moment coefficient (C_m) results from the small scale tests and the NLR results were made only on the basis of shifted plots. The large discrepancies noted earlier in the static C_m results rendered the unshifted comparisons useless. Also, because the dynamic C_m loops are thin, comparisons were made at only two small scale conditions,

(1) a low incidence range from 8° to 40° and (2) a high incidence range from 24° to 56° . In both cases the highest small scale frequency was used, $k = 0.0704$ and 0.0748 for the ADF and HFF tests respectively.

The comparisons of ADF and HFF C_m data with shifted NLR results are shown in Fig. 5-14 for the low incidence range, 8° to 40° . In Fig. 5-14a, the ADF data agree quite well with NLR results, however, the latter were shifted down by -0.04 . The pitch-up data show the best agreement which, along with the good agreement of unshifted C_N data in Fig. 5-9a, indicate an accurate representation of the center of pressure of the unsteady C_N component. The pitch-down trend is almost identical to the pitch-up trend for the ADF data where as C_m is higher for the NLR data. The lower level of ADF C_N results on pitch-down as compared with the unshifted NLR data in Fig. 5-9a, however, tends to offset the C_m difference and again yields a good estimate of the unsteady C_N component center of pressure.

The HFF unsteady C_m results do not show quite as good agreement with NLR data in Fig. 5-14b. In this case, however, the NLR data are not shifted as a result of the excellent agreement between static C_m data up to about 24° as shown in Fig. 5-4. The differences in the unsteady C_m data in Fig. 5-14b are due primarily to differences in the unsteady C_N data as are shown in Fig. 5-9a. Comparing the maximum incidence conditions for HFF and NLR, the difference in the unsteady centers of pressure for the two results using the C_N and C_m data is about 1% of the root chord. Thus, it can be seen that the disagreement shown in Fig. 5-14b is due mostly to static C_N offset. With regard to direction of rotation in the unsteady C_m loop the lower portion of the HFF loop has the same counter clockwise direction as the NLR data. However, the small clockwise loop at higher angles in the HFF data does not appear in the NLR loop. The clockwise direction is indicative of more highly separated flow fields which for the HFF model probably exist as a result of the low Reynolds number.

The effect of highly separated flows is seen in Fig. 5-15 where the ADF and HFF data are compared with shifted NLR results at the higher incidence range, 24° to 56° . In this case, all three dynamic loops are dominated by clockwise rotation with small counterclockwise loops located at the lower portion of the incidence range. The agreement is quite good for both ADF and HFF data as compared with the NLR results. The ADF loop shows better agreement with regard to depth whereas the HFF loop shows better agreement with regard to shape. The improvement of C_m correlation at this incidence range is attributed to the dominance of kinematic forces in the separated flow regime as was discussed previously for C_N in Section 5.2.1.

In summary, the correlations of dynamic C_m results from the ADF and HFF tests with large scale data from the NLR test have shown that reasonable trends are obtainable with small scale testing. The correlation of centers of pressure for unsteady forces was better than for C_m results. Similar to observations made for normal force, it was also seen that the moment correlations were further improved in the separated flow regime where kinematic forces dominated over viscous forces for dynamic model motions.

6.0 DISCUSSION OF RESULTS

Several items that affect the dynamic forces experienced by rapidly moving models will be discussed in this section. First, time history effects will be covered which will include repeatability, oscillatory motion vs pitch/pulse motion, frequency and pitch rate, starting and peak angles as well as incidence range. Second, the test medium will be discussed which will address water tunnel vs. wind tunnel static and dynamic testing. Third, Reynolds number effects will be discussed with primary emphasis placed on static testing and the relationship between attached and separated flows for dynamic testing. Fourth, three-dimensional effects will be considered using the two E-7 models to demonstrate this influence in both static and dynamic testing. Finally, planform effects will be discussed using the four flat plate models, the straked wing, 55° and 70° deltas, and the cranked wing, as examples.

6.1 TIME HISTORY EFFECTS

Two of the most important aspects of dynamic testing are repeatability and associated data scatter. In the case of unsteady forces and moments produced by large amplitude model motions, time history effects introduced through frequency and pitch rate have a significant impact. This impact is different whether tests are conducted in a wind tunnel or water tunnel.

Results obtained from oscillatory testing of the straked wing in the ADF wind tunnel are shown in Fig. 6-1. The plots show continuous oscillatory traces for many consecutive cycles of C_N , C_l and C_m vs α at the two frequencies, $k = 0.0249$ and 0.0704 . Based on the static value of C_{Nmax} , the scatter in C_N at both frequencies is less than 10%, however, buffeting is more evident at the low frequency than at the high frequency. This same phenomenon has been observed for other models as well as in the NLR straked wing results. It is believed that this effect is a result of the stabilizing influence of higher pitch rate on the large scale turbulent flow fields. Scatter of the C_l and C_m data are similar to the C_N results in nature, however, the percentage of C_m scatter is significantly higher at about 20% relative to the maximum value. Recasting the C_m scatter into center of pressure location, the variation is reduced to about 1% of the root chord which is more relevant for design purposes.

Repeatability for testing the 55° delta wing in the ADF wind tunnel is shown in Fig. 6-2 for $k = 0.0269$ and 0.0769 . Although this model and its flow fields are significantly different, the trends in scatter are similar to those observed in Fig. 6-1.

Water tunnel results are shown in Fig. 6-3 for dynamic tests of the straked wing. In this case, since the model motion is

pitch/pulse, three pulses are shown which were averaged together to obtain the final results presented and discussed in this report. The plots show C_N and C_m data for the three pulses in a format similar to that used for the oscillatory ADF data in Figs. 6-1 and 6-2. Significant differences are seen between the low and high frequency results, $k = 0.0268$ and 0.0748 respectively. At $k = 0.0268$, the buffeting characteristics are similar to those observed for the ADF test in Fig. 6-1 but at a higher amplitude of about 15% of static C_{Nmax} . At the higher frequency, $k = 0.0748$, significant large amplitude oscillations occur which are not seen in the ADF results. This phenomenon has been identified as the result of the viscous forces produced by model motion which are of significant amplitude due to high density of the water (Ref. 6). It has also been observed for model motion in still water to have a nature similar to that seen when the water velocity is 0.8 fps. Because this effect is peculiar to water tunnel dynamic testing, it will be discussed in more detail below under Test Medium. The higher frequency results shown in Fig. 6-3 were obtained by digitally filtering the recorded data, however, it was impossible to remove all of the viscous oscillations without destroying the desired dynamic forces and moments. The use of three pulses for averaging does not yield a high statistical accuracy as is evident in Fig. 6-3; thus, future high frequency tests should use more pulses to obtain better averages.

Results for water tunnel tests of the 55° delta are shown in Fig. 6-4 for $k = 0.0276$ and 0.0828 . With exception of one C_N pulse at high frequency, the data are more repeatable for this model as compared with the straked wing. The viscous oscillations peculiar to water tunnel testing are not so pronounced for this model, however, for the 70° delta and cranked wing the oscillations are as apparent in the data as for the straked wing results. Therefore the effect is believed to planform dependent.

The influence of model motion time history with regard to what happens before and after a pitch excursion is shown in Fig. 6-5. Results from ADF wind tunnel tests of the straked wing at $k = 0.0704$ are included for a single pitch/pulse and the averaged oscillatory run. As can be seen, the two C_N loops are nearly identical which has also been demonstrated with the large scale NLR results for the straked wing. The value of dynamic C_{Nmax} , however, is slightly higher for the oscillatory case. Thus, for correlation purposes, there is essentially no difference between oscillatory and single pitch/pulse results with the exception as noted.

Frequency effects are demonstrated for the four basic models in Figs. 6-6 through 6-9. Low and high frequency C_N vs α loops are shown for the maximum amplitude motion of 48° . The incidence range was chosen so as to have about the same relationship with

vortex burst and static C_{Nmax} . Straked wing C_N results are shown in Fig. 6-6a for ADF test at $k = 0.0249$ and 0.0704 which, with the amplitude of 48° , yields non-dimensional pitch rates of $\dot{\alpha} = 0.0150$ and 0.0290 . Water tunnel results for the straked wing are shown in Fig. 6-6b at $k = 0.0268$ and 0.0748 and $\dot{\alpha} = 0.0111$ and 0.0311 . Both sets of data show similar trends which significantly expand the C_N loops with frequency, however, the absolute values are different between ADF and HFF results. For this model, the loops are generally smaller for the HFF results.

Fig. 6-7 shows similar results for the 55° delta wing where the trends with frequency are the same but the loops are slightly larger for HFF data. The 70° delta wing results shown in Fig. 6-8 are similar to the 55° delta wing data in Fig. 6-7, however, the loops are definitely larger for the HFF data. Finally, the cranked wing ADF results in Fig. 6-9a are almost identical with those for the 70° delta wing in Fig. 6-8a as would be expected due to planform similarity. In Fig. 6-9b, the HFF cranked wing C_N loop is very close to the 70° delta wing data in Fig. 6-8b for the low frequency case but significantly smaller at the high frequency. The difference between ADF and HFF testing will be further analyzed under the subsection Test Medium.

The effect of starting and peak angles is of utmost importance in the development of unsteady forces and moments on dynamically moving models. This effect for increasing the peak angle while holding the starting angle fixed is demonstrated in Fig. 6-10 with ADF results at the two frequencies, $k = 0.0249$ and 0.0704 . The starting angle is fixed at 8° which is in the linear attached flow regime. The peak angle values are 24° , 40° and 54° which correspond respectively to conditions just beyond static vortex burst, just beyond static C_{Nmax} and well into fully stalled flow. Since frequency is held constant at two values, the non-dimensional pitch rate, $\dot{\alpha}$, is different for each amplitude. As can be seen in Fig. 6-10, as the peak angle is increased, the vortex flow regime characteristics are extended with positive $\dot{\alpha}$ into the burst vortex region at the higher frequency for all C_N , C_l and C_m results. The static characteristics are simply displaced to higher levels at the lower frequency with positive $\dot{\alpha}$. For negative $\dot{\alpha}$, larger C_N , C_l and C_m under shoots are noted with increasing peak angle at the higher frequency. At the lower frequency with negative $\dot{\alpha}$ there again seems to be a downward displacement of the static characteristics.

The effect of maintaining a peak angle of 54° while increasing the starting angle is demonstrated in Fig. 6-11 for the ADF test of the straked wing. In this case the excursions of C_N , C_l and C_m with increasing starting angle are significantly decreased as a result of (1) starting the pitching motion in more deteriorated flow fields and (2) a reduction in $\dot{\alpha}$. The fact that positive pitch rate starting at 24° leads to a significant

increase in C_N and C_l verifies the idea that positive α tends to organize the highly turbulent flow fields. The opposite trend for negative α verifies that the turbulent flow fields are more disorganized with pitch-down motions.

The same effects of starting and peak angles are shown for the ADF test of the cranked wing in Figs. 6-12 and 6-13. The starting angle was chosen at 16° so as to maintain a similar relationship with flow breakdown points as existed for the results in Figs. 6-10 and 6-11. The maximum angles for fixed starting angle were 32° , 48° and 64° which respectively corresponded to just above static vortex burst, just above static C_{Nmax} and well into stalled flow. Likewise, with starting points at 16° , 32° and 48° and a fixed peak angle of 64° , the flow field excursions began in vortex flow, burst vortex flow and highly stalled flow. The C_N and C_l results in Figs. 6-12 and 6-13 show similar trends to those exhibited by the straked wing in Figs. 6-10 and 6-11. The C_m loops are more exaggerated in comparison with the straked wing results as a result of an expanded scale, however the trends are more visible. All C_m loops tend to show clockwise motion in the highly separated regions above about 38° and counterclockwise in the vortex dominated flow regions below that angle. In addition, small counterclockwise loops exist near the peak of 64° which are more pronounced at the lower frequency.

The development of C_N and C_l high frequency loops for a fixed starting angle and increasing peak angle in either Fig. 6-10 or 6-12 can be used to demonstrate the interplay between model incidence time history and static flow transition points. The low amplitude excursion up to just passed static vortex burst in Fig. 6-10 ($k = 0.0704$) shows only a small C_N loop near the peak and is obviously dominated by unburst vortex flow fields. Extending the amplitude up to 40° just beyond static C_{Nmax} yields a loop that is significantly more open as a result of (1) penetrating further beyond the static vortex burst point and (2) an increased pitch rate due to a higher amplitude but fixed frequency. The loop opens even more when the maximum angle is increased to 54° . In this case, the vortex flow characteristic is extended to a higher angle with positive α and stalled flow is conversely extended to a lower angle with negative α .

It is interesting to note in both Figs. 6-10 and 6-12 for the highest amplitude and highest frequency, that the gain in dynamic C_{Nmax} for positive α over that of the middle amplitude run is less than the C_N increment loss for negative α . This asymmetry is attributed to the tendency for lag times to be less for the higher velocity "attached" flows dominating on pitch-up than for the highly chaotic stalled flows that dominate on the pitch-down. Thus, transitions to vortex burst and total separation tend to be less delayed with positive pitch rate than are the transitions from total separation and vortex burst with negative pitch rate.

Finally, an all important question to be addressed from the standpoint of testing procedures for time history effects is "can similar incidence range results at similar $\bar{\alpha}$ values be obtained with smaller amplitude motions"? This is more clearly stated with help of the results shown in Fig. 6-14 for the straked wing as tested in the ADF wind tunnel. For the low frequency results in Fig. 6-14a, $k = 0.0249$, the large amplitude motion from 8° to 56° with $\bar{\alpha} = 0.0105$ is shown as a dashed line; and the high frequency low amplitude motion results, $k = 0.0804$ and an incidence amplitude of 16° which yields $\bar{\alpha} = 0.0100$, are shown as solid lines. Ideally if incidence and $\bar{\alpha}$ are the driving parameters then an envelop produced from the low amplitude higher frequency loops should correlate very well with the large amplitude lower frequency loop. This is seen to be nearly true in Fig. 6-14a. For the higher frequency large amplitude case for $\bar{\alpha} = 0.0290$ in Fig. 6-14b, the runs of a smaller amplitude of 32° were made at the same reduced frequency, $k = 0.0704$, hence the $\bar{\alpha}$ values were smaller at 0.0190. In this case, the envelop produced by the 32° amplitude runs generally fell inside that for 48° amplitude as it should.

Similar plots are shown for the HFF water tunnel test of the straked wing model in Fig. 6-15. In this case, the low frequency high amplitude loop for $\bar{\alpha} = 0.0111$ in Fig. 6-15a is well represented by the envelop of the low amplitude high frequency loops for $\bar{\alpha} = 0.0104$. A similar trend to that in Fig. 6-14b is seen in Fig. 6-15b with the high frequency high amplitude loop for $\bar{\alpha} = 0.0311$. Fig. 6-16 shows similar HFF results for the higher incidence range extending from 24° to 64° but for the same values of k and $\bar{\alpha}$ depicted in Fig. 6-15. Again, these results show trends similar to those in Fig. 6-15 with exception that the lower level of C_N on the 48° amplitude pitch-down in Fig. 6-16b is further removed from that for the 32° amplitude runs in comparison with Fig. 6-15b.

On the basis of the above comparisons it appears that large amplitude motions can be simulated with low amplitude tests but at similar incidences and $\bar{\alpha}$ values as long as $\bar{\alpha}$ is low, ie in the 0.01 range. As $\bar{\alpha}$ increases, the simulation of dynamic C_{Nmax} characteristics on pitch up is good where as low C_N values on pitch down are not low enough for the small amplitude runs. This point can be further clarified by comparing the large scale NLR data at higher k values with the HFF results in Fig. 6-15b for $\bar{\alpha} = 0.0311$. For reference, NLR data for $\bar{\alpha} = 0.0225$ and lower amplitude are compared with the HFF loop in Fig. 6-17a. As can be seen, this comparison is similar to that shown in Fig. 6-15b for a similar $\bar{\alpha}$ value of 0.0207 for the smaller amplitude runs. In Fig. 6-17b, the NLR results for a higher frequency and $\bar{\alpha} = 0.0280$ agree better at dynamic C_{Nmax} with the HFF loop on pitch-up. On pitch-down, however, the NLR results match the HFF data at about 40° but are higher until they cross again at about 15° . In fact, the pitch-down characteristics of the NLR data in both

Figs. 6-17a and b are nearly identical which indicates a strong influence of time history since the high incidence loop at lower $\bar{\alpha}$ has a larger amplitude but similar peak angle to that at higher $\bar{\alpha}$ but lower amplitude.

The reason for the inability of the low-amplitude runs to be able to match the dynamic C_N undershoot at higher amplitudes but similar $\bar{\alpha}$ is the time history effect of where the pitch-down begins. If pitch-down begins above static C_{Nmax} , in the stalled flow regime, then the higher lag permits C_N to fall much lower than if the pitch-down begins below static C_{Nmax} . This is evident in the NLR data in Fig. 6-17b where the loop that begins at 28° and reaches 48° does show sufficient C_N undershoot. The NLR loop that begins at 21° and ends at 40° , however, does not penetrate the stalled region enough to achieve sufficiently chaotic flow which will produce the desired C_N undershoot needed to simulate the large amplitude motion. Thus, the highly non-linear nature of the chaotic flows which allows them to persist to much lower angles with pitch-down cannot be simulated if the model motion time history does not take it into that flow regime.

In summary, time history effects have been presented which show that their influence is of major importance in the development of dynamic forces and moments on moving models that represent rapidly maneuvering aircraft. Repeatability was shown to be better for the ADF oscillatory data as compared with the HFF pitch/pulse results. For correlation purposes, it was also found that pitch/pulse and oscillatory model motions gave essentially the same results with the exception that dynamic C_{Nmax} was slightly higher for the latter type motion. Frequency effects at constant amplitude motion were shown to be consistent for both ADF and HFF results with a trend to expanding the C_N dynamic loops with increasing frequency for all models tested. The effect of starting and peak angles was demonstrated to be highly non-linear as a result of varying lag characteristics which were determined by the flow field types encountered by the model during its motion time history. As a result, it is possible to simulate pitch-up dynamic C_N overshoot characteristics of large amplitude motions with smaller amplitude runs but of similar $\bar{\alpha}$ values. The dynamic C_N undershoot on pitch-down, however, cannot be fully simulated in this way for large amplitude motions that significantly exceed the point of static C_{Nmax} . This is due to the non-linear nature of the time history effects in highly chaotic turbulent flows that exist over a highly stalled wing.

6.2 TEST MEDIUM

This subsection is devoted to describing the differences between the dynamic testing of small scale models in small wind tunnels or water tunnels and will not discuss Reynolds number

effects which will be addressed in subsection 6.3. The following discussions will be concerned with the kinematic consequences of dynamic testing in a low velocity, high density fluid as opposed to a high velocity, low density fluid.

One of the primary motives for dynamic testing in water tunnels is the reduction of frequency and hence inertial forces due to model accelerations that are permitted with the low test speeds which are on the order of 1 fps. Compared with testing in a wind tunnel at 100 fps, dynamic similarity of k and C can be achieved in the water tunnel at 1/100 of the frequency used in air. Thus for the same size model, a frequency of 3 Hz in the wind tunnel at 100 fps is simulated in the water tunnel with a frequency of 0.03 Hz at 1 fps. This expansion of the time scale by a factor of 100 significantly reduces the complexity and difficulties of data acquisition as well as data reduction. High recording rates are not needed (2 samples per second are sufficient) and model inertia forces due to accelerations are essentially zero, ie $\propto 10^{-4}$.

As a result of testing at low velocities, dynamic pressures in the water tunnel are lower than in the wind tunnel by about a factor of 10 relative to 100 fps in air. However, sufficient sensitivity can be achieved in a practical balance design such as was developed at General Dynamics (Ref. 6), so that forces and moments for developing aerodynamic coefficients can be measured with reasonable accuracy.

Initial static tests in the water tunnel as were discussed in Section 5.0 were very encouraging in spite of the low Reynolds number of less than 10^5 . However, the first attempts at dynamic testing were not so successful as described in Ref. 6. Unexpected large amplitude oscillations that increased with model pitch rate were encountered at frequencies as low as 0.01 Hz and became intolerable at frequencies approaching 0.1 Hz. At first it was suspected that the oscillations were due to virtual mass of the much higher density of water ($\times 10^3$ relative to air). However, a reduction of frequency by 10^{-2} further reduced the virtual mass effect in water by 10^{-1} relative to air since it scaled with frequency squared.

An investigation was then conducted as described in Ref. 6, to determine both the source and nature of these oscillations. Tests conducted with the water velocity at zero showed that the oscillations were still present but were more systematic for a model pitch pulse. It was also possible to see a trend with pitch rate within the model motion time history where pitching moment oscillation amplitudes seemed to vary in proportion to pitch rate.

Typical results are shown in Figs. 6-18, 6-19 and 6-20 for the time history of pitching moment for the straked wing model in

executing a pitch/pulse of 48° amplitude in the water tunnel at zero velocity. The pitch/pulse cycle times and frequencies are 86.2 sec (0.0116 Hz), 28.7 sec (0.0348 Hz) and 15.3 sec (0.0654 Hz) respectively in the three figures. The time histories show the static contribution of model weight, which is more evident in Fig. 6-18, and the dynamic oscillations about the static mean value which are dominant in Fig. 6-20. As will be noticed, the amplitude of oscillations are greatest at the maximum pitch rate portions of the cycles and overall for the shortest cycle time of 15.3 sec. The amplitudes of oscillations about the mean tend to scale inversely with the cycle time since the amplitude is constant in the three figures. Other tests were run as discussed in Ref. 6 where the pitch rate was held constant but amplitude varied. In these tests, scaling of the oscillations with pitch rate was shown to still be valid.

Another peculiarity of the oscillations that can be observed in Figs. 6-18 through 6-20 is the apparent reduction in frequency with a decrease of cycle time. This is not an effect of sampling rate since it is identical in all three cases. Nor is it what would be expected on the basis of conventional vortex shedding frequencies, where as the velocity of wing edges increase with increased pitch rate, the frequencies of the oscillations also increase. As pointed out in Ref. 6, this phenomenon is attributed to the effect of wing edge velocity on vortex shedding structure. At very low pitch rates in Fig. 6-18, it is postulated that small vortices are shed from the edges in a weak shear layer that does not roll up into larger vortices. It also appears that in Fig. 6-19 at the intermediate cycle time, the frequency might be higher by virtue of a higher edge velocity as would be expected. At the shortest cycle time in Fig. 6-20, however, the frequency has dropped considerably which indicates a change in vortex structure at the higher edge velocity. In this case it is suspected that the shear layer is of sufficient strength to cause the small individual vortices to roll-up into a larger vortex structure which results in the lower frequency.

Since this phenomenon is proportional to pitch rate, which by virtue of similarity requirements is proportional to velocity, it is possible to separate the oscillations from the flow induced forces of interest which are proportional to velocity squared. However, in the case of the General Dynamics water tunnel, the maximum velocity is limited to about 1 fps. Hence filtering of the recorded data and limiting the maximum pitch rate were used to circumvent this problem. This also indicates that for dynamic testing at lower velocities of about 0.25 fps such as those used in conventional flow-visualization testing, these oscillations will become 4 times larger relative to the desired aerodynamic forces and moments as compared with 1 fps test velocity.

Examples of pitching moment data, C_m , for the straked wing performing pitch/pulse cycles similar to those in Figs. 6-18, 6-

19 and 6-20, are shown in Figs. 6-21, 6-22 and 6-23 for a water velocity of about 0.8 fps. The filtered (solid) and unfiltered (dashed) time history results are shown for cycle times of 87.7 sec (0.0114 Hz), 30.0 sec (0.0333 Hz) and 16.7 sec (0.0600 Hz) respectively. Filtering consisted of three forward and three backward passes (to remove time lag induced by the filter) of a 0.25 Hz low-pass digital filter (see Section 3.7). As can be seen, the filtered data in Figs. 6-21 and 6-22 for the lower frequency runs show a reasonable correlation with the apparent mean of the unfiltered data. There is sufficient frequency and amplitude separation for these two cases, however, for the third case at the highest frequency, the oscillations are dominant, particularly in the pitch-down part of the cycle. Also, the lower frequency of the oscillations makes it doubly difficult to separate out the data of interest through low-pass filtering.

As a result of the above investigation, it was decided that for dynamic water tunnel testing in this study, the minimum pitch/pulse cycle time would be limited to about 30 sec. for a water velocity of 0.8 fps. Thus, all results processed for dynamic testing in the ADF wind tunnel were likewise limited to about 2.5 to 3.0 Hz so as to be compatible with the water tunnel data base. This was not too restrictive, however, since the ADF data for frequencies greater than about 4 Hz were not reliable due to over torquing of the stepper motor and loss of incidence correlation with stepper motor position.

Before continuing with direct comparisons of ADF and HFF dynamic results, it is helpful to first make direct comparisons of the steady results. These are shown for the C_N vs α data in Fig. 6-24 for the straked wing planform. The two sets of data show a very good overall agreement with exception of the apparent displacement in incidence below about 20° . This displacement of the HFF data has already been attributed to balance and support interference in Subsection 5.1 and is hence not a result of test medium. The excellent agreement in the vicinity of C_{Nmax} and beyond indicates that there may be cancelling effects as will become evident in the following discussions.

Steady C_N results for the ADF and HFF tests of the 55° delta wing were already compared in Fig. 5-5. In this case, there is also an apparent displacement in incidence at lower angles, however, the non-zero value for the ADF data at $\alpha = 0^\circ$ is suspicious. The most notable difference is seen at C_{Nmax} and beyond where there seems to be a constant displacement in C_N and α . In the earlier discussions in Subsection 5.1, this difference at high incidence was attributed to Reynolds number effects due to the lower leading edge sweep angle of 55° . Thus, it is not felt that any other effects due to test medium are influencing the results in Fig. 5-5.

For the 70° delta wing steady force characteristics, a four-way comparison of ADF, HFF, Wentz and Chang/Muirhead results in Fig. 5-6 was discussed earlier in Subsection 5.1. Most of the differences between ADF and HFF data were attributed to balance/support interference based on comparisons with the Wentz and Chang/Muirhead data sets. In addition, a convincing argument was made for the effect of leading edge radius on forces induced by vortex flows. This was based on (1) the close matching of ADF and HFF data up to about 30° where both models had rounded leading edges and (2) the close matching of Wentz and Chang/Muirhead data up to about 28° where these models had sharp leading edges. No significant effects were attributed to the test medium for this model.

Finally, a comparison of C_N vs α results for ADF and HFF tests of the cranked wing is shown in Fig. 6-25. The trends seen in this figure are similar to those shown for the 70° delta in Fig. 5-6 as expected due to dominance of the 70° sweep on the inboard part of the cranked wing. It should be noted that in comparison with the 70° delta, the difference between the ADF and HFF results for the cranked wing do not exhibit such drastic changes in character. Instead, they depart smoothly before C_{Nmax} and merge smoothly after C_{Nmax} .

Returning to the static characteristics of the straked wing, it was mentioned that the excellent agreement between ADF and HFF data near C_{Nmax} and above could be a result of cancelling effects. The lower level of C_{Nmax} for the 55° delta was attributed primarily to Reynolds number effects because of the lower sweep. The higher levels of C_{Nmax} for the 70° delta and the cranked wing were attributed to balance/support interference. It is therefore felt that the straked wing experienced a combination of these effects where (1) the highly swept straked section tended to develop a higher normal force due to balance/support interference and (2) the lower swept outboard wing broke down at a lower angle and produced a lower normal force because of Reynolds number effects. Noting the similarity of differences in C_{Nmax} for the 55° and 70° deltas, it is reasonable to expect these two effects to cancel for the straked wing.

Comparisons of dynamic ADF and HFF C_N results for the straked wing are shown in Figs. 6-26 for two frequencies and two amplitudes with the same starting angle. In order to minimize effects due to static correlation deficiencies, the dynamic HFF data were shifted so as to match the loop starting point with the corresponding point on the ADF static curve. (This is the same procedure used in developing Figs. 5-9 through 5-12.) Thus, the C_N and α scales in this figure and Figs. 6-27, 6-28 and 6-29 for the other three models, all correspond to the ADF data. For reference purposes, however, the shifted HFF static curve is always included.

The dynamic straked wing results in Figs. 6-26 have all been previously discussed to a certain extent, particularly in regard to correlations with the NLR data. In summary, it can be seen that the C_N loops obtained with the ADF tests are larger than those from the HFF tests. In comparing with the NLR data, it was shown in Subsection 5.2 that the HFF results gave the best correlations. However, the irregularities in the HFF data, induced by the large amplitude oscillation at higher frequencies described earlier in this subsection are troublesome and are felt to have impact on these comparisons. A larger number of pitch/pulse data sets in the averaged HFF data would be very helpful in smoothing the dynamic loops.

The 55° delta wing results for similar conditions are shown in Figs. 6-27. The correlations at lower frequency with the shifted HFF data are excellent and are reasonable at the higher frequency. There are some similarities between these data sets in Figs. 6-27b and 6-27d and those for the straked wing in Figs. 6-26b and 6-26d.

Because of the large difference in the location of static C_{Nmax} for the 70° delta, a higher starting angle was used for the HFF results so as to preserve the relationship between the incidence range and static C_{Nmax} . The ADF conditions for a low and high frequency used a starting angle of 8° and two peak angles of 40° and 54° . The HFF conditions for similar k values had a starting angle of 16° and two peak angles of 48° and 64° . These results are shown matched at starting angles in Figs. 6-28 with the exception that low frequency data for the lower amplitude was not available from the ADF test, hence, Fig. 6-28a was left blank so as to preserve the format. Allowing for the irregularities in the water tunnel results, the comparisons in Fig. 6-29b are reasonable. Those in Fig. 6-28c and 6-28d are excellent for pitch-up but show significantly lower C_N undershoot levels for the HFF data on pitch-down. The differences in undershoot levels for both frequencies are very close in magnitude to the differences in static C_N levels at high angles, say at 60° . Thus, the disagreements are not a result of dynamic differences but of static differences instead. This is another graphic illustration of the coupling between static and dynamic characteristics.

Similar comparisons for the cranked wing are made in Figs. 6-29 where the starting angles were the same value of 8° . Because of significant differences in the static C_{Nmax} values the low amplitude range results in Figs. 6-29a and 6-29b from 8° to 40° do not show very good correlation between ADF and HFF data. This is due primarily to the maximum incidence for the HFF data being so close to the angle of static C_{Nmax} whereas for the ADF data that point is sufficiently exceeded to produce a more open loop. The higher amplitude results in Figs. 6-29c and 6-29d show

reasonable correlation, especially in the high frequency case. However, the width of the HFF C_N loop should be greater than that for the ADF data because of the larger difference between static C_{Nmax} and C_N at higher angles. This was demonstrated in the case of the 70° delta wing in Fig. 6-28. It is important to note that the dynamic undershoot characteristics during pitch-down match exceedingly well in both cases as do the static C_N levels above about 50° . This result in addition to that for the 70° delta wing, is further proof of the strong tendency of dynamic loops to be governed by the underlying static characteristics.

In summary, the effects of test medium, high-speed air vs low-speed water, do not seem to have any influence on static force data for the models tested other than Reynolds number effects. This is not true for dynamic testing where significant force and moment oscillations not seen in air were observed in the water tunnel dynamic data at frequencies as low as 0.01 Hz, even for zero water velocity. As a result, pitch rate limitations were imposed on the test conditions and low pass filtering was applied during data processing to remove the oscillations. Because of high frequencies required by testing in air at high speeds, frequency limitations were also encountered due to the high dynamic inertia loads on the driving stepper motor. Low pass filtering was also used in the ADF data processing to eliminate forces and moments resulting from structural dynamic effects. The correlation of dynamic C_N loops for the four basic models showed that the two test approaches agreed very well where static characteristics were closely matched. Where static data did not correlate, the displacements in dynamic data tended to track corresponding displacements in the static data.

6.3 REYNOLDS NUMBER EFFECTS

Reynolds number effects relative to small scale testing have been repeatably mentioned throughout the previous portion of this report. It is appropriate, however, to summarize these effects in a single discussion devoted to the subject.

The major influences of Reynolds number effects are felt in the steady forces and moments. Dynamic characteristics are in turn affected by the changes in static forces and moments through the close coupling of the static and dynamics for a given configuration. In most cases, differences noted in C_N and C_m loops have been tied back to original differences in the static characteristics. Reynolds number effects have not been observed as being directly important to dynamic forces and moments, thus the following discussion will be devoted to the effects in steady flow.

The NLR data base (Ref. 5) as previously mentioned, contained static force and moment data for the straked wing tested with two types of support systems at various speeds. The test with wire balance suspension gave results with minimum interference at two speeds of 25 m/sec and 66 m/sec which yielded Reynolds numbers of 1.4×10^6 and 3.7×10^6 . The test with the model supported by the dynamic driving system had much higher interference on the lower surface and was run at a higher speed of 80 m/sec with $R_e = 4.5 \times 10^6$. Fig. 6-30 shows the C_N and C_m results for these three test conditions where comparing the test in wires data provides a trend with R_e for a common support interference. As can be seen, the C_N curve at 66 m/sec for $R_e = 3.7 \times 10^6$ is higher over the incidence range tested as compared with the C_N curve at 25 m/sec.

The increase of C_{Nmax} with R_e shown in Fig. 6-30 is opposite to that shown by Soltani, Bragg and Brandon in Ref. 11 where they showed a decrease in C_{Nmax} with increase in R_e on a 70° sharp edged delta wing. Their results and conclusions are not believable because the data published by Chang and Muirhead (Ref. 8) showed that Wentz's 70° delta data (Ref. 7) was strongly influenced by support interference (see discussions relating to Fig. 5-6 in this report). Soltani, et al used Wentz's data as part of their verification of Reynolds number effects that they had measured, however, use of Chang and Muirhead's data would make this apparent R_e effect disappear.

Returning to Fig. 6-30, the C_m curves for the tests in wires show an aft movement of the center of pressure with increasing R_e . Most likely, this rearward shift of loading is a result of retarding the growth of separation on the lower swept main wing panel. A similar effect was discussed for the 55° delta wing (Fig. 5-5) where the HFF results at lower R_e had a lower level of C_{Nmax} that was attributed to higher separation on the lower swept wing.

Comparison of the NLR C_N data at 80 m/sec for static testing on the dynamic support system, with the test in wires data at 66 m/sec in Fig. 6-30 shows that the two data sets essentially agree with each other up to vortex burst. After that point, the 80 m/sec C_N data have a similar trend as the 66 m/sec test in wires results but at a lower level. Since the R_e values are so close in this comparison, most of the observed effect is attributed to support interference. The C_m data in Fig. 6-30 show a consistent trend with increasing R_e but the increments in the incidence range of about 30° to 40° are too large between the 66 m/sec data and that at 80 m/sec. This is again attributed primarily to support interference effects.

With the above trends noted for the NLR straked wing model test similar trends can be shown for the small scale results in cases where effects due to semi-span testing, support

interference, etc. can be separated out. The most obvious are the small scale straked wing models tested in the ADF and HFF. The ADF results for C_N in Fig. 5-3 show a similar relationship with the test in wires data at 25 m/sec as was shown between the test in wires data at 25 m/sec and 66 m/sec. That is, for $Re = 0.55 \times 10^6$ for the ADF results and $Re = 1.4 \times 10^6$ and 3.7×10^6 for the test in wires data, a consistent trend is shown with Re for similar support interference. The C_m data in Fig. 5-3 do not show a consistent trend, however, this was already attributed to semi-span testing effects.

The HFF results for C_N shown in Fig. 5-4 are compared with NLR data at 80 m/sec so as to retain similarity in support interference effects. The trend with Re is again similar to that shown in Fig. 5-3 where C_N is lower in the incidence range dominated by burst vortex flow up to static C_{Nmax} . For the C_m results, excellent agreement with the NLR data is seen up to about 22° and after about 40° . This trend is similar to that shown in Fig. 6-30 between the dynamic test static NLR data at 80 m/sec and the test in wires data at 66 m/sec. Thus, it is indicated that the differences in C_m in Fig. 5-4 between 22° and 40° are due mostly to the higher level of balance/support interference on the HFF model.

It is also possible that the good agreement between C_m data up to 22° in Fig. 5-4 is a result of cancelling effects. In Fig. 6-30, a slight reduction in C_m is seen in the NLR results for static tests on the dynamic support as compared with test in wires at 66 m/sec. Since the HFF support has greater interference than the NLR dynamic support, this effect could be large enough to offset the increase in C_m expected due to the low Re value of 0.06×10^6 in the water tunnel.

Similar trends observed for the straked wing were also observed for the 55° delta wing as a result of being a higher aspect ratio wing with lower leading edge sweep. Comparisons in Fig. 5-5 showed that C_N for the ADF test agreed very well with Wentz's data (Ref. 7) since both were at similar Reynolds number values of 0.45×10^6 and 0.58×10^6 respectively. The HFF C_N data taken at $Re = 0.05 \times 10^6$ were lower from C_{Nmax} up to about 38° where the two curves merged. This trend was identical to that observed for the straked wing. The C_m correlations were dominated by differences caused by semi-span testing, Reynolds number effects and balance/support interference.

In the case of the 70° delta comparisons in Fig. 5-6, less sensitivity was seen due to Reynolds number effects than for the straked wing or 55° delta. C_{Nmax} obtained from the ADF tests agreed well with Chang and Muirhead but these were at about the same Reynolds number of 0.6×10^6 and 0.7×10^6 respectively. However, C_{Nmax} also agreed well between the HFF data and Wentz which had a much higher Reynolds number difference of 0.066×10^6

and 1.1×10^6 respectively. In the final analysis of the 70° delta wing results, the primary differences in the four sets of data were attributed to support interference and leading edge sharpness rather than Reynolds number.

The correlation of HFF results for the 3-D E-7 model with 1/9-scale model data in Fig. 5-8 shows an amazing insensitivity to Reynolds number effects. For this comparison, R_e is 0.052×10^6 for the HFF test and 6.5×10^6 for the 1/9-scale test (both values are based on the MAC). The similarity of the C_N vs α curve for this model and the 70° delta indicates that a large amount of normal force on the E-7 is developed by vortex flow even though the wing sweep is only 60° . Thus, it is not surprising that Reynolds number does not play a dominant role. The same observation is true in the C_m correlations in Fig. 5-8 where an offset is present due to model differences at angles less than 30° .

In summary, Reynolds number effects have been observed mostly in the steady data where as the differences in dynamic results can be traced back to differences in the steady characteristics. The effects of lower Reynolds numbers were shown to decrease normal force on models at incidences where the flow is dominated by burst vortex type flow fields. Less sensitivity was seen for more highly swept wings of lower aspect ratio. The effects of lower Reynolds number on pitching moment were shown to move the center of pressure forward at all flow conditions, however, the magnitude of change was not significant and amounted to only about 1% of the root chord in the case of the straked wing.

6.4 THREE-DIMENSIONAL EFFECTS

Three dimensional effects were investigated on the E-7 configuration by testing a scaled 3-D model and a flat plate version in the HFF. Tests were conducted in steady flow and at two frequencies with an incidence range of 8° to 56° in unsteady flow. The flat plate model was fabricated from 0.050 in thick aluminum sheet in the projected planform shape of the E-7 configuration complete with nose and aft end (see Fig. 3-7). Thus, the flat plate model had an effective "strake" as represented by the flat nose.

Results of the steady test of the flat and 3-D models are shown in Fig. 6-31 for C_N and C_m vs α . Alpha increasing and decreasing data are shown for the 3-D model and alpha increasing only data are shown for the flat plate model which exhibited less hysteresis effects. Fuselage camber effects are evident near 0° and slopes of C_N and C_m are similar up to about 10° . Beyond 10° , it appears that vortex lift is being generated by the flat plate nose acting as a strake. This is indicated by a pitch up

trend in C_m that breaks at about 20° which is probably due to burst of the flat plate nose vortex. After that point, C_m trends track each other with an approximately constant displacement most likely due to the added lift on the flat plate nose. At about 40° , the 3-D model flow fields break down and drive C_m toward the trend shown by the flat plate model after which both track each other with a slight nose up offset for the 3-D model. The offset in C_m is similar to that for C_N which indicates that the center of pressure is about the same for both models above about 50° . It is probable that after the wing completely stalls, the flat plate "nozzle area" picks up normal force which tends to balance the flat plate nose. The normal force of these two projected areas is most likely responsible for the additional C_N increment for the flat plate model above 40° .

Dynamic results for two frequencies, $k = 0.0333$ and 0.0882 are shown in Figs. 6-32 and 6-33. The incidence range of 8° to 56° starts in incipient vortex flow, passes through vortex burst and static C_{Nmax} , and peaks in stalled wing flow. With exception of some difference due to static characteristics, the dynamic C_N loops in Figs. 6-32 and 6-33 are very similar. In this case, both C_N vs α plots were made by shifting the flat plate plots so that the static curves coincided up to about 25° . The higher level of C_N for the flat plate model on pitch-down at low frequency in Fig. 6-32 is directly related to the higher static level above 50° for that model. The same is not entirely true for the higher frequency in Fig. 6-33. In fact a noticeable difference near the minimum incidence shows an apparent lag tendency for the 3-D model as compared with the flat plate model. Other than that the high frequency loops are very similar.

The pitching moment loops in Figs. 6-32 and 6-33 are quite different, however, and tend to be less open for the flat plate model. The difference is again tied to the static characteristics shown in Fig. 6-31 where the pitch-up transition around 35° to 45° is much more pronounced for the 3-D model. The influence of this "glitch" is evident at the lower frequency in Fig. 6-32 for the 3-D model where the dynamic loop appears to be a simple static hysteresis loop with additional lag. (This is indeed the case.) At the higher frequency in Fig. 6-33, the 3-D C_m loop is further extended in a similar manner. The C_m loop for the flat plate model at lower frequency is similar to that for the 3-D model but thinner as predicted by a less severe "glitch" in C_m near 40° for the flat plate model. At high frequency, the C_m loop is larger in the 10° to 20° range for the flat plate model which is related to the flow transition indicated by a break in the static C_m curve at about 20° . This break was attributed to bursting of the vortex that is apparently generated by the flat plate nose as discussed above.

In summary, the use of flat plate models to dynamically represent scaled 3-D configurations has been shown to be

effective in generating representative C_N loops related to the static characteristics. For this configuration the C_m loops were not well correlated, however, the differences were shown to be directly related to differences in the static C_m curves. Thus, it has been further demonstrated that the dynamic characteristics are fairly insensitive to the usual aerodynamic parameters in a direct sense but are influenced indirectly through the static characteristics.

6.5 PLANFORM EFFECTS

One of the main objectives of this investigation was to determine the effect of varying planform geometric parameters on dynamic force characteristics. The approach taken was to develop trends from both ADF and HFF dynamic tests and verify these trends by showing how well the two test techniques agree with each other. Thus, trends shown by ADF test results should correlate with those shown by HFF results otherwise both could be suspect. This was not always a straight forward judgement and in some cases definite conclusions could not be drawn.

The development of trends was based on a systematic comparison of the data sets already discussed in this report. The effect of leading edge sweep was shown with the 55° and 70° delta wings. The effect of planform type for low aspect ratio highly swept wings was shown with the 70° delta and the $70^\circ/30^\circ$ cranked wing. The effect of planform type for higher aspect ratio lower swept wings was determined with the straked wing and 55° delta. The first two effects were examined at both frequencies where as the latter was examined only at the higher frequency.

Comparison of 55° and 70° delta wing C_N loops are shown in Fig. 6-34 for the ADF tests. The incidence range is from 8° to 56° for both models at the low and high frequencies. At low frequency the 70° delta is more dynamic during pitch-up but less on pitch-down. At the high frequency, both wings look very similar on pitch-up where as the 55° delta is again more dynamic on pitch down. It will be noticed, however, that the static C_{Nmax} point occurs about 8° earlier on the 55° delta, thus the relationship of the model motion with major flow field transition points was not the same for both wings.

A second comparison for the 55° and 70° delta wing C_N loops is shown in Fig. 6-35 for the ADF test. In this case, the 70° delta wing pitch/pulse starts at 16° and goes to about 64° . The 55° delta data are the same as shown in Fig. 6-34 but are shifted in both angle and C_N so as to maintain a common starting point for the dynamic loops. As can be seen, the loops for the two wings have a similar relationship to static C_{Nmax} . At low frequency, the two dynamic loops are very similar but show a

different skewing which tends to track the static curves after static C_{Nmax} . At high frequency, the C_N loops again look very similar but are skewed in the same way as the loops were at the lower frequency. This second comparison was felt to be more indicative of planform effects on dynamic normal force characteristics since it was possible to better separate out the static trends.

A similar comparison for the two delta wings with HFF results is shown in Fig. 6-36 using the same conditions as those in Fig. 6-35. In this case, C_{Nmax} was not as well matched due to Reynolds number effects on the 55° delta. The low frequency C_N loops are similar in shape but wider for the 70° delta. This is a result of the larger drop in static C_N after C_{Nmax} as compared with the 55° delta. At high frequency, the loops are very similar but the 70° delta loop is again wider. Skewing of the loops with static characteristics is present but is not as pronounced as in the case of the ADF results in Fig. 6-35.

When related back to differences in the static characteristics, the two delta wings show very similar dynamic C_N loops for both sets of test data. Thus within the leading edge sweep range of 55° to 70° , the effect of sweep seems to be minimal for the dynamic forces.

The effect of planform type for low aspect ratio highly swept wings is shown in Fig. 6-37 for the ADF tests of the 70° delta and $70^\circ/30^\circ$ cranked wing models. The aspect ratios were 1.455 and 1.715 respectively. Two frequencies were tested and the amplitude shown is for 8° to 54° . Because the static curves were so close for these two wings no shifting was necessary. The C_N loops at both frequencies are very similar as expected due to dominance of the 70° swept inboard portion of the cranked wing. The loops are identical at low frequency and slightly larger for the cranked wing at the higher frequency.

HFF results for the 70° delta and $70^\circ/30^\circ$ cranked wings are shown in Fig. 6-38 for the same two frequencies but a higher incidence range of 16° to 64° . Because of balance/support interference, C_{Nmax} occurred at a higher angle for these models in the water tunnel; hence the incidence range was shifted so as to better match with the location of C_{Nmax} . A slight downward ($-C_N$) shift of the cranked wing results was also required in order to match starting points on the dynamic C_N loops. The low frequency loops are very similar in comparison to those for the ADF tests in Fig. 6-37 with the exception that dynamic C_{Nmax} is less for the cranked wing than the delta wing in Fig. 6-38. The trends at high frequency in Fig. 6-38 do not look reasonable, however, where the cranked wing data show a significantly smaller loop in comparison to the 70° delta wing results. This is opposite in trend to what was seen in Fig. 6-37. Since the static C_N curves are so close for the two wings in the water

tunnel, it would be expected that their associated dynamic loops would also be similar. Hence, it is felt that the cranked wing dynamic data at the higher frequency may not be representative.

In accordance with the result found for the effect of wing sweep, the 70° delta and $70^\circ/30^\circ$ cranked wing showed essentially the same dynamic characteristics with exception of the one noted discrepancy. Thus, the effect of cranking the outboard tip to 30° seems to have minimum influence on the dynamic forces.

The effect of planform type for higher aspect ratio wings with lower sweep is shown in Fig. 6-39 for both the ADF and HFF results at the higher frequency. In this case, the straked wing and 55° delta results are compared where the aspect ratio is 2.44 and 2.81 respectively. In neither the ADF nor HFF data sets is any similarity seen in the dynamic C_N loops. The static C_N curves, however do agree quite well in both cases. It has been observed that the straked wing acts like a planform whose reference length for dynamic similarity is much shorter than the root chord. Thus, the dynamic loops for this wing appear to be less dynamic than say the delta wings for the same amplitude of motion and reduced frequency.

It is not known what the correct dynamic reference length for the straked wing should be, but a comparison with the lower frequency 55° results in Fig. 6-40 indicates that it is much less than the root chord. The ADF results in Fig. 6-40 are almost identical with exception of a higher dynamic C_{Nmax} overshoot. If the theoretical root chord of the straked wing is used, would be reduced to 0.0165 which is close to 0.0114 for the 55° delta wing. The HFF results do not match as well but there is a significant improvement. However, this last comparison is clouded by the high levels of oscillatory noise present in the water tunnel data.

Judging by the ADF results in Fig. 6-40 it appears that again there is little influence of planform type for higher aspect ratio wings on the dynamic normal force development. This seems to be especially true if the static characteristics are very similar.

In summary, relative to the static C_N curves, minimum effects were observed on dynamic normal force development for (1) wing sweep (55° to 70°) on delta wings, (2) planform shape (70° delta vs $70^\circ/30^\circ$ cranked) for low aspect ratio and high sweep, and (3) planform shape (straked vs 55° delta) for higher aspect ratio and lower sweep. All trends seemed to be clearly visible with exception of two cases for HFF data at the higher frequency.

7.0 CONCLUSIONS

The force testing of small-scale models in a small wind tunnel and a water tunnel was investigated as an inexpensive and quick means to obtain meaningful dynamic force and moment data representative of rapidly maneuvering full-scale aircraft. Force tests of flat-plate semi-span models were conducted in the General Dynamics Aerodynamic Development Facility (ADF) which is a small 14x14 in² low speed wind tunnel. Oscillatory model motions up to 48° (peak to peak) amplitude were tested at frequencies of 1 to 3 Hz. Force tests of flat and three-dimensional full span models were conducted in the General Dynamics Hydroflow Facility (HFF) which is a horizontal flow water tunnel with a 24x24 in² test section. Pitch/pulse model motions were tested for conditions similar to those tested in the ADF. The test velocities were 100 fps in the ADF and 0.8 fps in the HFF which yielded nominal test Reynolds numbers of 0.6×10^6 and 0.06×10^6 respectively (based on root chord). Frequencies of motion in the HFF were scaled with velocity to maintain constant non-dimensional frequencies and pitch rates. Thus, frequencies for the HFF tests were nominally 0.01 and 0.03 Hz.

Specific objectives of this investigation were: (1) verify static and dynamic force and moment measurements from the small scale tests with results from reliable or multiple sources; (2) determine time history effects for various frequencies, amplitudes, starting angles and peak angles; (3) evaluate the effects of test medium; (4) determine Reynolds number effects; (5) demonstrate the importance of model three-dimensionality; and (6) evaluate the effects of planform geometry variations. Results for each of these objectives are summarized below.

The static correlation of ADF wind tunnel and HFF water tunnel force and moment results with other reliable sources of data has shown that both test techniques give reasonable results. In general full-span testing in the HFF provides very good force and moment data that may be slightly low, particularly near C_{Nmax} , as a result of Reynolds Number effects. Semi-span testing in the ADF provides better normal force data because of a higher Reynolds number capability, but pitching moment data which are off as a result of centers of pressure that are too far aft.

Good agreement has been demonstrated between dynamic normal force results obtained with the small scale models and the NLR model. Correlations were made at the higher frequency of the small scale tests at various incidence ranges and amplitudes based on matching the starting point static conditions. In general, the HFF results tended to agree better with the NLR data than did the ADF results at the lower incidence ranges. At the higher range where the model motion was confined to highly separated flows, good agreement was achieved between all three

results without shifting to match the starting point static conditions. This change in characteristic was attributed to the change in the relationship between kinematic and viscous forces for dynamic model motion.

The correlations of dynamic pitching moments from the ADF and HFF tests with large scale data from the NLR test have shown that reasonable trends are obtainable with small scale testing. The correlation of centers of pressure for unsteady forces was better than the correlation of C_m results. Similar to observations made for normal force, it was also seen that the moment correlations were further improved in the separated flow regime where kinematic forces dominated over viscous forces for dynamic model motions.

Time history effects were presented which showed that their influence is of major importance in the development of dynamic forces and moments on moving models that represent rapidly maneuvering aircraft. Repeatability was shown to be better for the ADF oscillatory data as compared with the HFF pitch/pulse results. For correlation purposes, it was also found that pitch/pulse and oscillatory model motions gave essentially the same results with the exception that dynamic C_{Nmax} was slightly higher for the latter type motion. Frequency effects at constant amplitude motion were shown to be consistent for both ADF and HFF results with a trend to expanding the C_N dynamic loops with increasing frequency for all models tested. The effect of starting and peak angles was demonstrated to be highly non-linear as a result of varying lag characteristics which were determined by the flow field types encountered by the model during its motion time history. As a result, it is possible to simulate pitch-up dynamic C_N overshoot characteristics of large amplitude motions with smaller amplitude runs but of similar values. The dynamic C_N undershoot on pitch-down, however, cannot be fully simulated in this way for large amplitude motions that significantly exceed the point of static C_{Nmax} . This is due to the non-linear nature of the time history effects in highly chaotic turbulent flows that exist over a highly stalled wing.

The effects of test medium, high-speed air vs low-speed water, do not seem to have any influence on static force data for the models tested other than Reynolds number effects. This is not true for dynamic testing where significant force and moment oscillations not seen in air were observed in the water tunnel dynamic data at frequencies as low as 0.01 Hz, even for zero water velocity. As a result, pitch rate limitations were imposed on the test conditions and low pass filtering was applied during data processing to remove the oscillations. Because of high frequencies required by testing in air at high speeds, frequency limitations were also encountered due to the high dynamic inertia loads on the driving stepper motor. Low pass filtering was used in the ADF data processing to eliminate forces and moments

resulting from structural dynamic effects. The correlation of dynamic C_N loops for the four basic models showed that the two test approaches agreed very well where static characteristics were closely matched. Where static data did not correlate, the displacements in dynamic data tended to track corresponding displacements in the static data.

Reynolds number effects were observed mostly in the steady data where as the differences in dynamic results could be traced back to differences in the steady characteristics. The effects of lower Reynolds numbers were shown to decrease normal force on models at incidences where the flow is dominated by burst vortex type flow fields. Less sensitivity was seen for more highly swept wings of lower aspect ratio. The effects of lower Reynolds number on pitching moment were shown to move the center of pressure forward at all flow conditions, however, the magnitude of change was not significant and amounted to only about 1% of the root chord in the case of the straked wing.

The use of flat plate models to dynamically represent scaled 3-D configurations was shown to be effective in generating representative C_N loops related to the static characteristics. For this configuration the C_m loops were not well correlated, however, the differences were shown to be directly related to differences in the static C_m curves. Thus, it has been further demonstrated that the dynamic characteristics are fairly insensitive to the usual aerodynamic parameters in a direct sense but are influenced indirectly through the static characteristics.

Relative to the static C_N curves, minimum effects were observed on dynamic normal force development for (1) wing sweep (55° to 70°) on delta wings, (2) planform shape (70° delta vs $70^\circ/30^\circ$ cranked) for low aspect ratio and high sweep, and (3) planform shape (straked vs 55° delta) for higher aspect ratio and lower sweep. All trends seemed to be clearly visible with exception of two cases for HFF data at the higher frequency.

In general it has been demonstrated that the small scale wind and water tunnel test techniques do provide reasonable dynamic force and moment data for a wide variety of planforms and conditions. Upper limits on dynamic test frequencies, however, were encountered in both approaches due to structural dynamic effects in the case of small wind tunnel and vortex shedding effects in the water tunnel.

REFERENCES

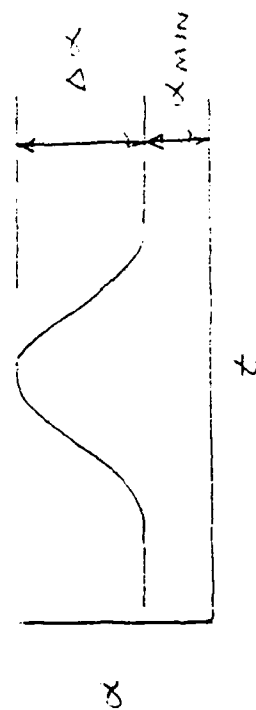
1. Herbst, W. B., "Dynamics of Air Combat", Journal of Aircraft, Vol. 20, July 1983, pp. 594-598.
2. Lang, J. and Francis, M. S., "Unsteady Aerodynamics and Dynamic Aircraft Maneuverability", Paper No. 29, presented at the AGARD Symposium on Unsteady Aerodynamics - Fundamentals and Applications to Aircraft Dynamics, Gottingen, Germany, AGARD CP386, May 6-9, 1985.
3. McAlister, K.W., Pucci, S. L., McCroskey, W. J., and Carr, L. W., An Experimental Study of Dynamic Stall on Advanced Airfoil Sections, Volume 2. Pressure and Force Data, NASA TM 84245, September 1982.
4. Sanctuary, G.E., F-16 Flight Test Aerodynamic Coefficient Extraction Procedures and Results, General Dynamics' Fort Worth Division Report 16PR2405, July 1982.
5. Cunningham, A. M., Jr., Den Boer, R. G., et al, Unsteady Low-Speed Wind Tunnel Test of a Straked Delta Wing, Oscillating in Pitch, AFWAL-TR-87-3098 (Parts I through VI), April 1988.
6. Cunningham, A. M., Jr., Bushlow T., Wilson, T. A. and Mercer, J. R., Water Tunnel Force Testing Experience, General Dynamics' Fort Worth Division Report ERR-FW-2884, December 1988.
7. Wentz, W. H., Jr. and Kohlman, D. L., Wind Tunnel Investigations of Vortex Breakdown on Slender Sharp-Edged Wings, NASA Research Grant NGR-17-002-043, Final Report, November 1968.
8. Chang, R. C. and Muirhead, V. U., "Investigation of Dynamic Ground Effects", NASA CP-2462 (p. 363), August 1985.
9. Hoerner, S. F., Fluid-Dynamic Drag, Hoerner Fluid Dynamics, Brick Town, N. J., 1965.
10. Foley, W. H., Albright, A. E., Powers, D. J. and Smith, C. W., Study of Aerodynamic Technology for Single-Cruise-Engine V/STOL Fighter/Attack Aircraft, Phase II Final Report, NASA CR 177367, August 1985.
11. Soltani, M. R., Bragg, M. B. and Brandon, J. M., "Experimental Measurements on an Oscillating 70-Degree Delta Wing in Subsonic Flow", AIAA Paper 88-2576-CP, 1988.

TABLE 3-1 - SMOKE TUNNEL TEST CONDITIONS

α Min (Deg.)	$\Delta \alpha$ (Deg.)			
	16	32	48	64
8	X	X	X	X
16	X	X	X	X
24	X	X	X	
32	X	X	X	
40	X	X	X	
48	X	X		
56	X			
64	X			

Cut-off for
Straked wing

Frequencies $k = 0.027, 0.078$ (0.025, 0.070 for Straked Wing)



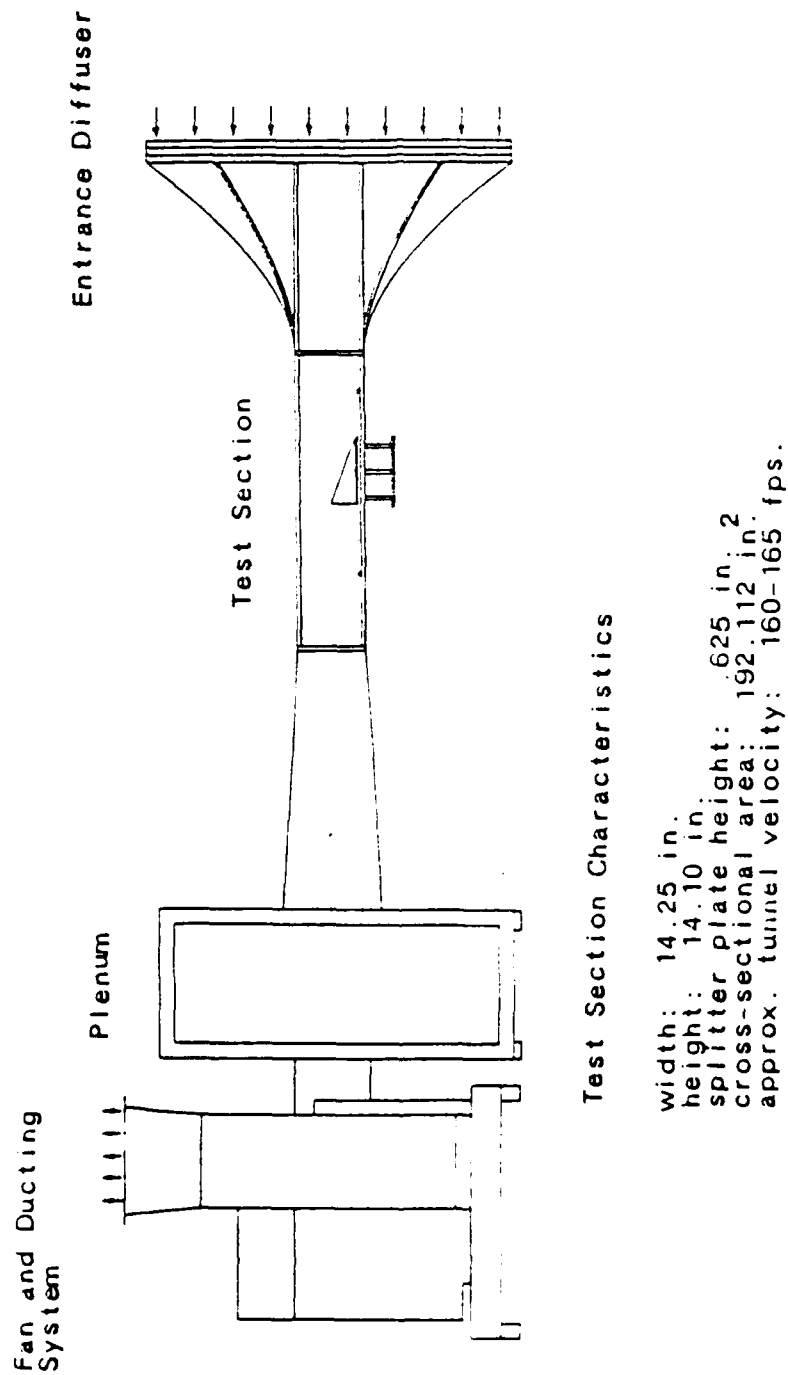
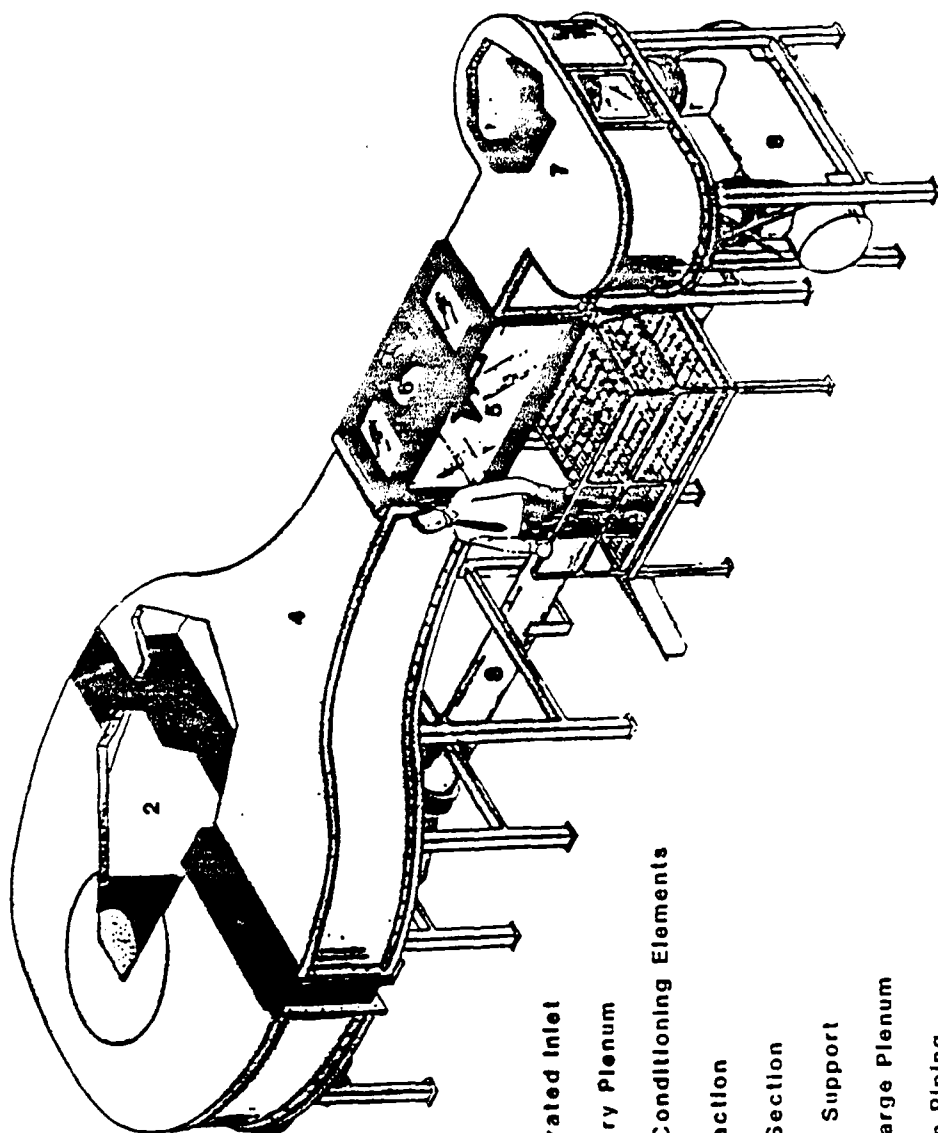


Fig. 3-1 General Dynamics Aerodynamic Development Facility (ADF)



KEY:

1. Perforated Inlet
2. Delivery Plenum
3. Flow Conditioning Elements
4. Contraction
5. Test Section
6. Model Support
7. Discharge Plenum
8. Return Piping

Fig. 3-2 General Dynamics Hydroflow Facility (HFF)

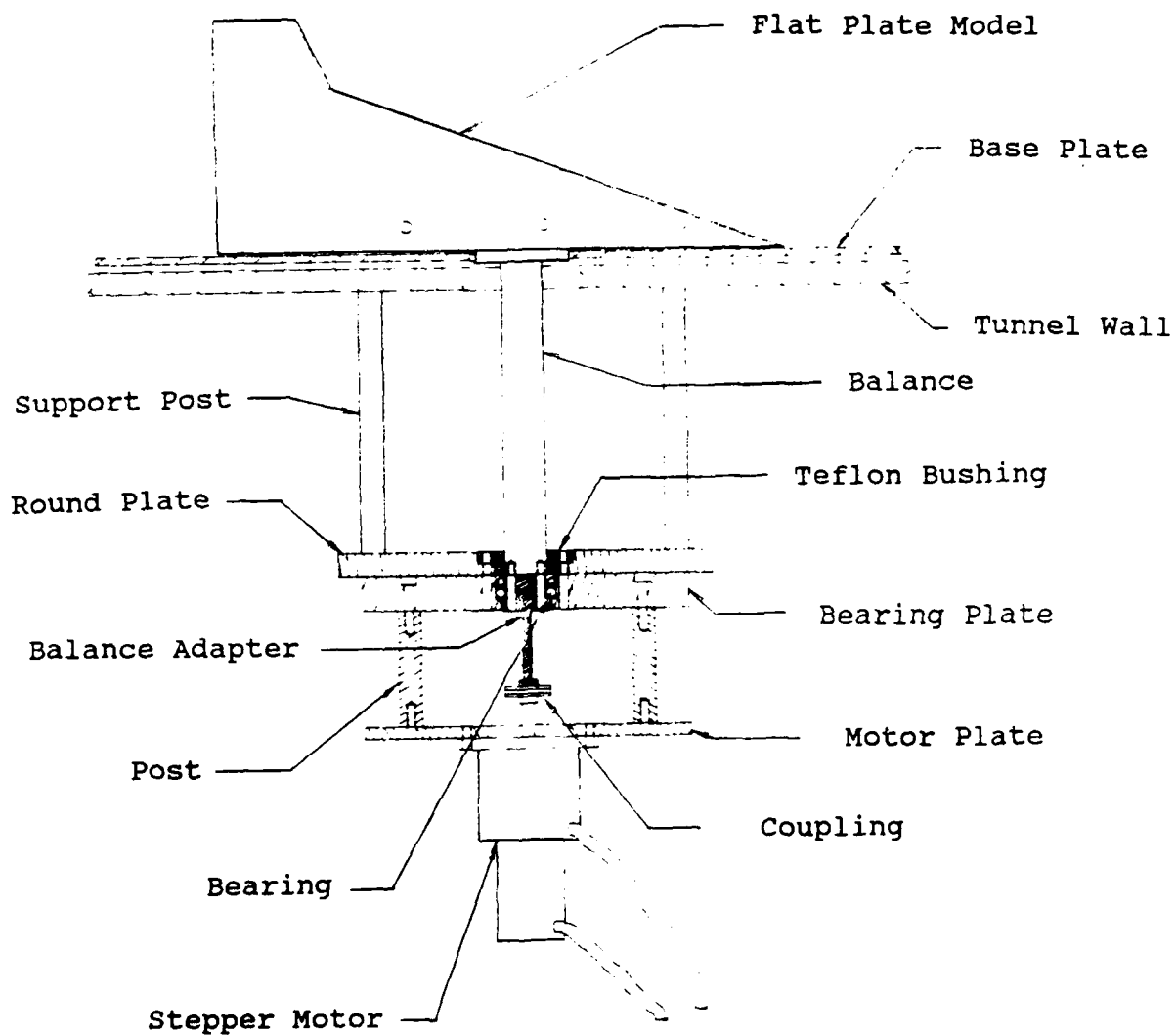


Fig. 3-3 ADF Dynamic Drive and Support System
For Semi-Span Models

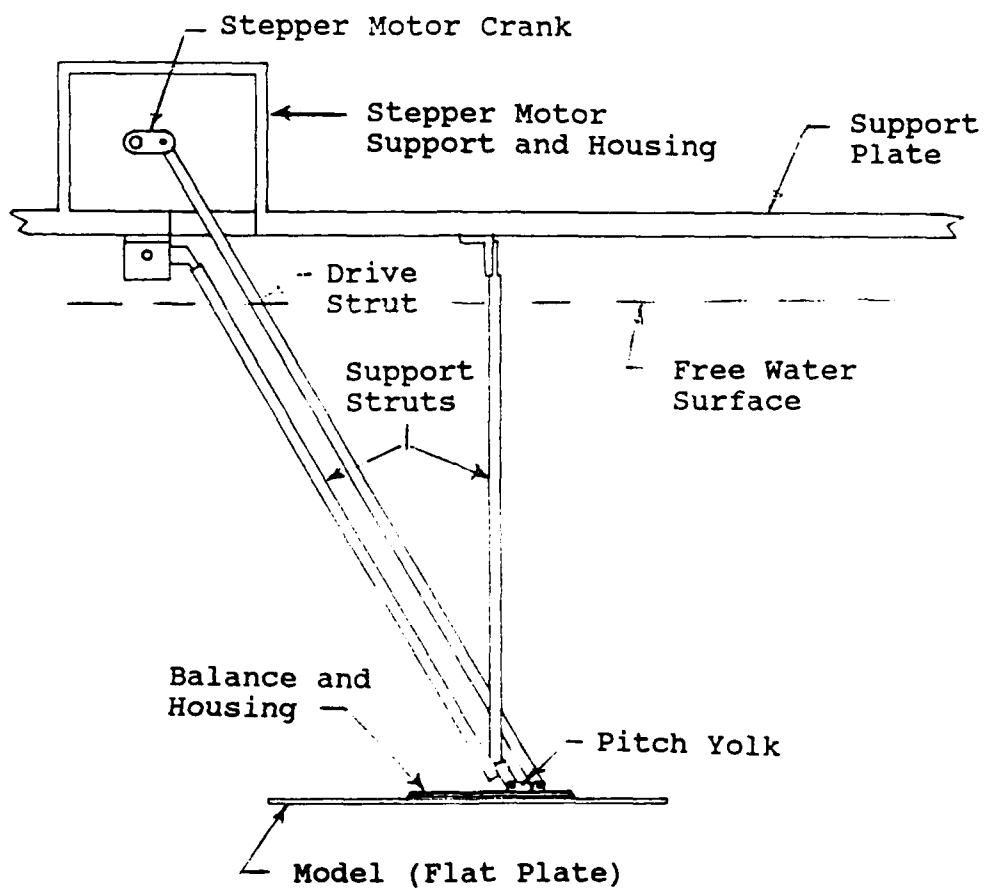
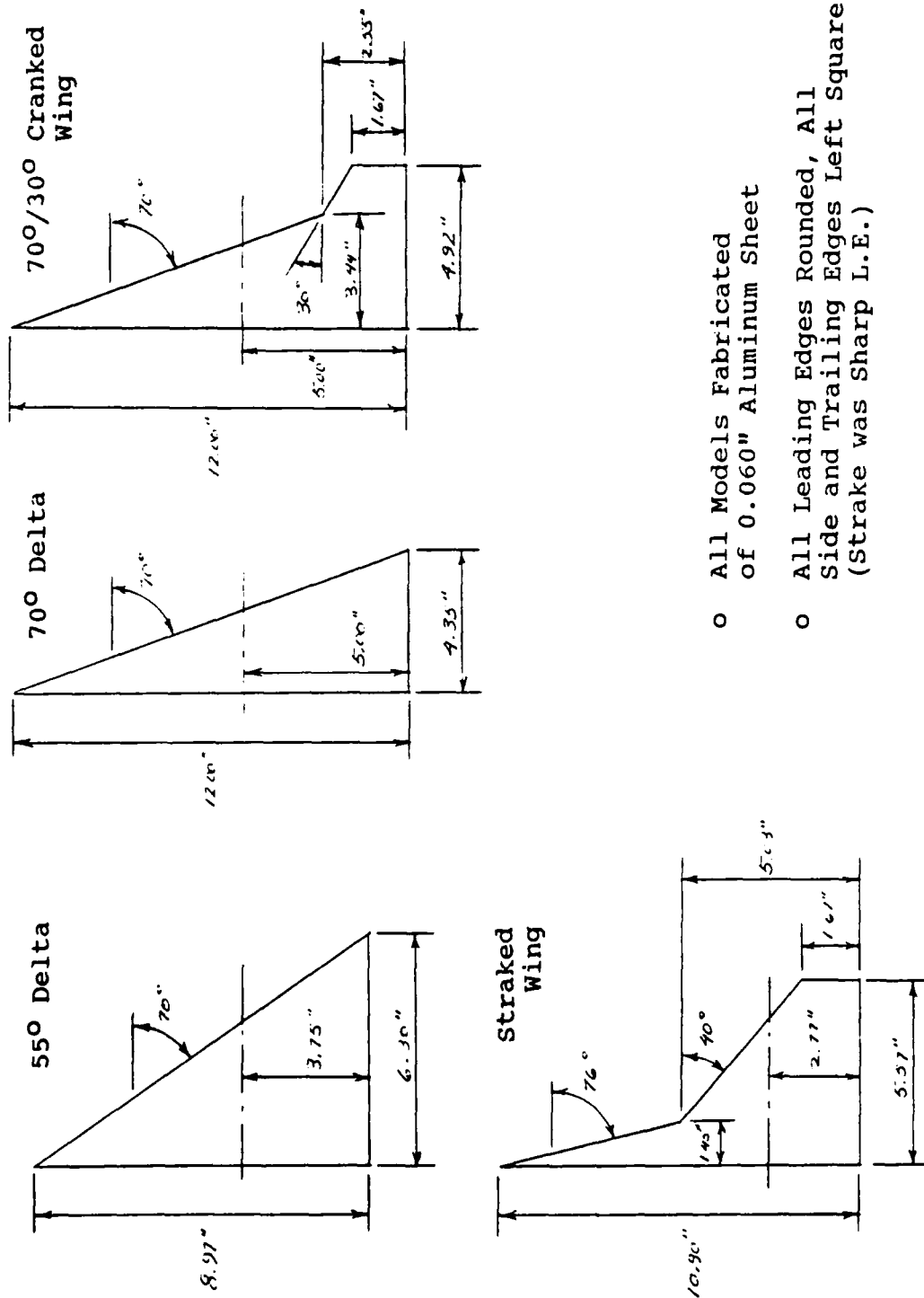


Fig. 3-4 HFF Dynamic Drive and Support System
For Full-Span Models



- o All Models Fabricated of 0.060" Aluminum Sheet
- o All Leading Edges Rounded, All Side and Trailing Edges Left Square (Strake was Sharp L.E.)

Fig. 3-5 ADF Flat Plate Semi-Span Models

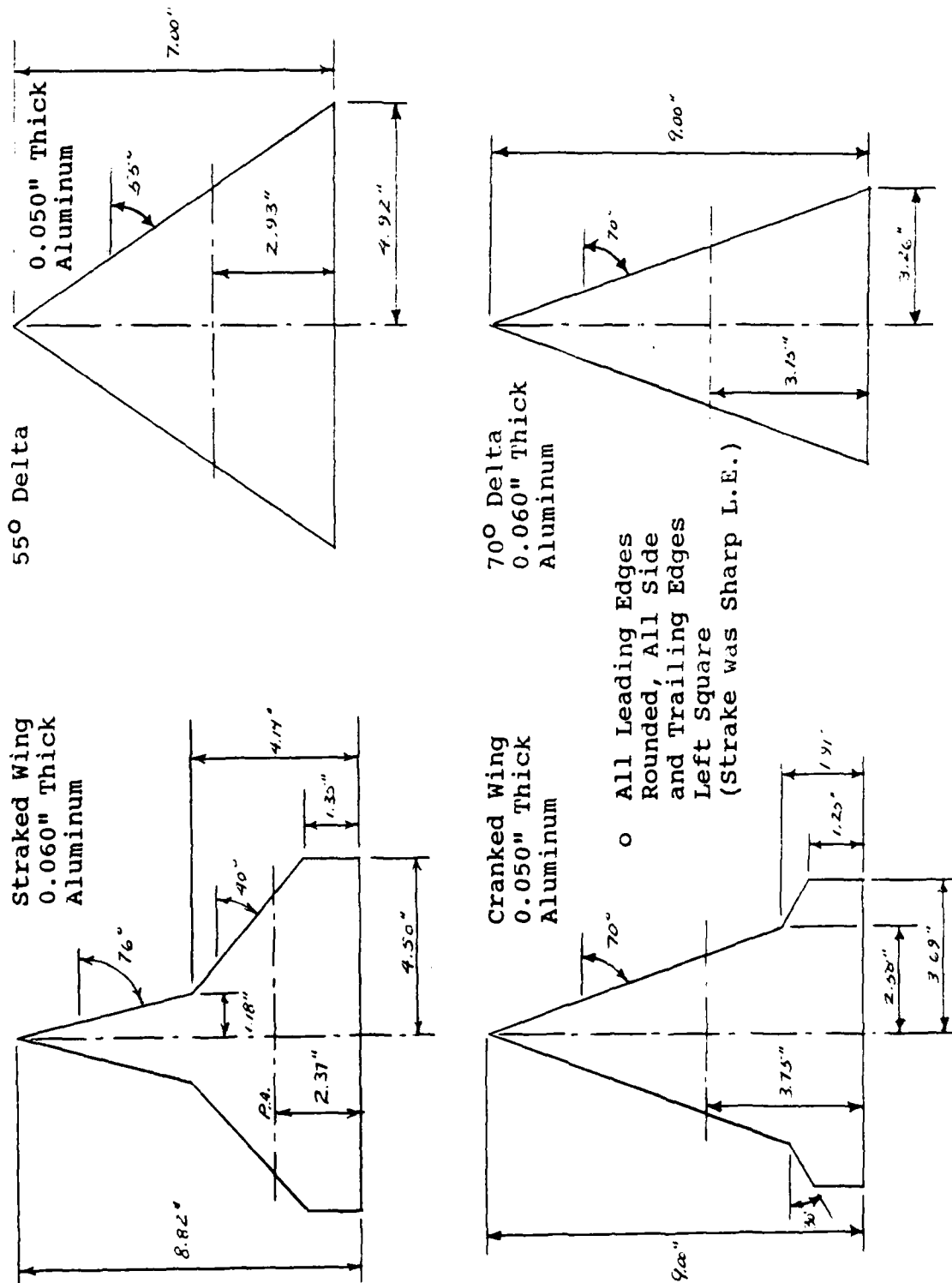


Fig. 3-6 HFF Flat Plate Full Span Models

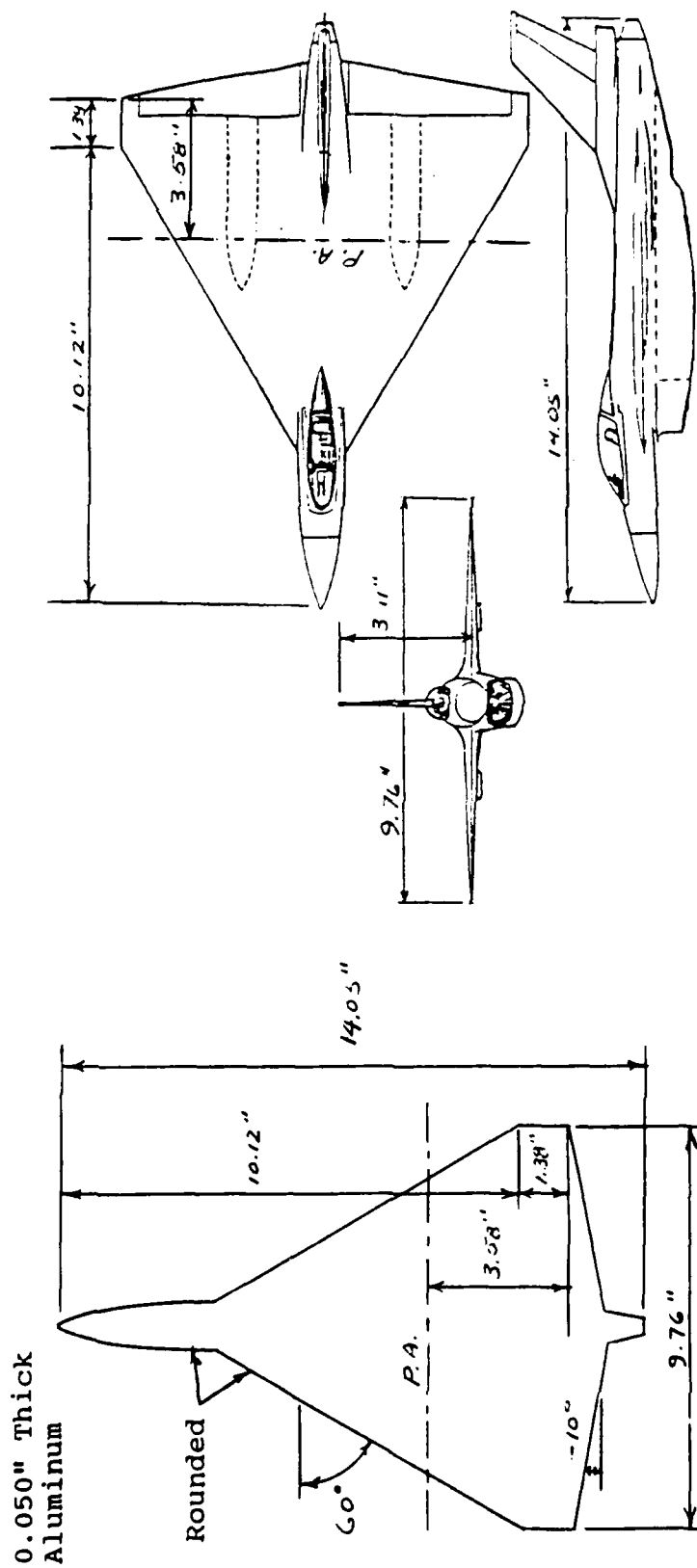


Fig. 3-7 Three Dimensional and Flat E-7 Models for the HFF

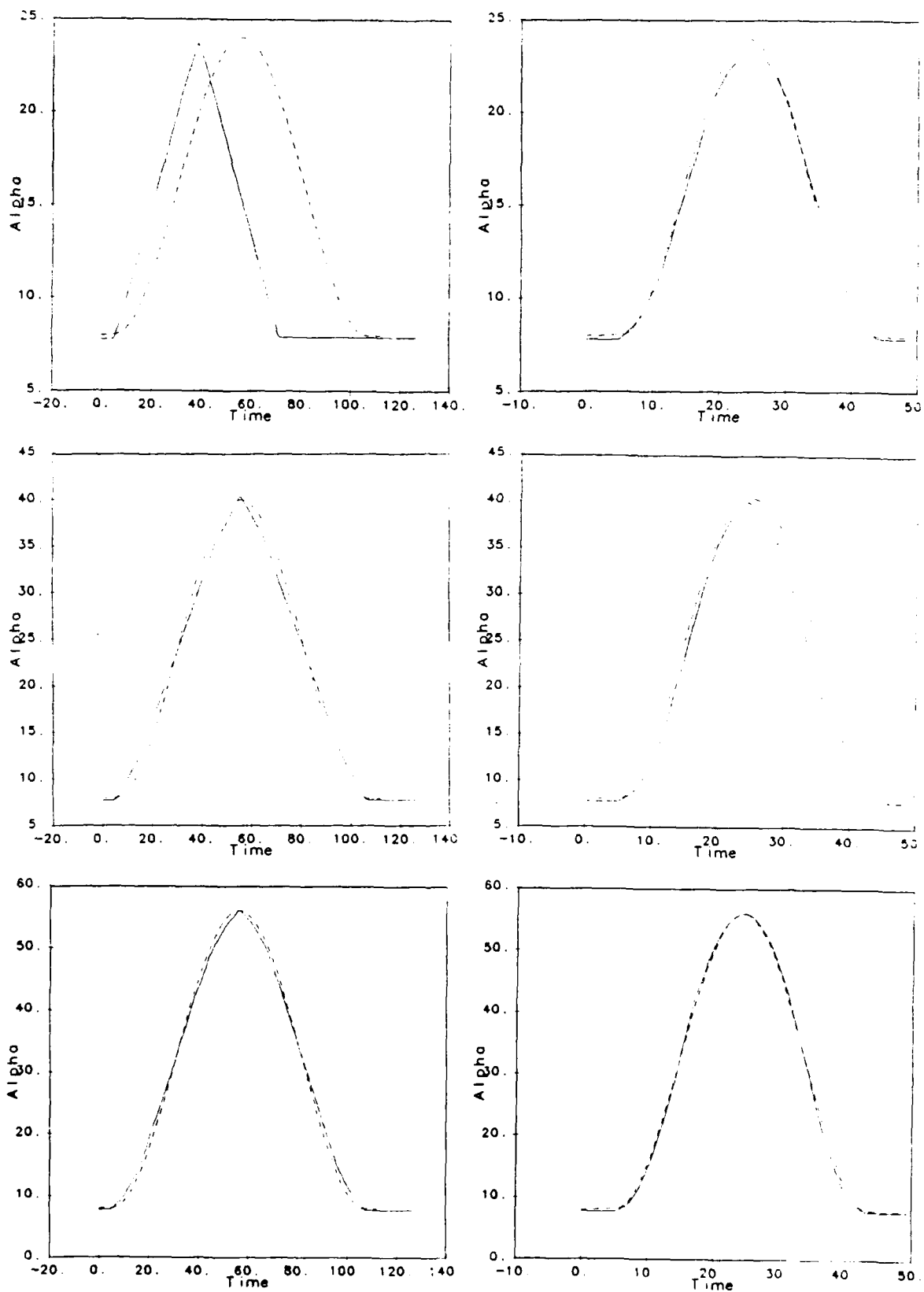


Fig. 3-8 Pitch/Pulse Incidence Time History for Water Tunnel Models at Various Pitch Rates

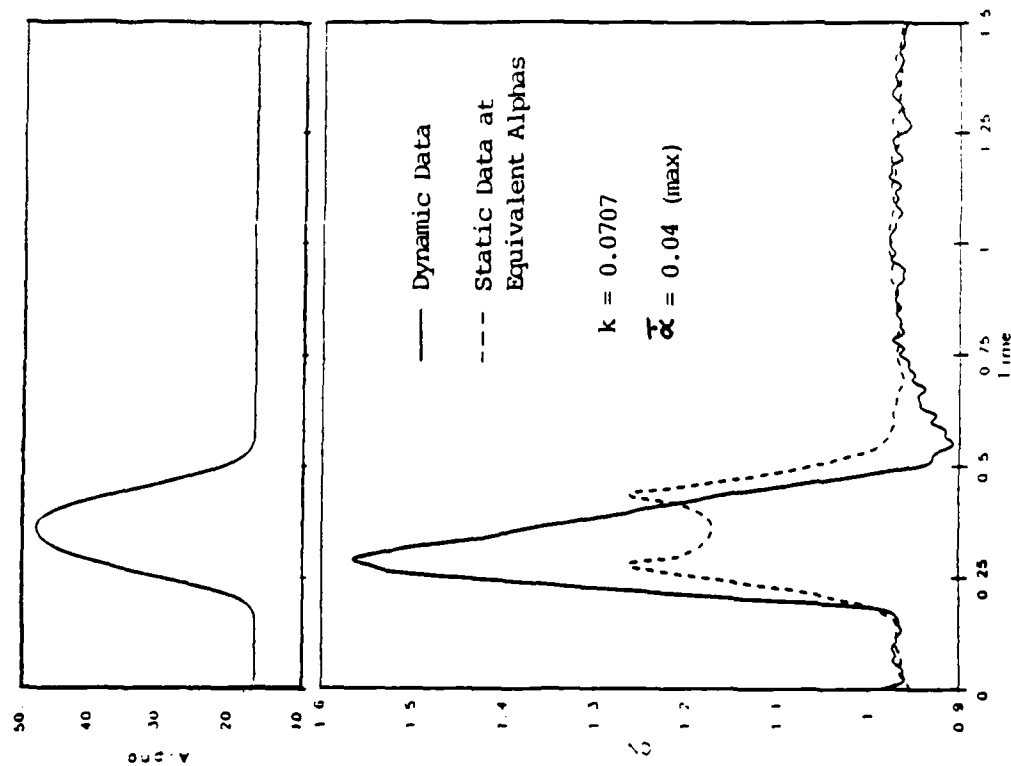


Fig. 4-1 Time History Presentation of a Pitch/Pulse for the Straked wing

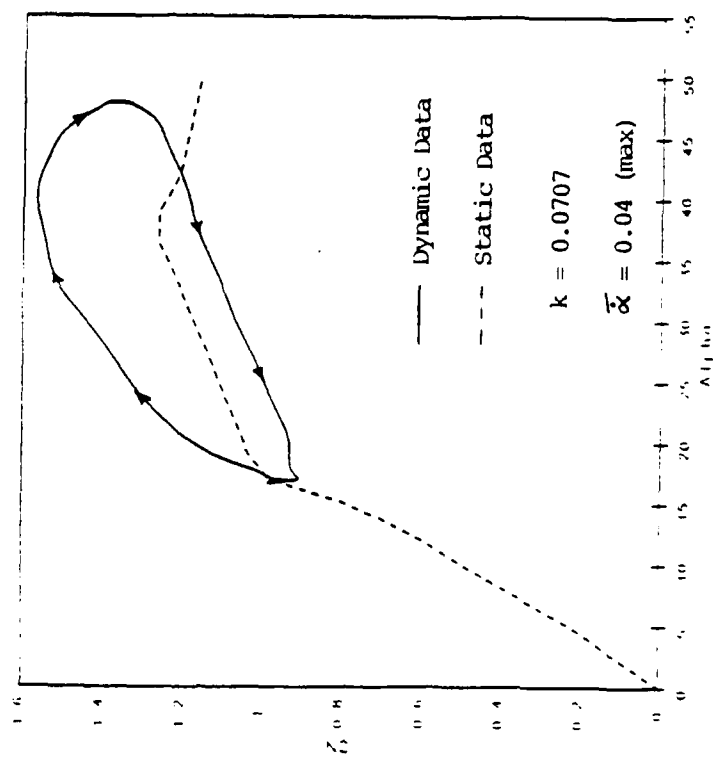
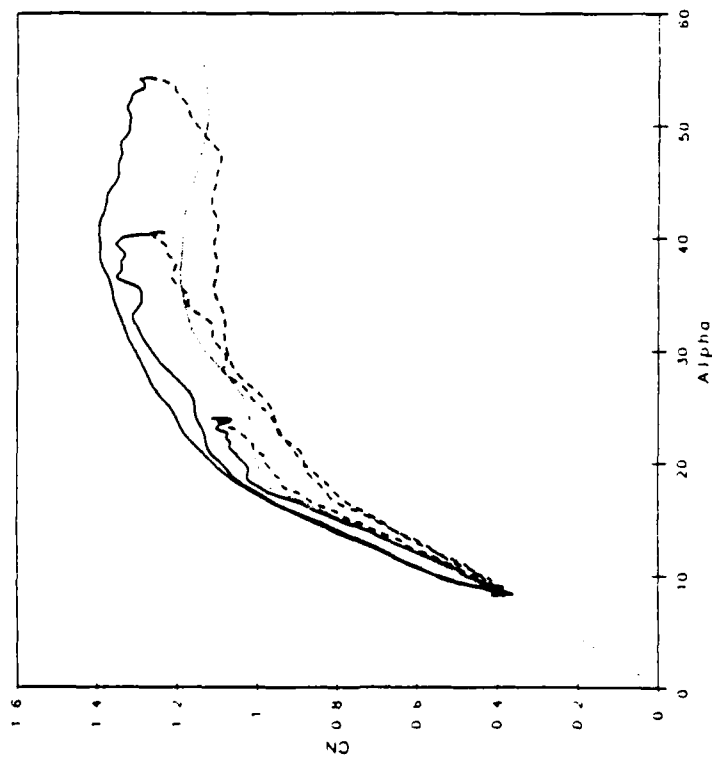
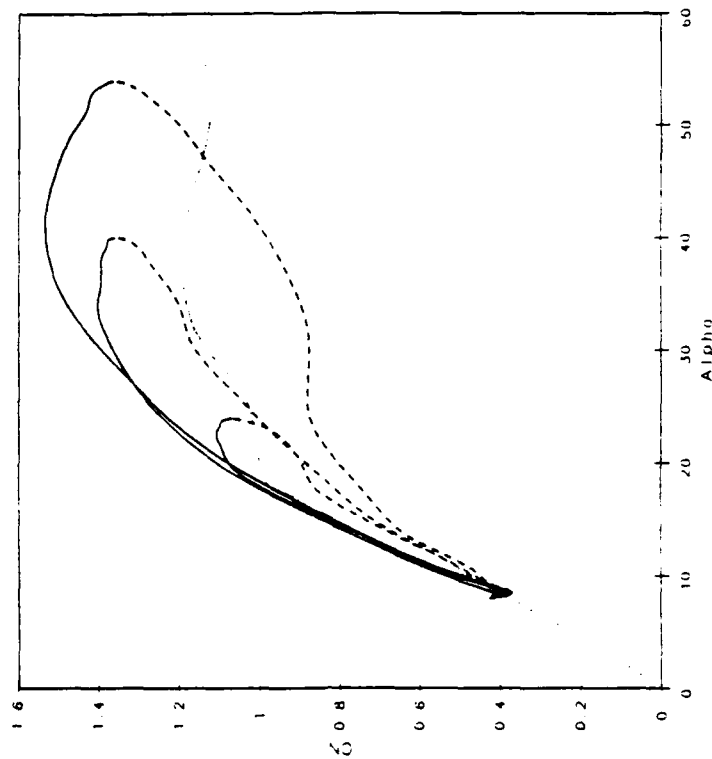


Fig. 4-2 C_N vs α Presentation of a Pitch/Pulse for the Straked Wing

— Positive Pitch Rate
 - - - Negative Pitch Rate
 Static



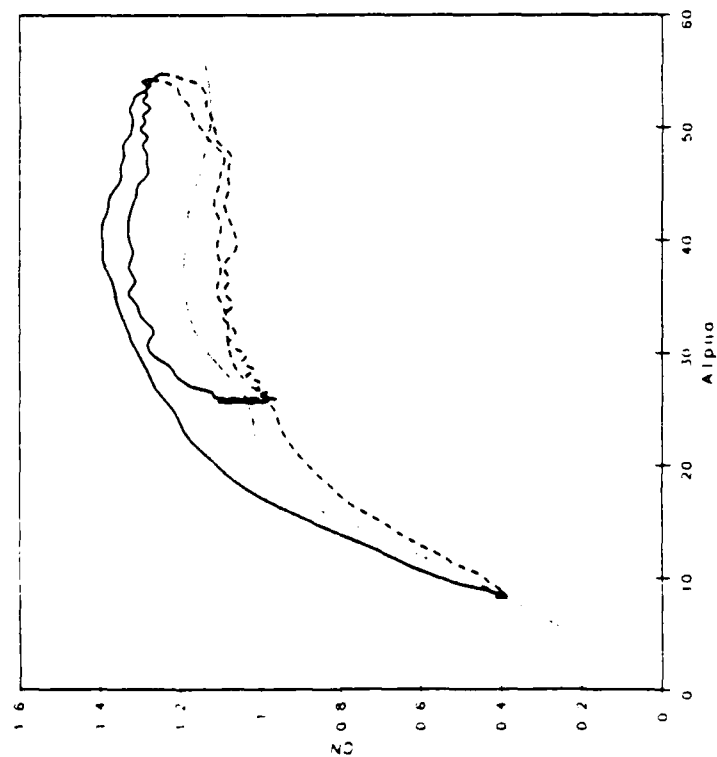
(a.) $k = 0.027$, $f = 0.95$ Hz



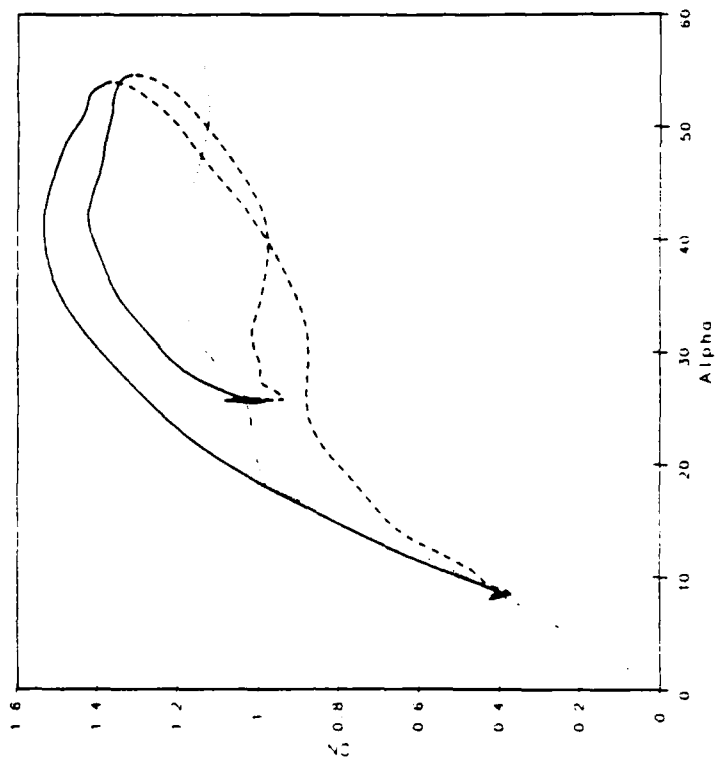
(b.) $k = 0.082$, $f = 2.5$ Hz

Fig. 4-3 Multiple Plot Format for Increasing Peak Angles with a Fixed Starting Angle at Two Frequencies

— Positive Pitch Rate
 - - - Negative Pitch Rate
 Static

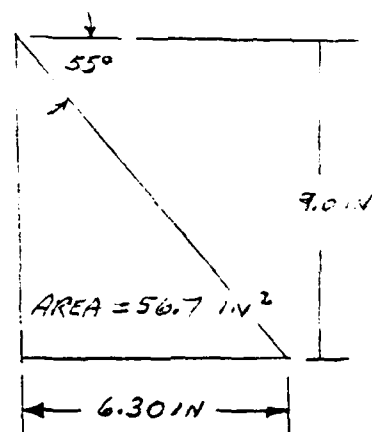
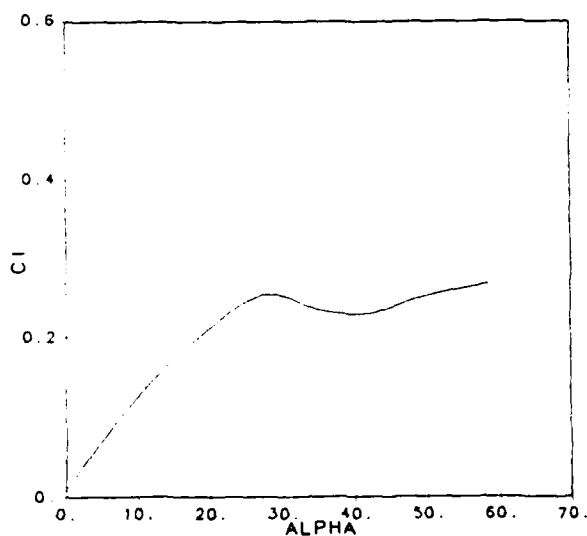
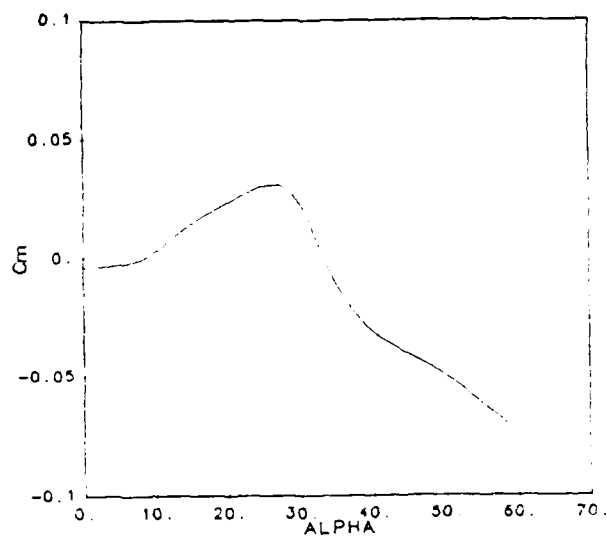
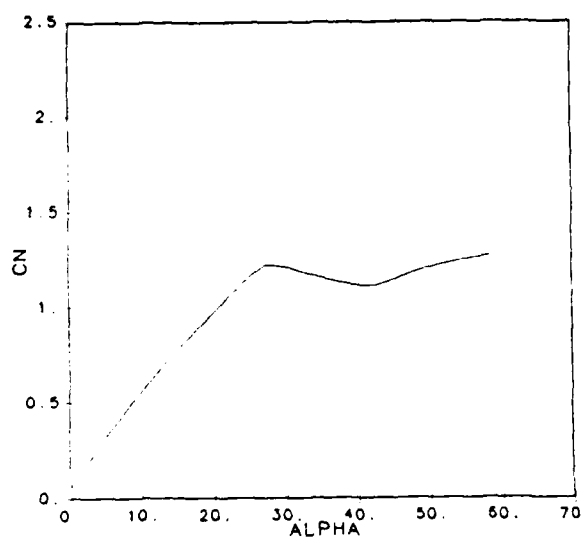


(a.) $k = 0.027$, $f = 0.95$ Hz



(b.) $k = 0.062$, $f = 2.5$ Hz

Fig. 4-4 Multiple Plot Format for Increasing Starting Angle with a Fixed Peak Angle at Two Frequencies



$t = 0.060$ in
 LE = Cylindrical
 TE = Square
 P.A. = 58.33% C_R

Fig. 4-5 Example of the Static Data Format (55° Delta) for Volume II - ADF Wind Tunnel Data Base

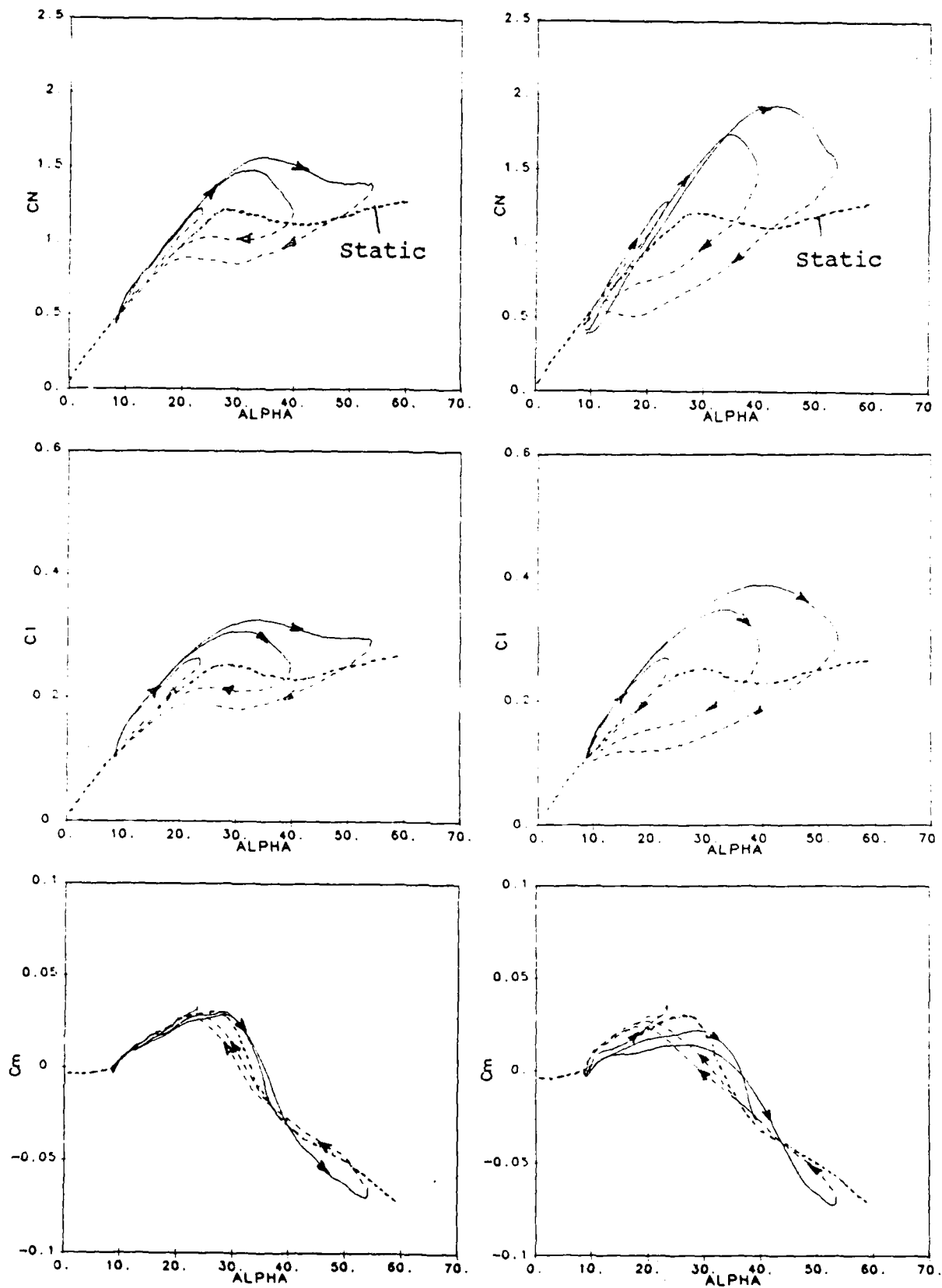
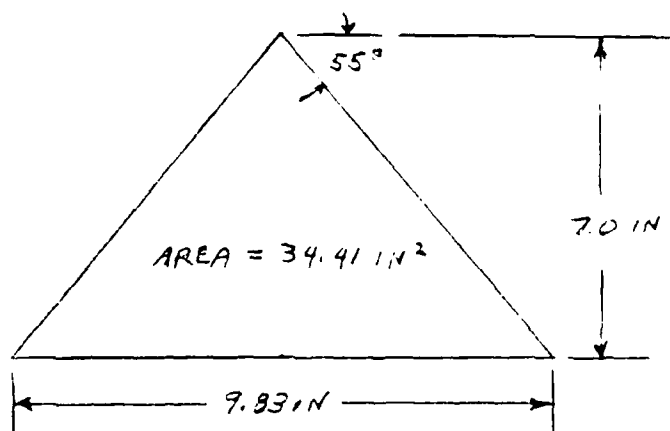
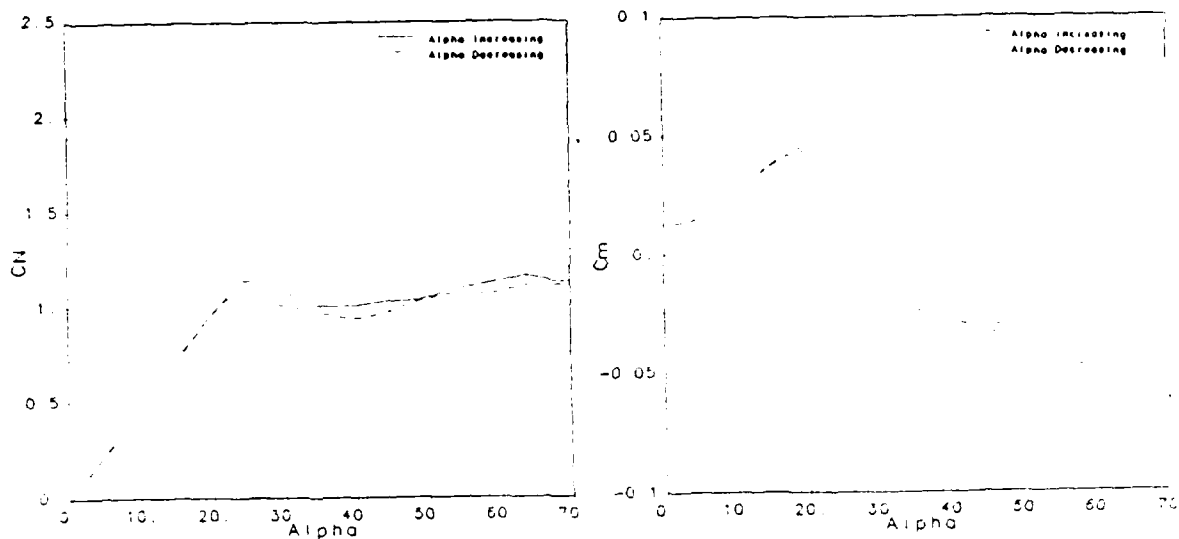


Fig. 4-6 Example of the Dynamic Data Format (55° Delta)
for Volume II - ADF Wind Tunnel Data Base



t = 0.050 in
 LE = Cylindrical
 TE = Square
 P.A. = 57.5% C_R

Fig. 4-7 Example of the Static Data Format (55° Delta)
for Volume II - HFF Water Tunnel Data Base

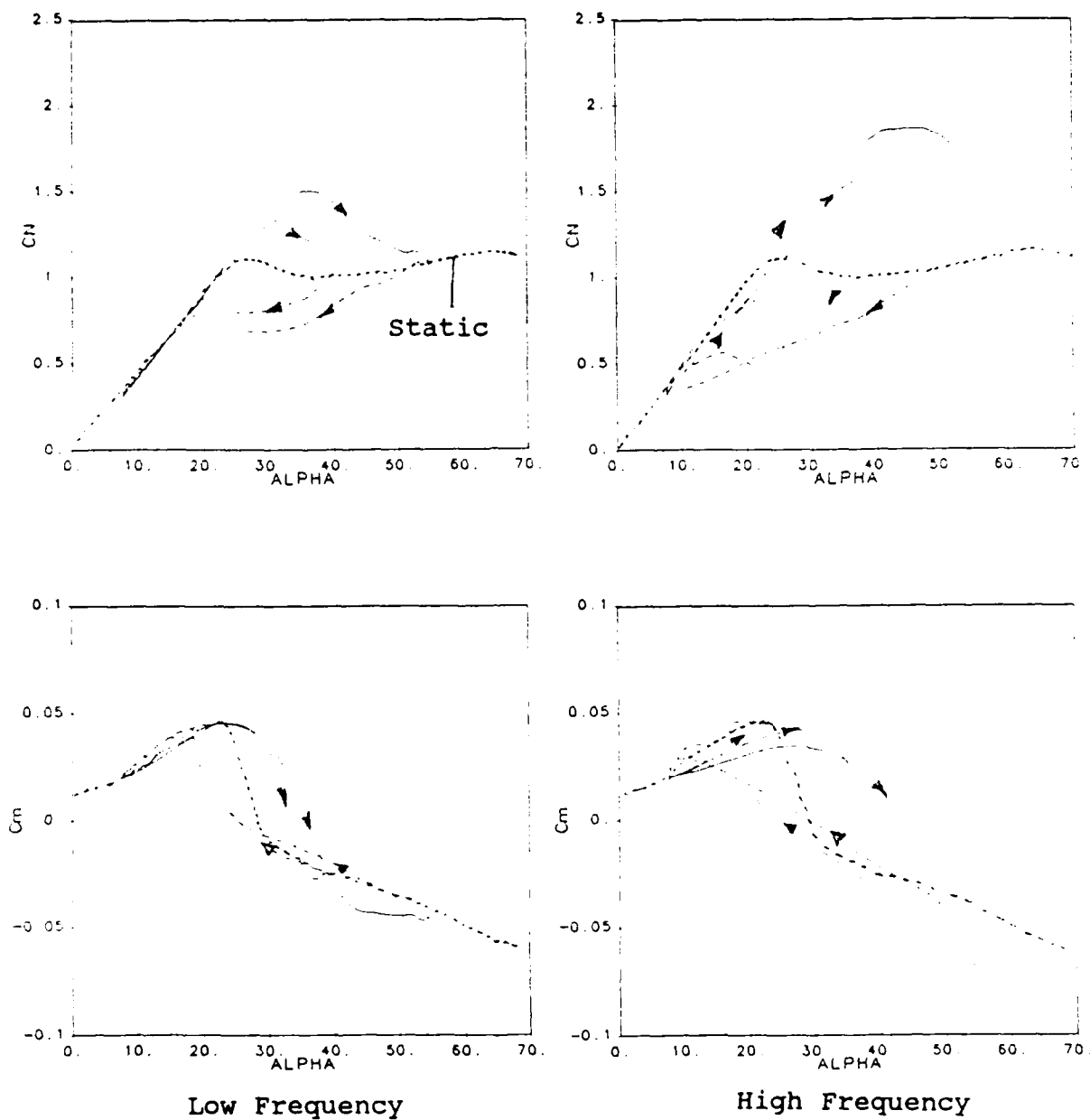


Fig. 4-8 Example of the Dynamic Data Format (55° Delta)
for Volume II - HFF Water Tunnel Data Base

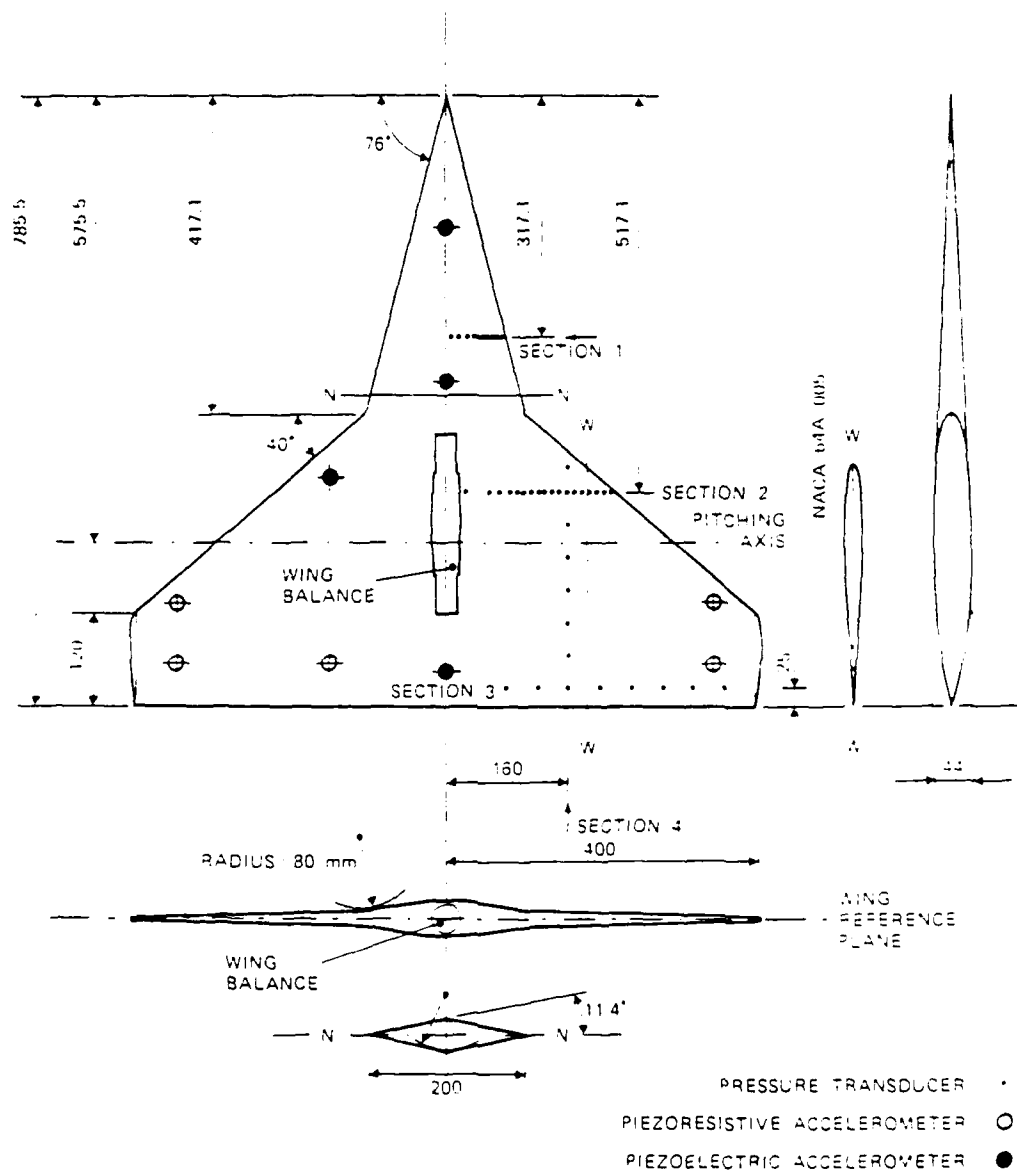


Fig. 5-1 Wing Planform and Instrumentation
for the NLR Straked Wing Model (Ref. 5)

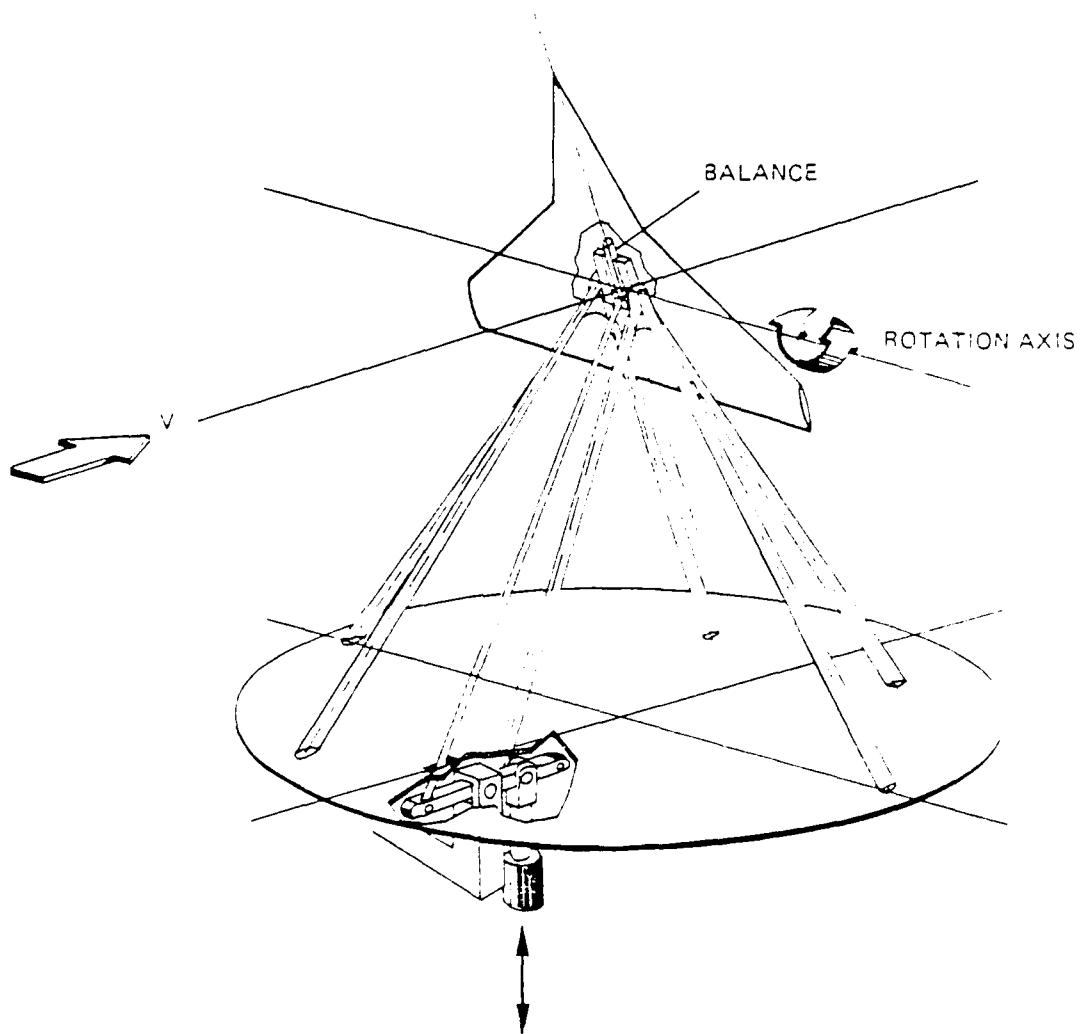


Fig. 5-2 Dynamic Drive and Support System
for the NLR Model (Ref. 5)

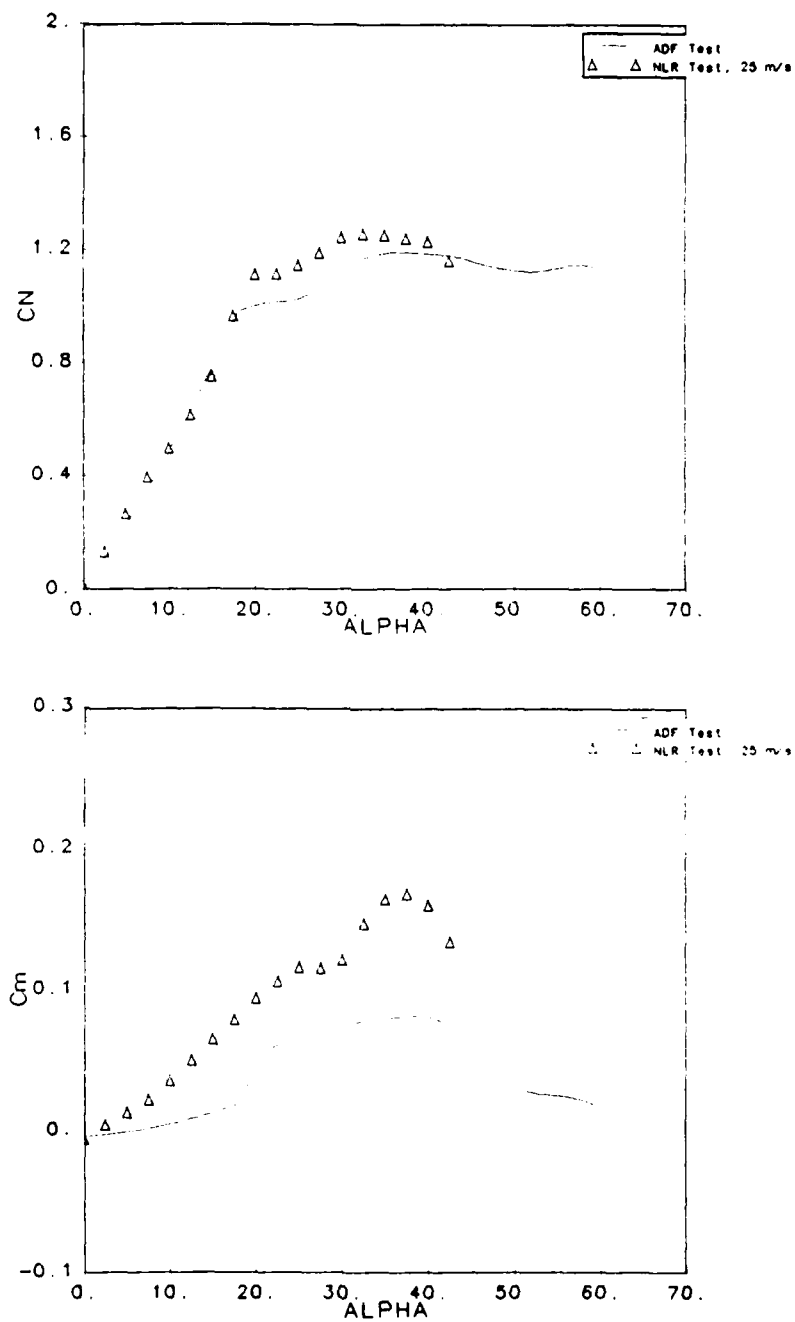


Fig. 5-3 Comparison of Steady Straked Wing Force and Moment Data for the ADF Test ($R_e = 0.55 \times 10^6$) and NLR Test in Wires (Ref. 5, $R_e = 1.4 \times 10^6$)

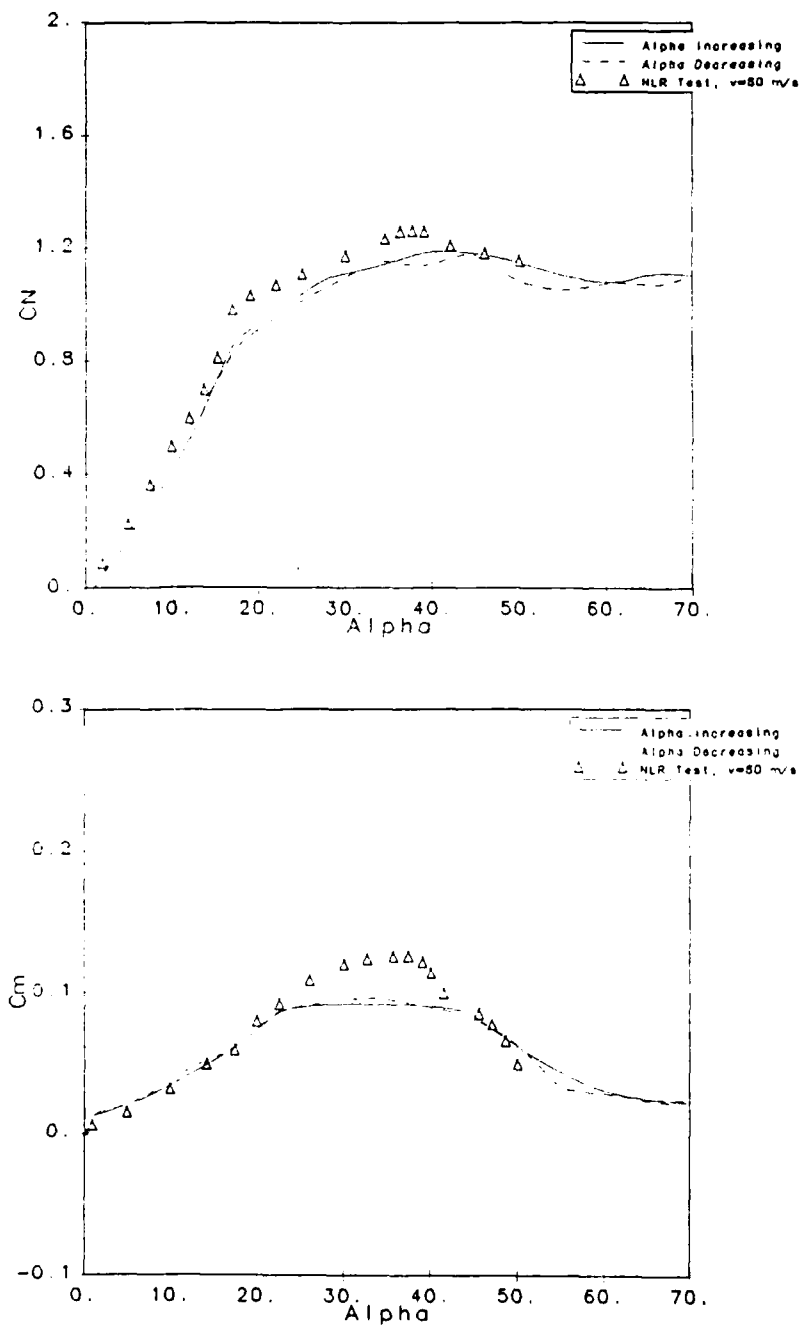


Fig. 5-4 Comparison of Steady Straked Wing Force and Moment Data for the HFF Test ($R_e = 0.06 \times 10^6$) and NLR Test (Ref. 5, $R_e = 4.5 \times 10^6$)

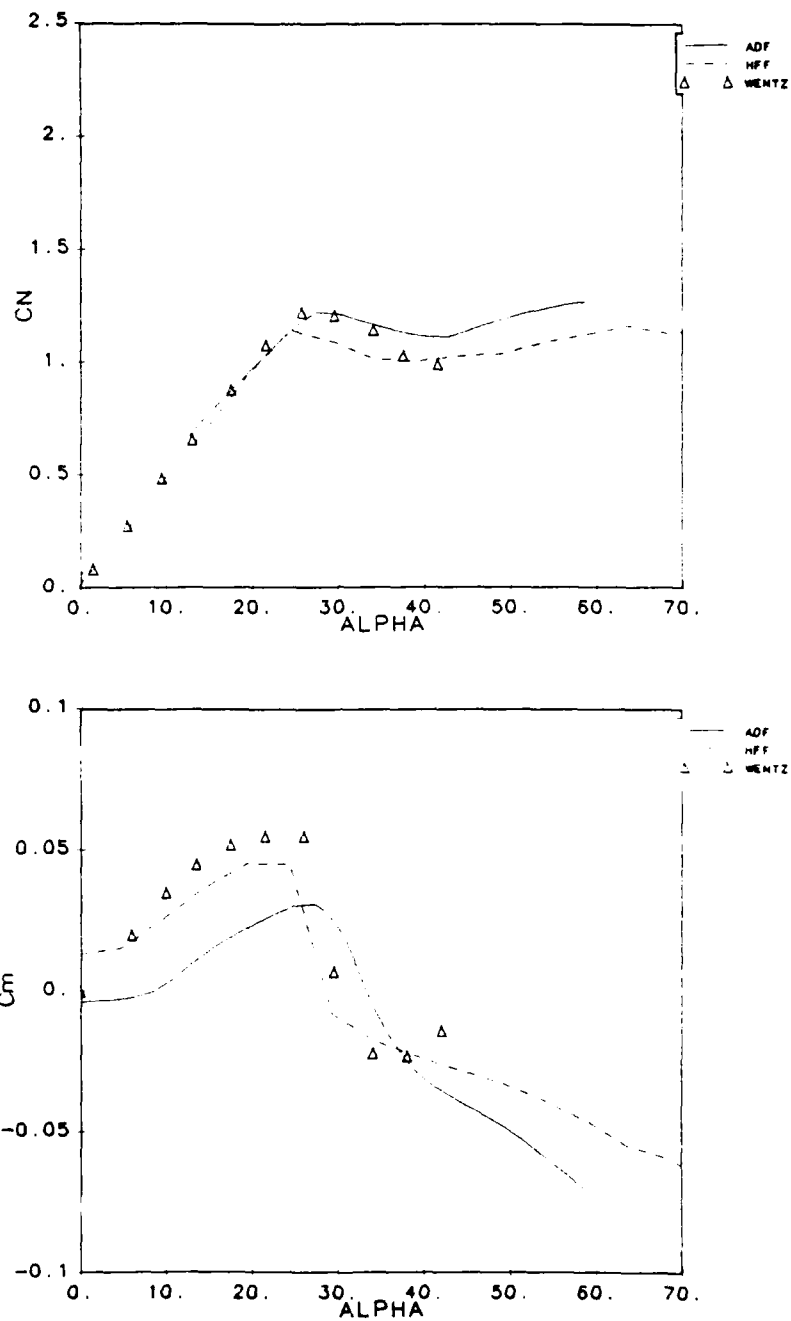


Fig. 5-5 Comparison of Steady 55° Delta Wing Force and Moment Data for the ADF Test ($R_e = 0.45 \times 10^6$), the HFF Test ($R_e = 0.05 \times 10^6$) and Wentz (Ref. 7, $R_e = 0.58 \times 10^6$)

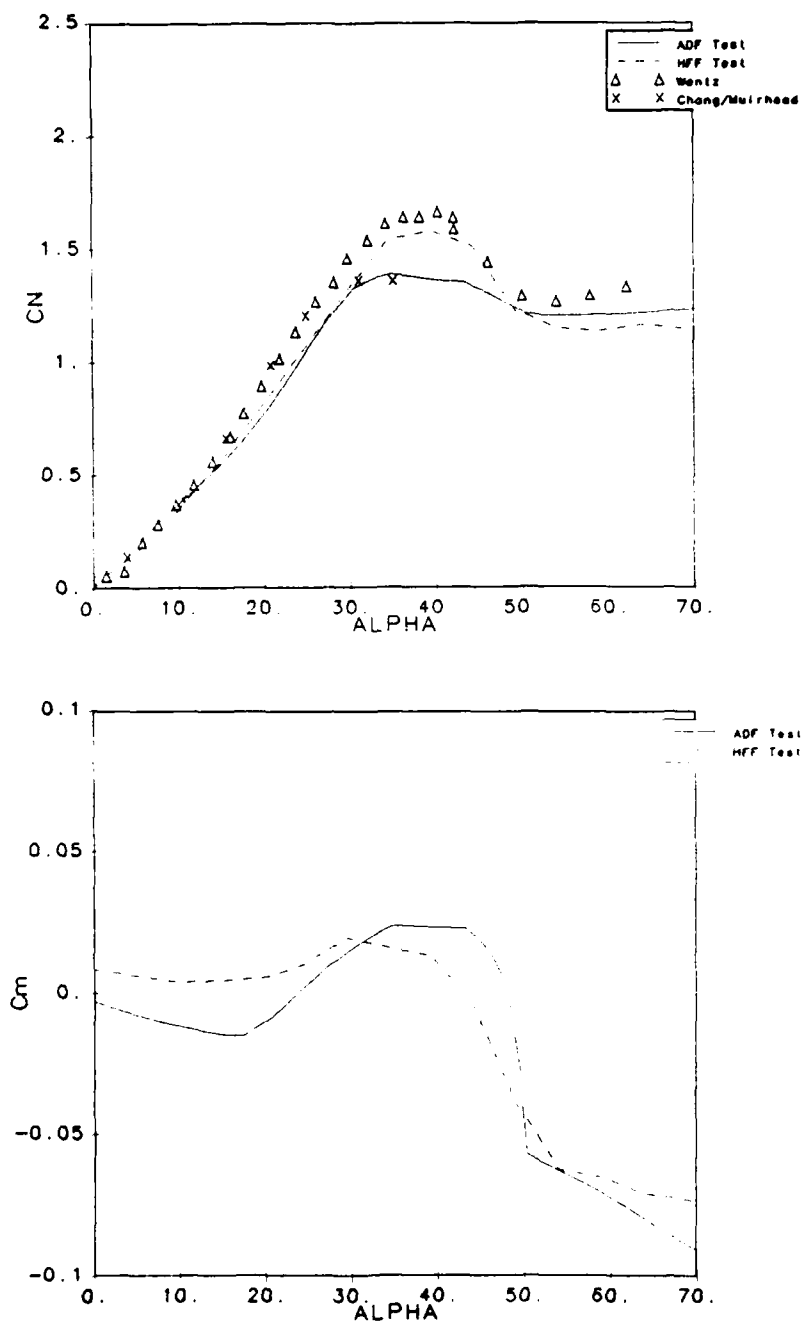


Fig. 5-6 Comparison of Steady 70° Delta Wing Force and Moment Data for the ADF Test ($R_e = 0.6 \times 10^6$), HFF Test ($R_e = 0.066 \times 10^6$), Wentz (Ref. 7, $R_e = 1.1 \times 10^6$) and Chang and Muirhead (Ref. 8, $R_e = 0.7 \times 10^6$)

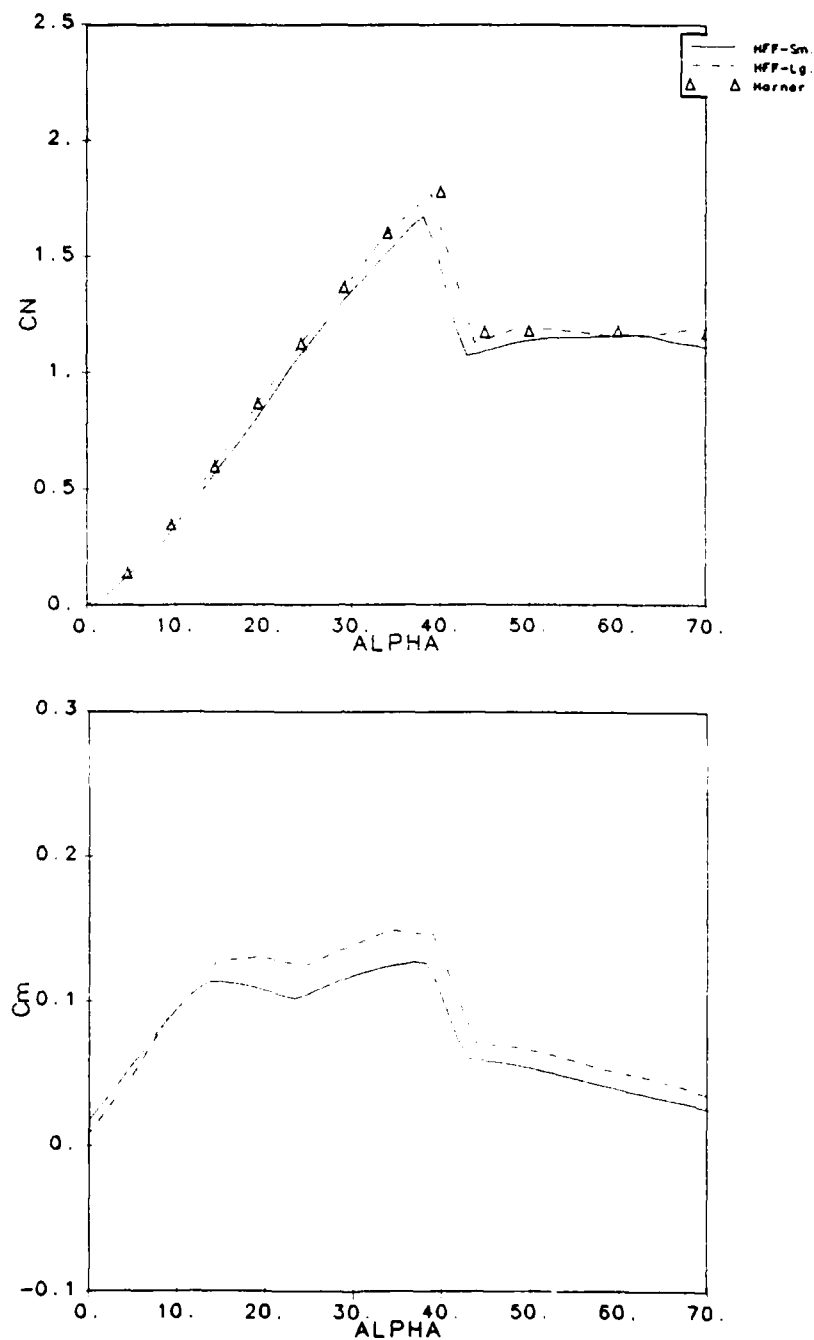


Fig. 5-7 Comparison of Steady Force and Moment Data for the Small and Large Disks in the HFF Test and the Results from Hoerner (Ref. 9)

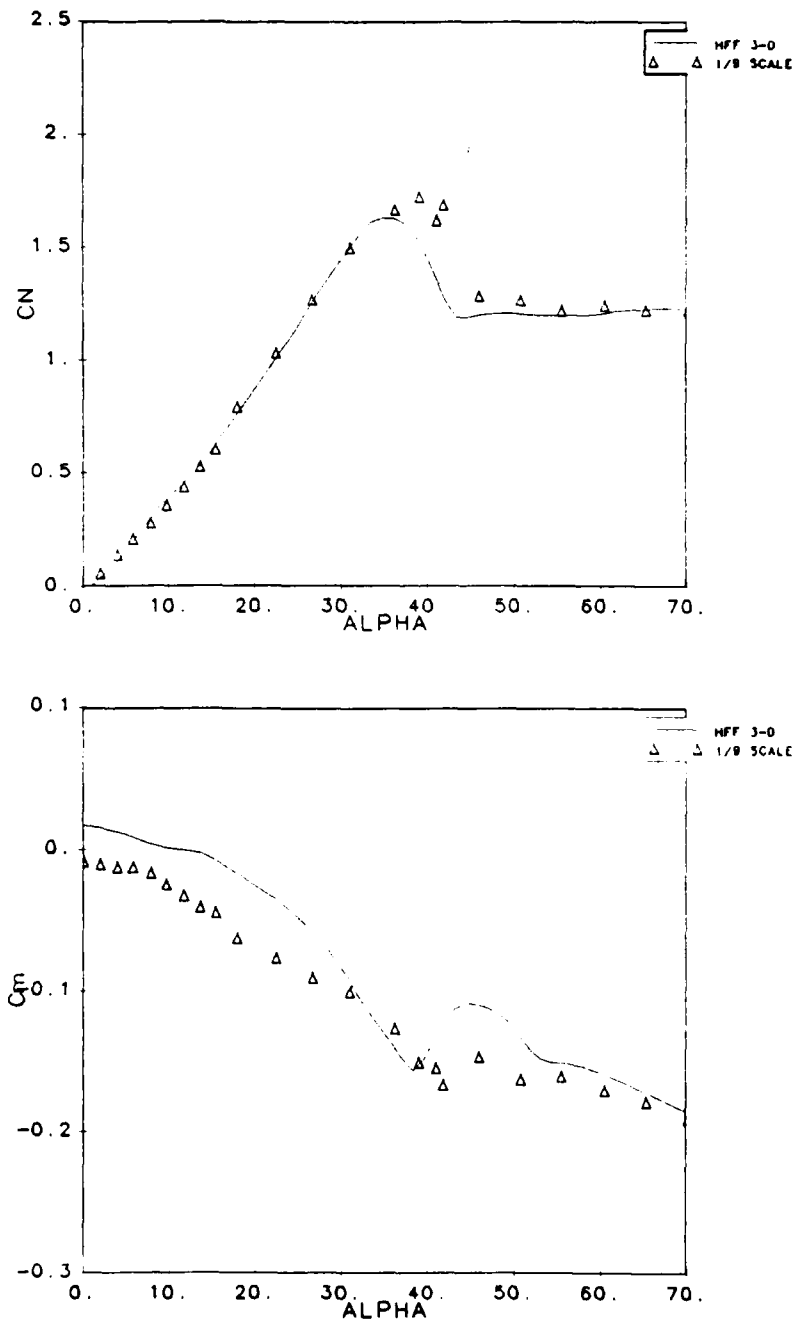
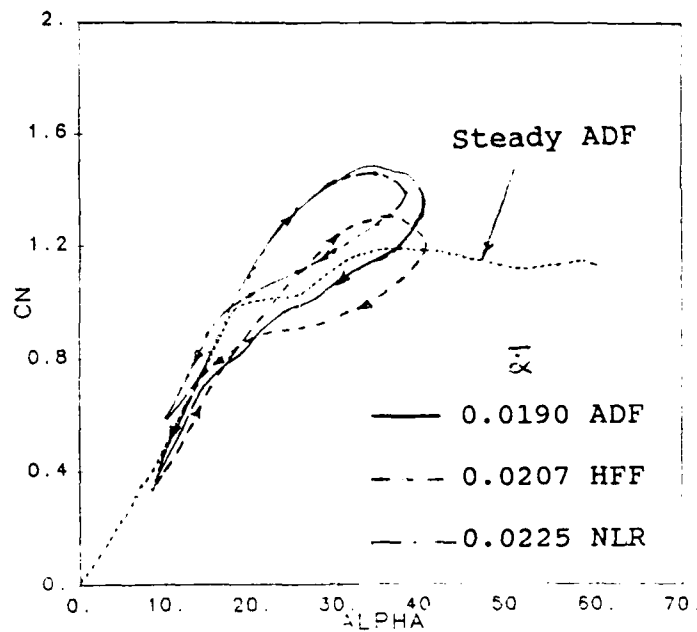
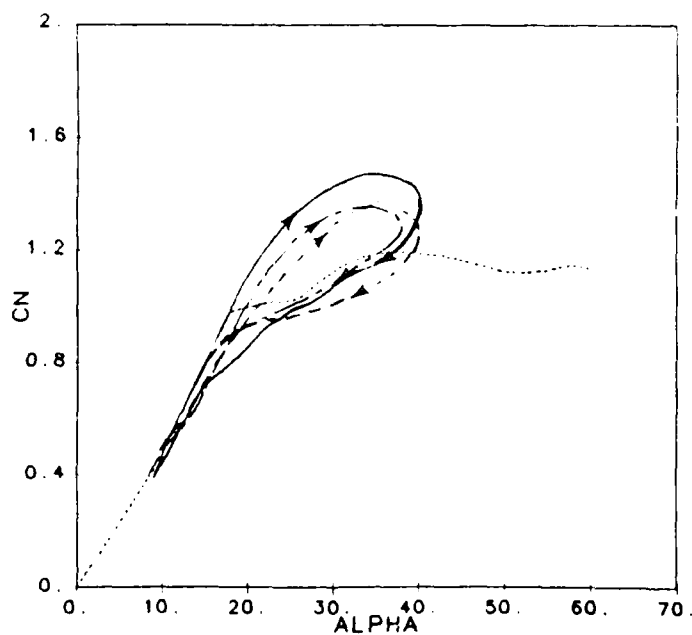


Fig. 5-8 Comparison of Steady 3-D E-7 Force and Moment Data for the HFF Test ($R_e = 0.052 \times 10^6$) and 1/9 - Scale Test (Ref. 10, $R_e = 6.5 \times 10^6$)

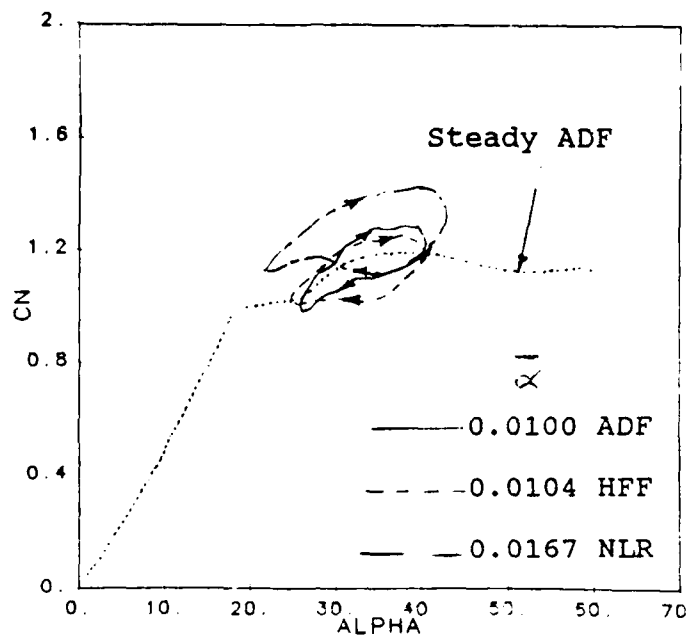


(a) Unshifted Loops

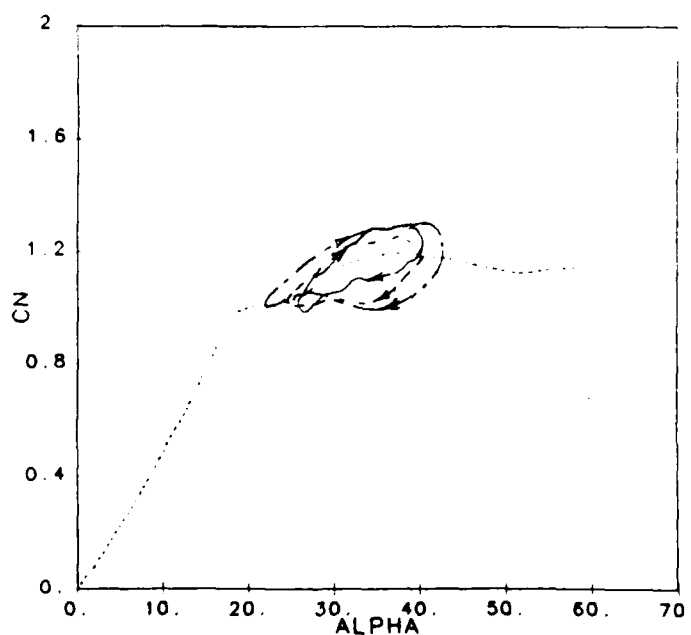


(b) Shifted Loops

Fig. 5-9 Comparison of Unsteady Straked Wing Normal Force Data for the ADF and HFF Tests with NLR Results (Ref. 5) over the Incidence Range of 8° to 40°

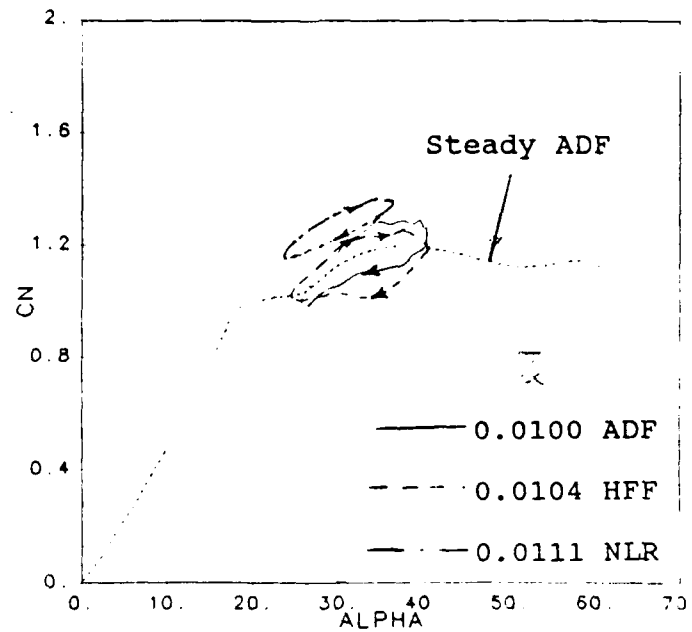


(a) Unshifted Loops

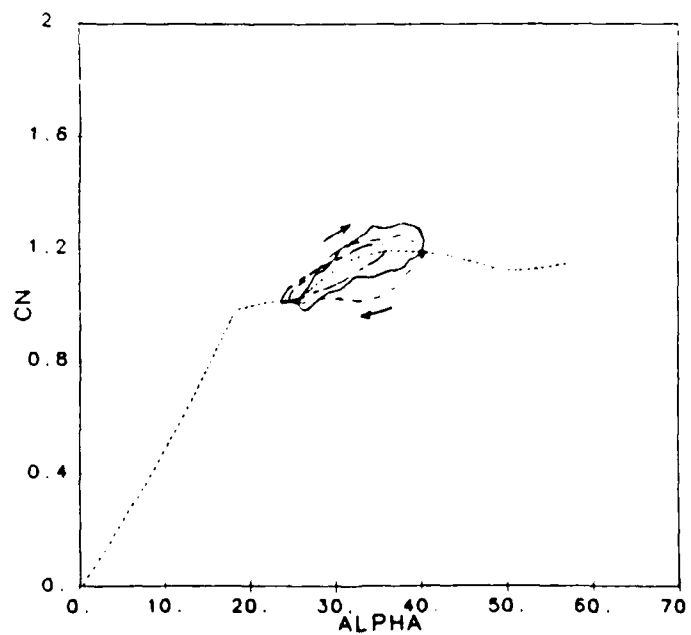


(b) Shifted Loops

Fig. 5-10 Comparison of Unsteady Straked Wing Normal Force Data for the ADF and HFF Tests with NLR Results (Ref. 5) over the Incidence Range of 22° to 42°

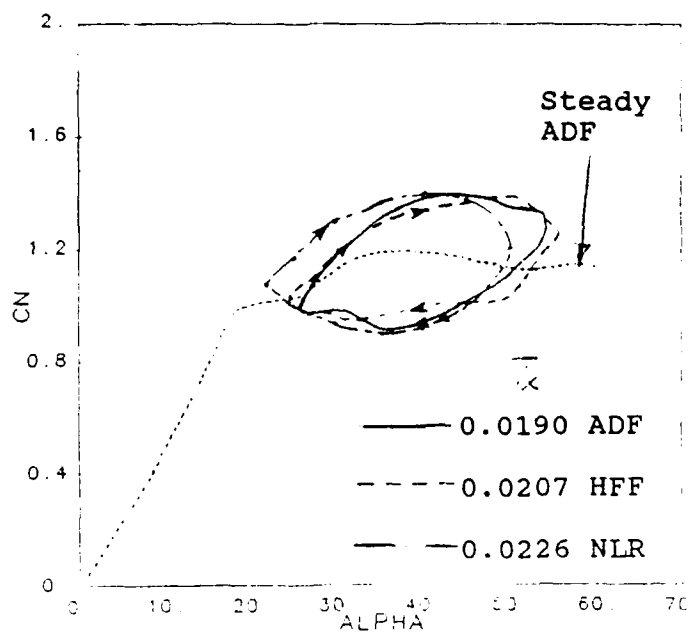


(a) Unshifted Loops

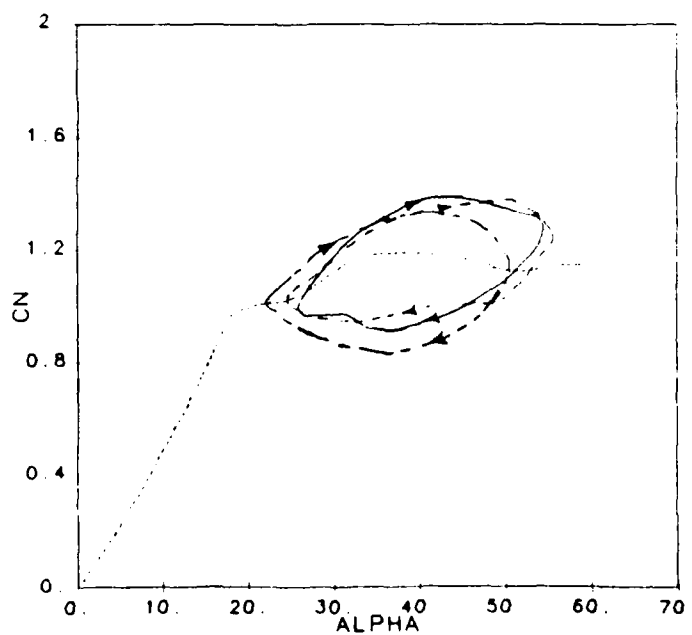


(b) Shifted Loops

Fig. 5-11 Comparison of Unsteady Straked Wing Normal Force Data for the ADF and HFF Tests with NLR Results (Ref. 5) over the Incidence Range of 24° to 38°

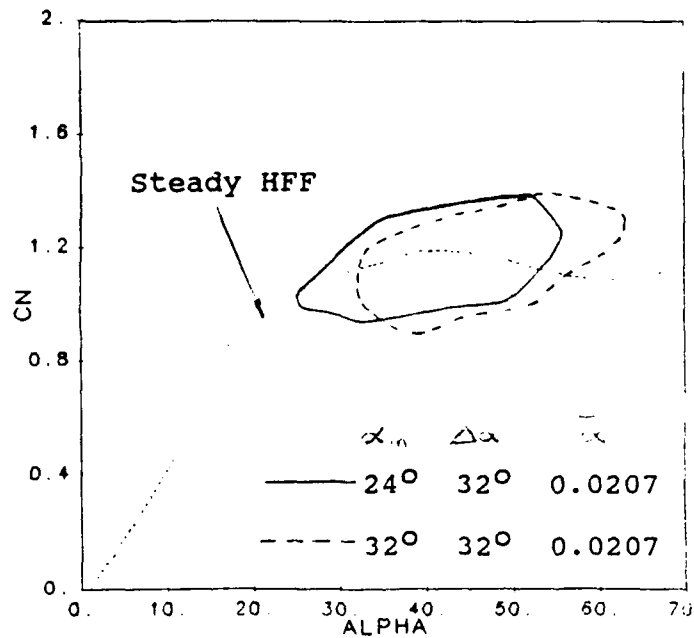


(a) Unshifted Loops

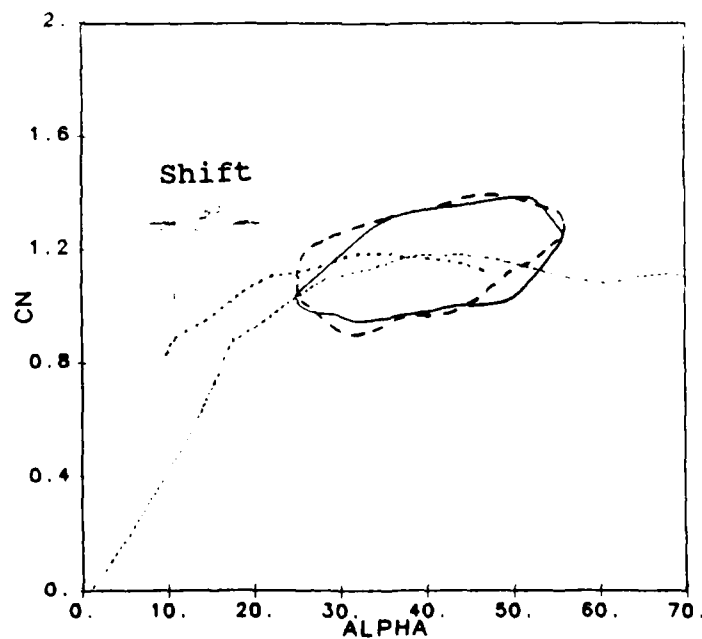


(b) Shifted Loops

Fig. 5-12 Comparison of Unsteady Straked Wing Normal Force Data for the ADF and HFF Tests with NLR Results (Ref. 5) over the Incidence Range of 24° to 56°

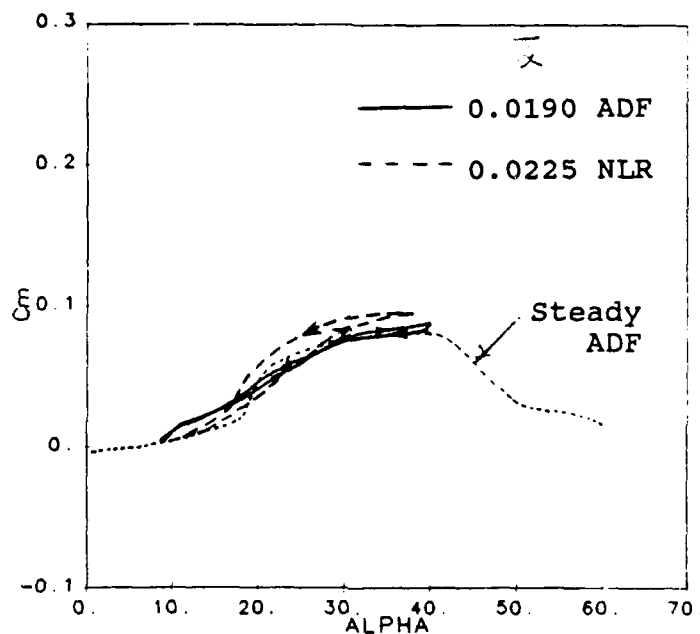


(a) Unshifted Loops

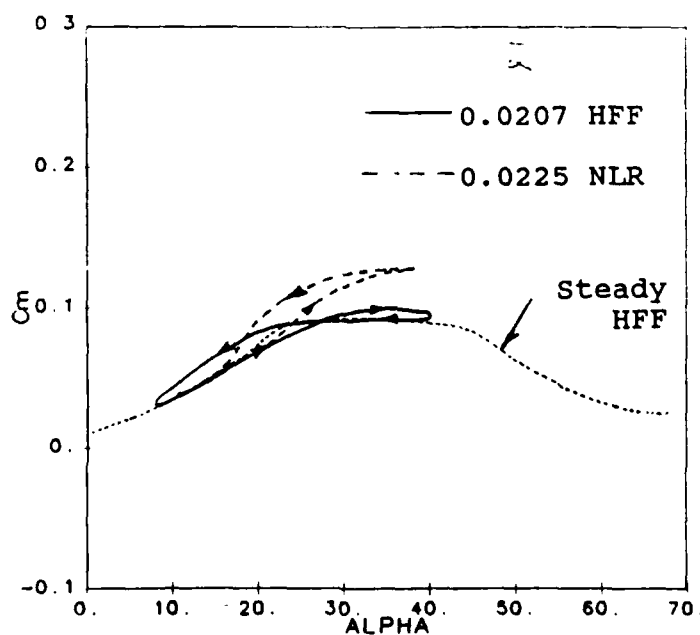


(b) Shifted Loops

Fig. 5-13 Comparison of Unsteady Straked Wing Normal Force Data for Two HFF Runs at Different Incidences But of Identical Dynamic Conditions

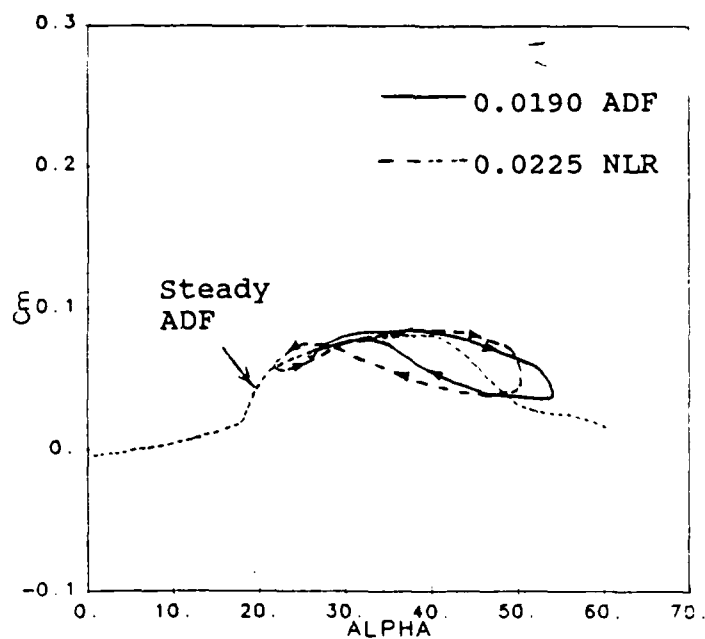


(a) ADF Results

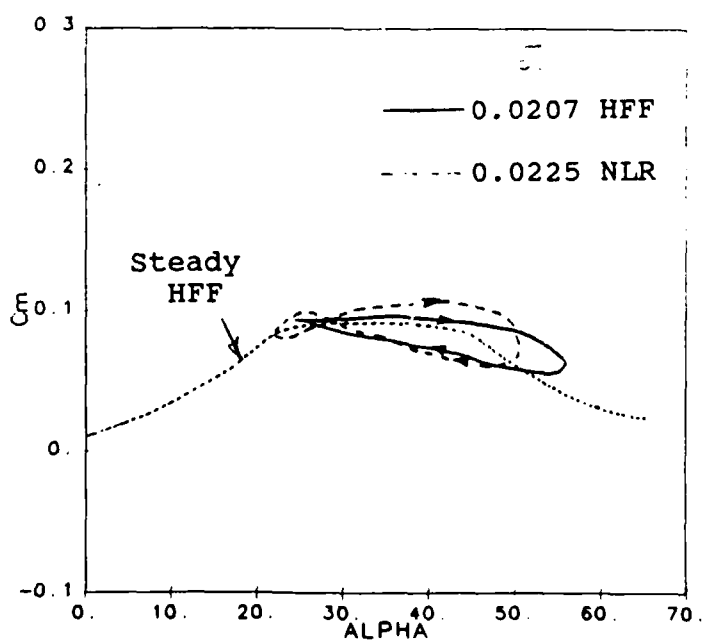


(b) HFF Results

Fig. 5-14 Comparison of Unsteady Straked Wing Pitching Moment Data for ADF and HFF Tests with Shifted NLR Results (Ref. 5) Over the Incidence Range of 8° to 40°



(a) ADF Results



(b) HFF Results

Fig. 5-15 Comparison of Unsteady Straked Wing Pitching Moment Data for ADF and HFF Tests with Shifted NLR Results (Ref. 5) Over the Incidence Range of 22° to 56°

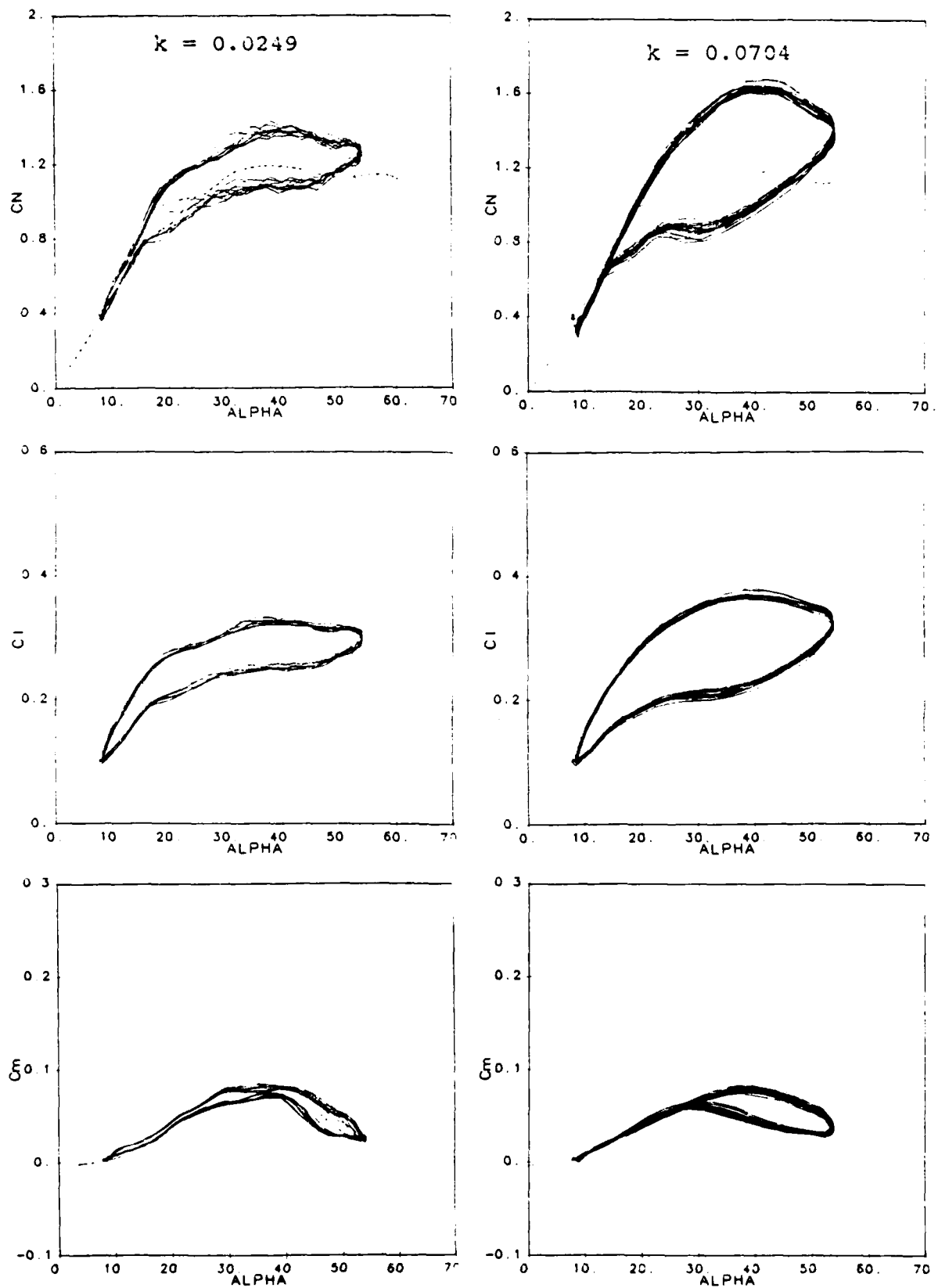


Fig. 6-1 Repeatability of Straked Wing Dynamic Data in the ADF at Two Frequencies

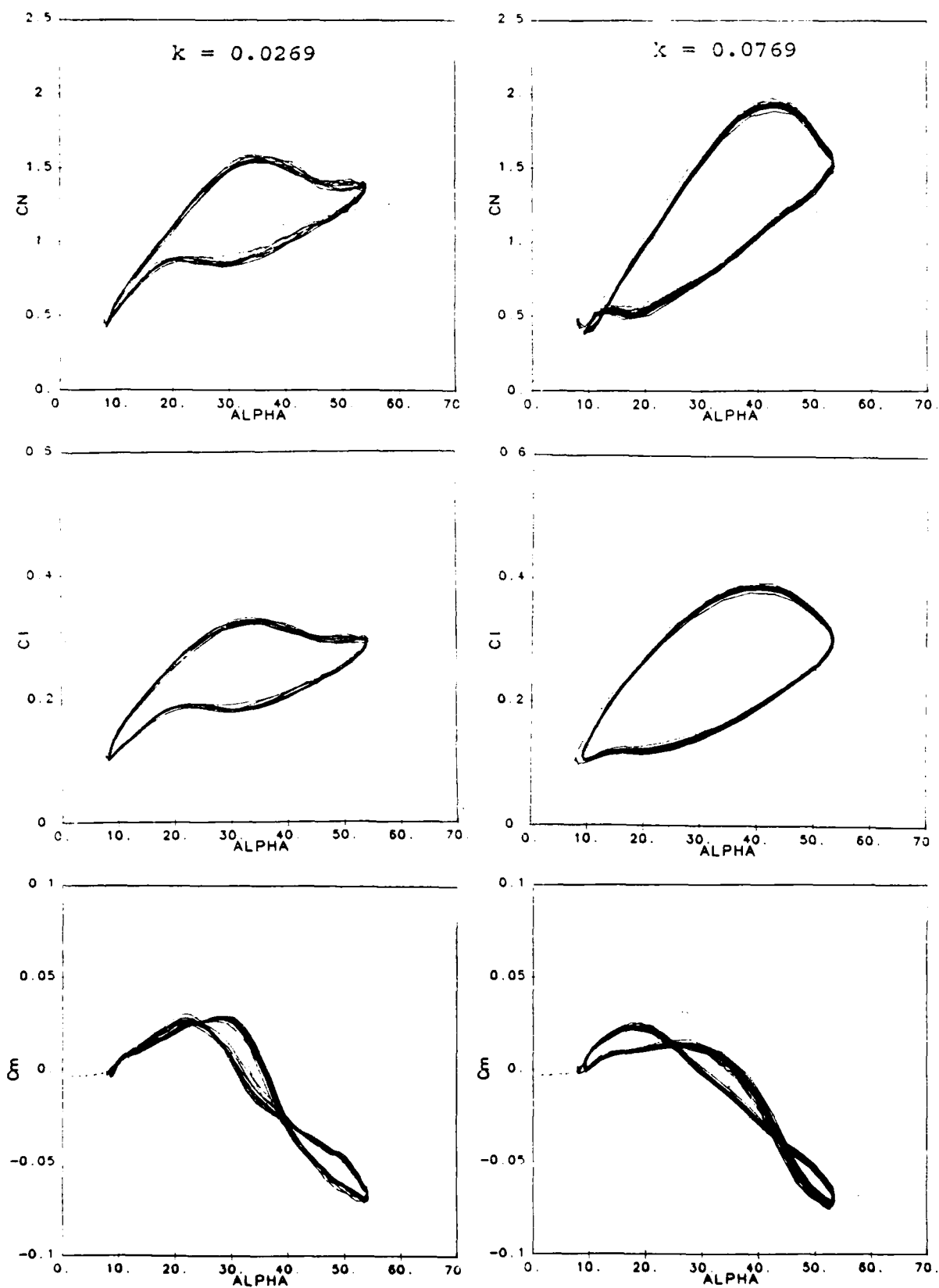


Fig. 6-2 Repeatability of 55° Delta Dynamic Data in the ADF at Two Frequencies

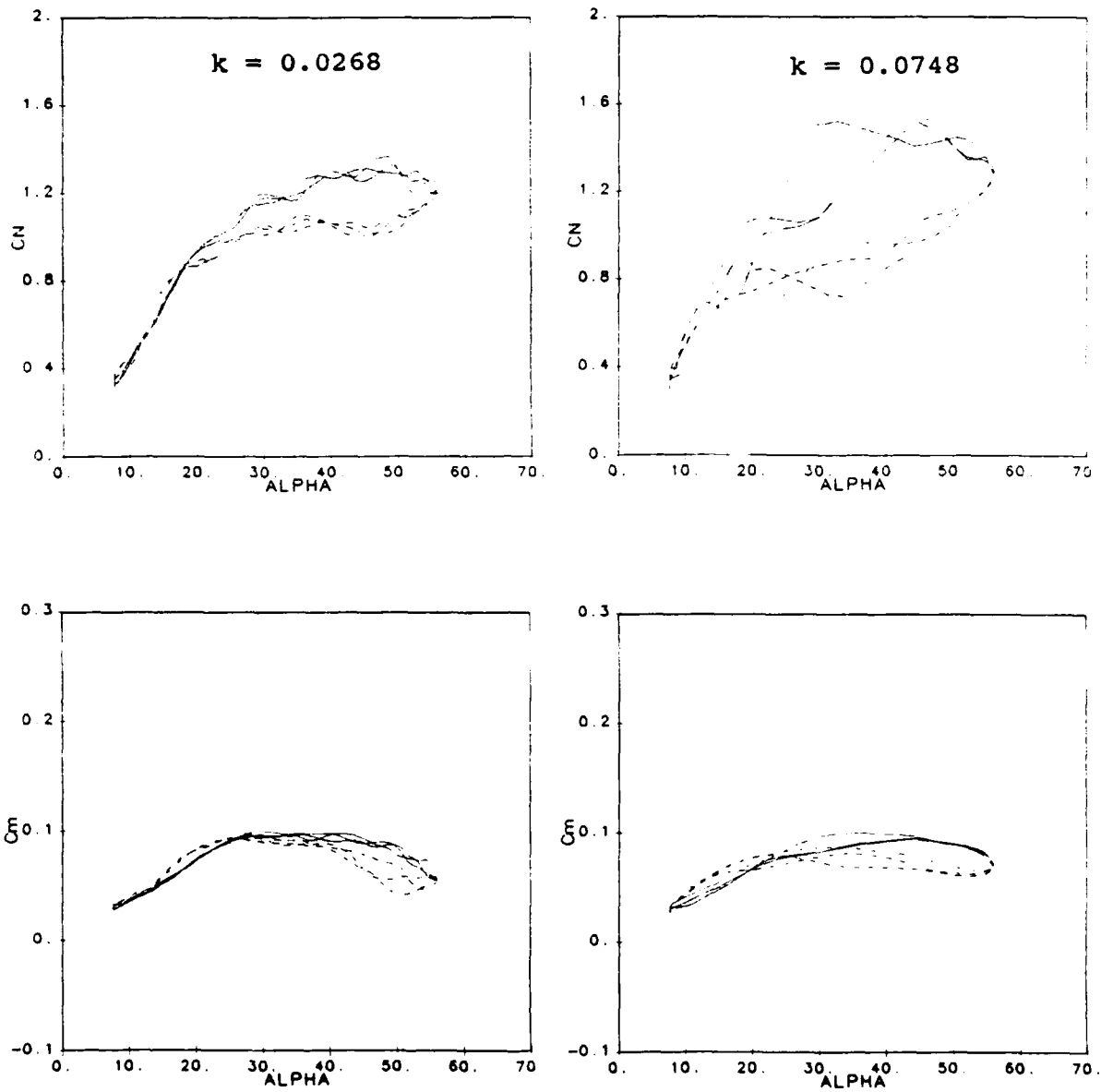


Fig. 6-3 Repeatability of Straked Wing Dynamic Data in the HFF at Two Frequencies

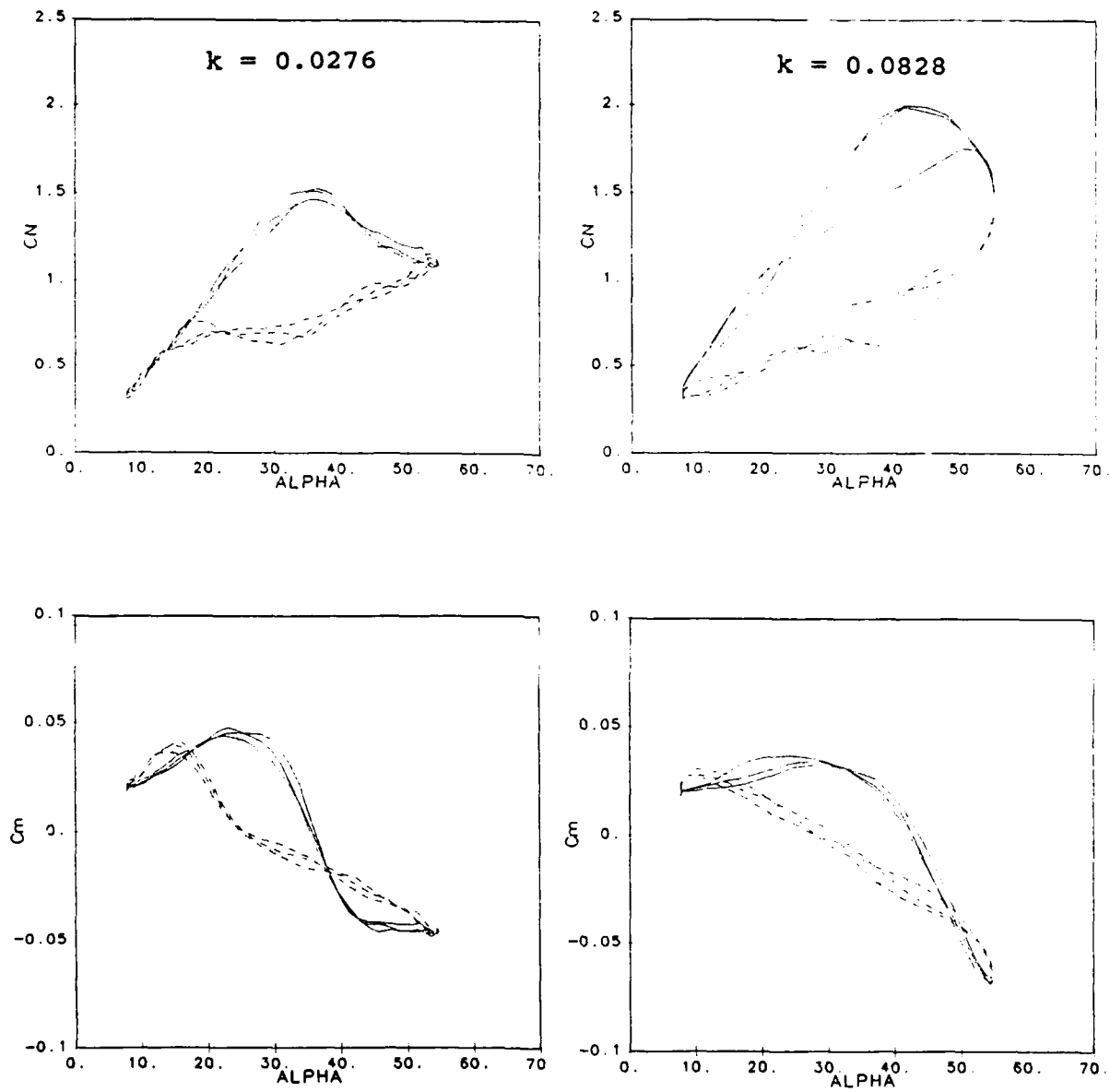


Fig. 6-4 Repeatability of 55° Delta Dynamic Data in the HFF at Two Frequencies

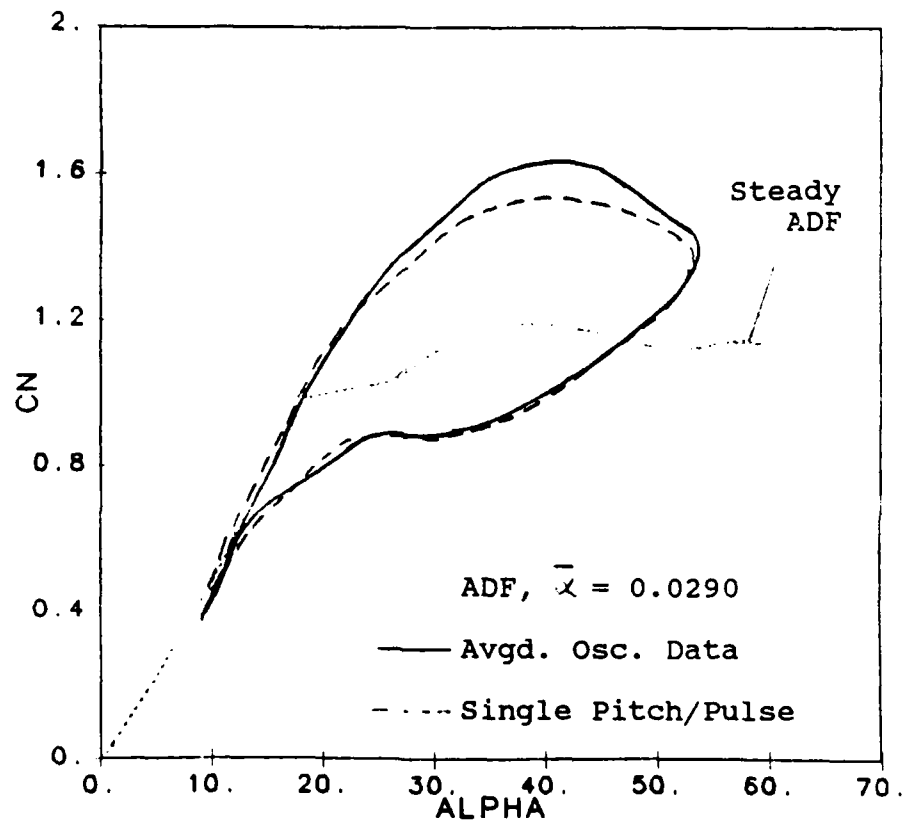
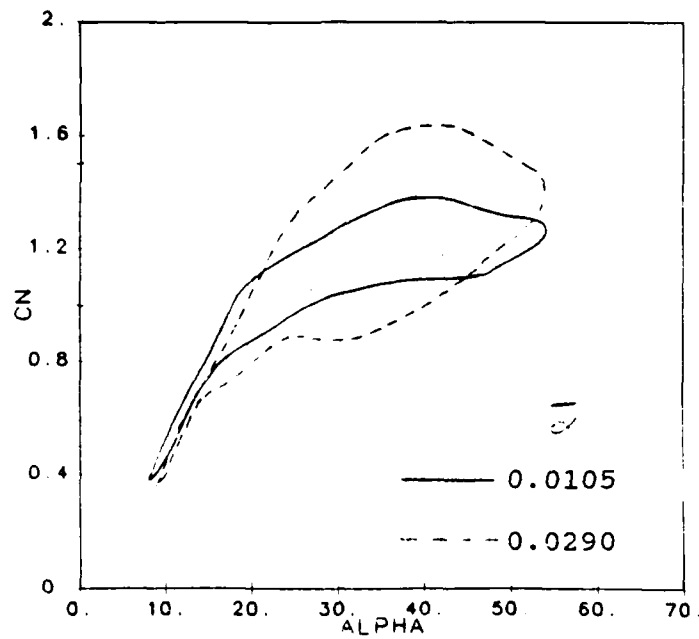
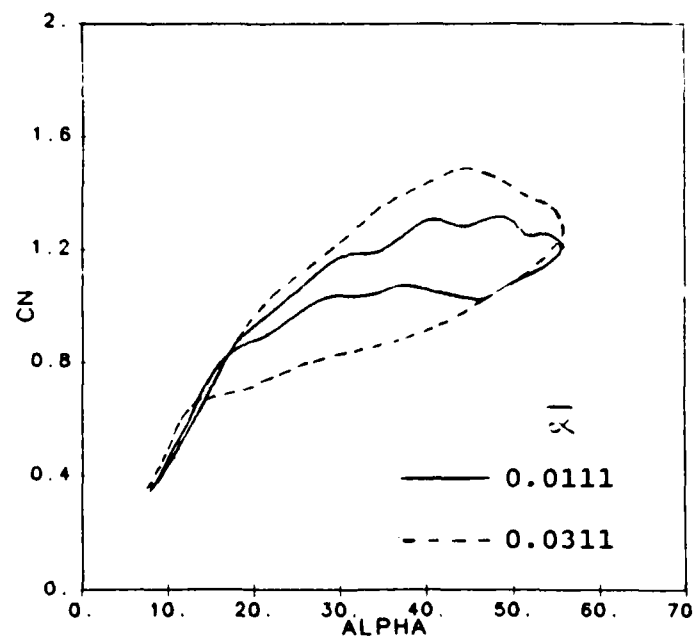


Fig. 6-5 Comparison of Oscillatory and Pitch/Pulse Normal Force Data for the Straked Wing in the ADF at One Frequency

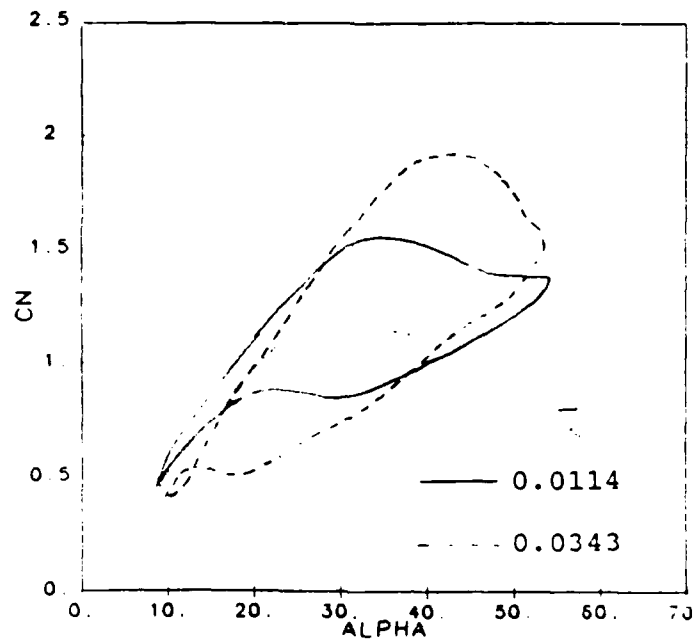


(a) ADF Results

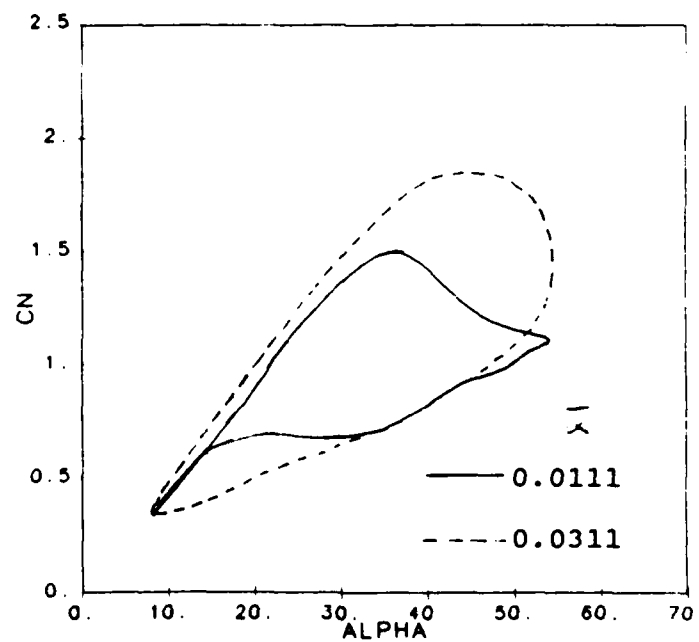


(b) HFF Results

Fig. 6-6 Effect of Frequency for the Straked Wing in ADF and HFF Tests

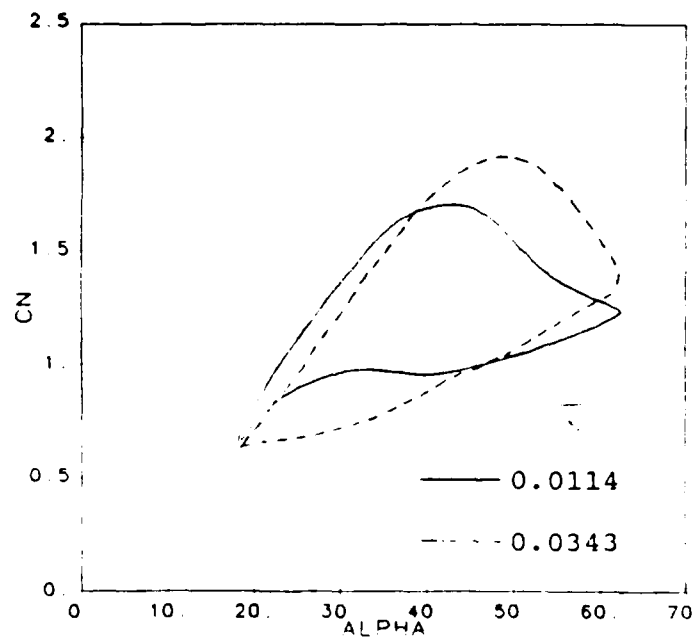


(a) ADF Results

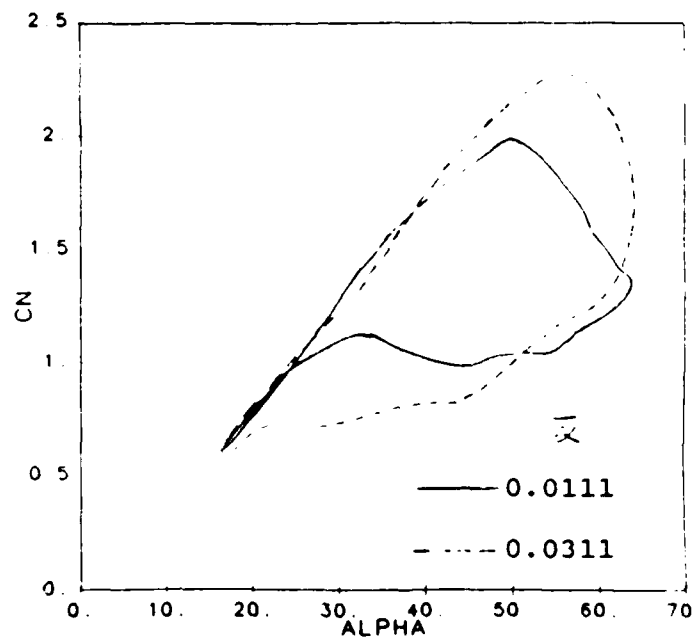


(b) HFF Results

Fig. 6-7 Effect of Frequency for the 55° Delta in ADF and HFF Tests

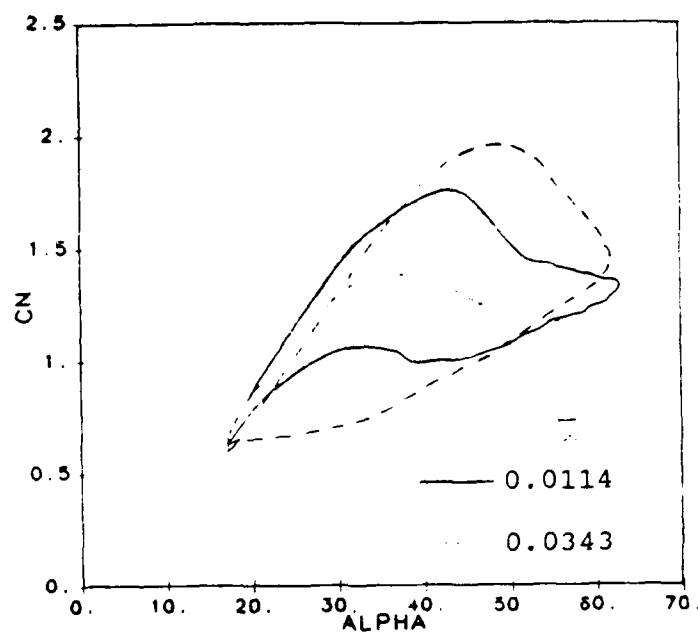


(a) ADF Results

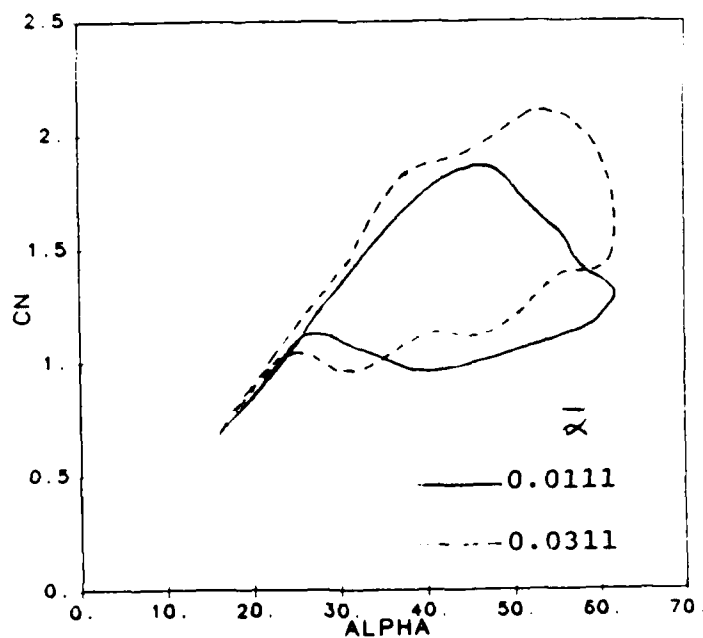


(b) HFF Results

Fig. 6-8 Effect of Frequency for the 70° Delta in ADF and HFF Tests



(a) ADF Results



(b) HFF Results

Fig. 6-9 Effect of Frequency for the $70^\circ/30^\circ$ Cranked Wing in ADF and HFF Tests

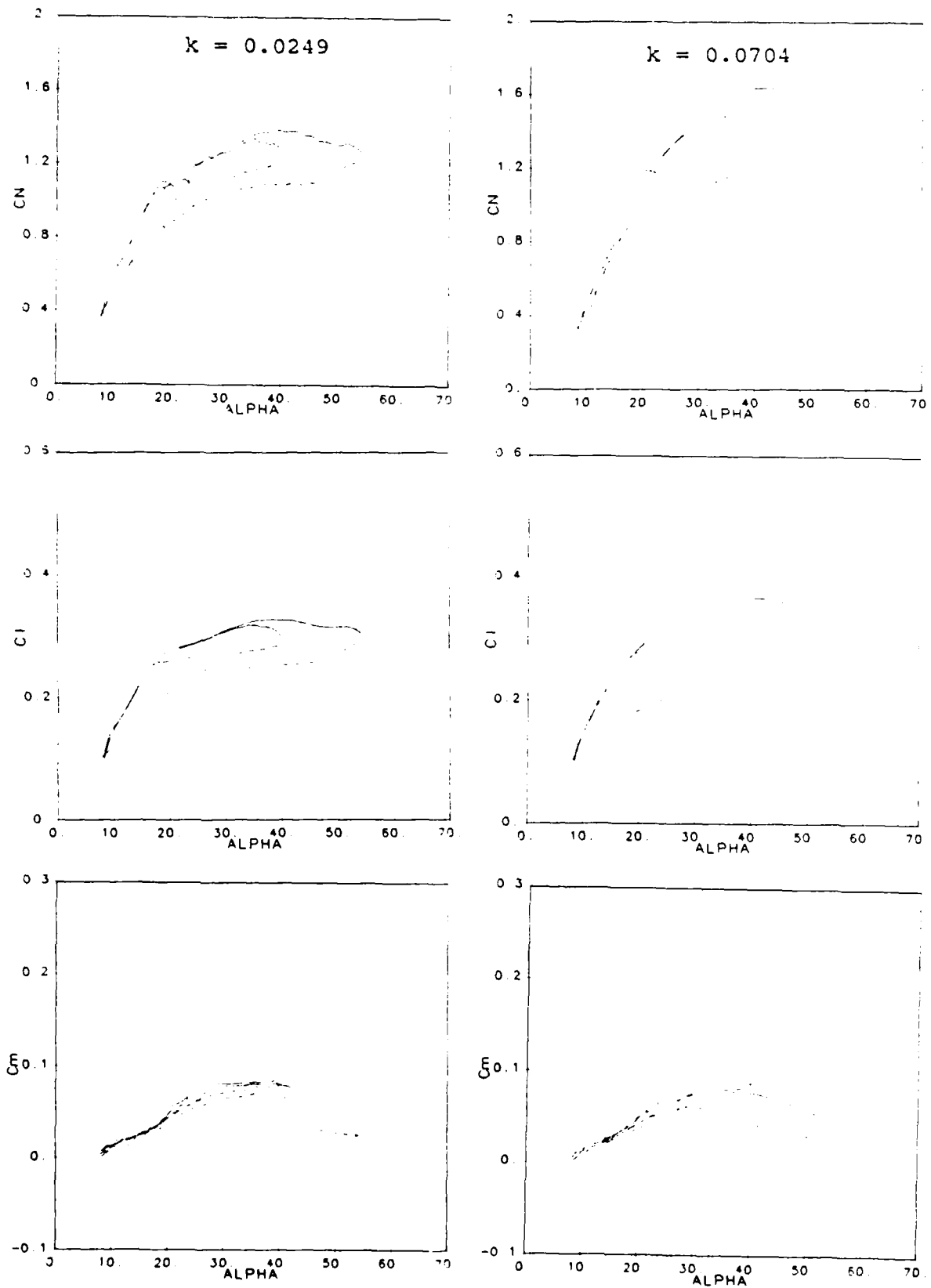


Fig. 6-10 Effect of Peak Angle for a Fixed Starting Angle in ADF Tests of the Straked Wing

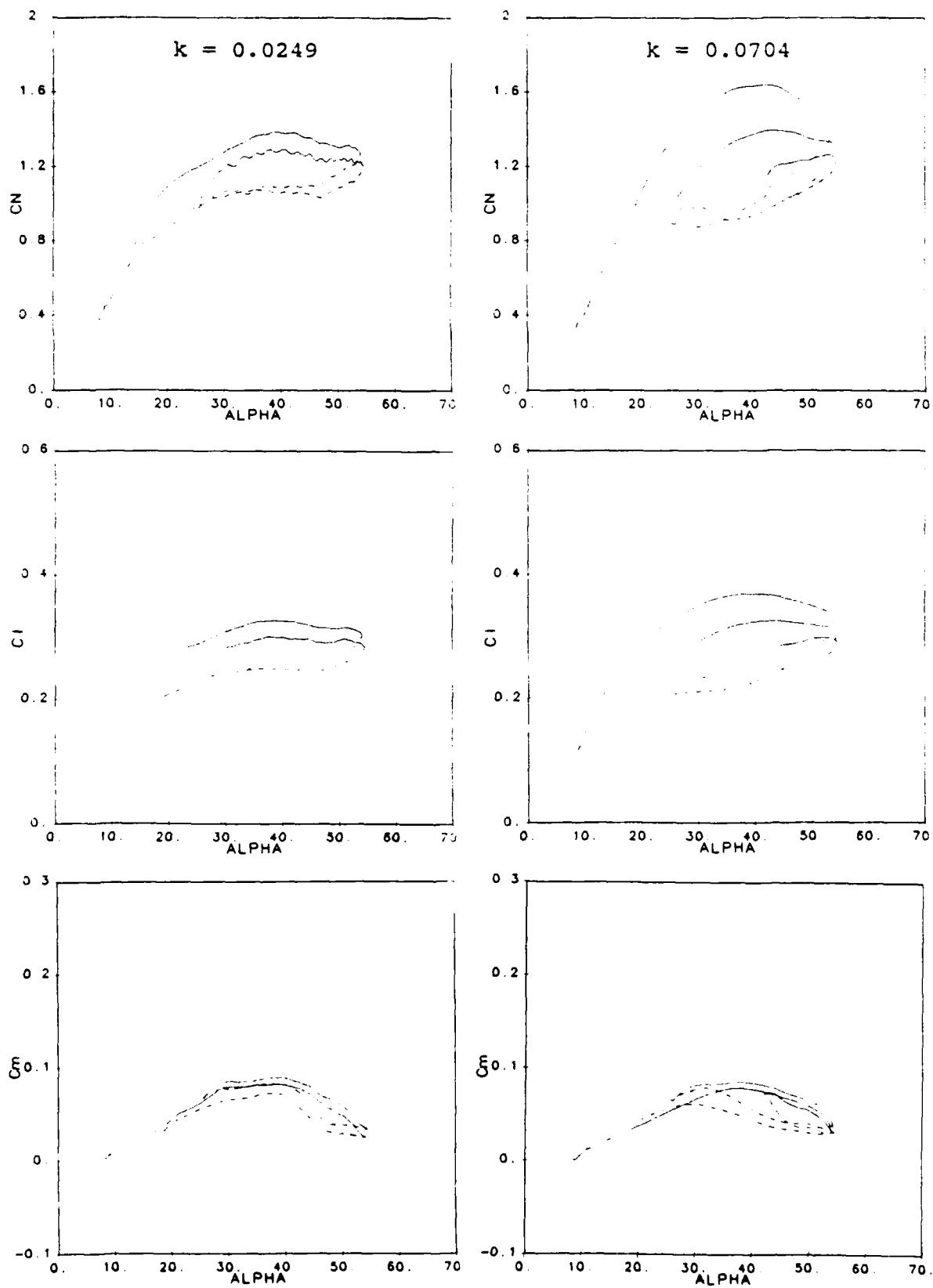


Fig. 6-11 Effect of Starting Angle for a Fixed Peak Angle in ADF Tests of the Straked Wing

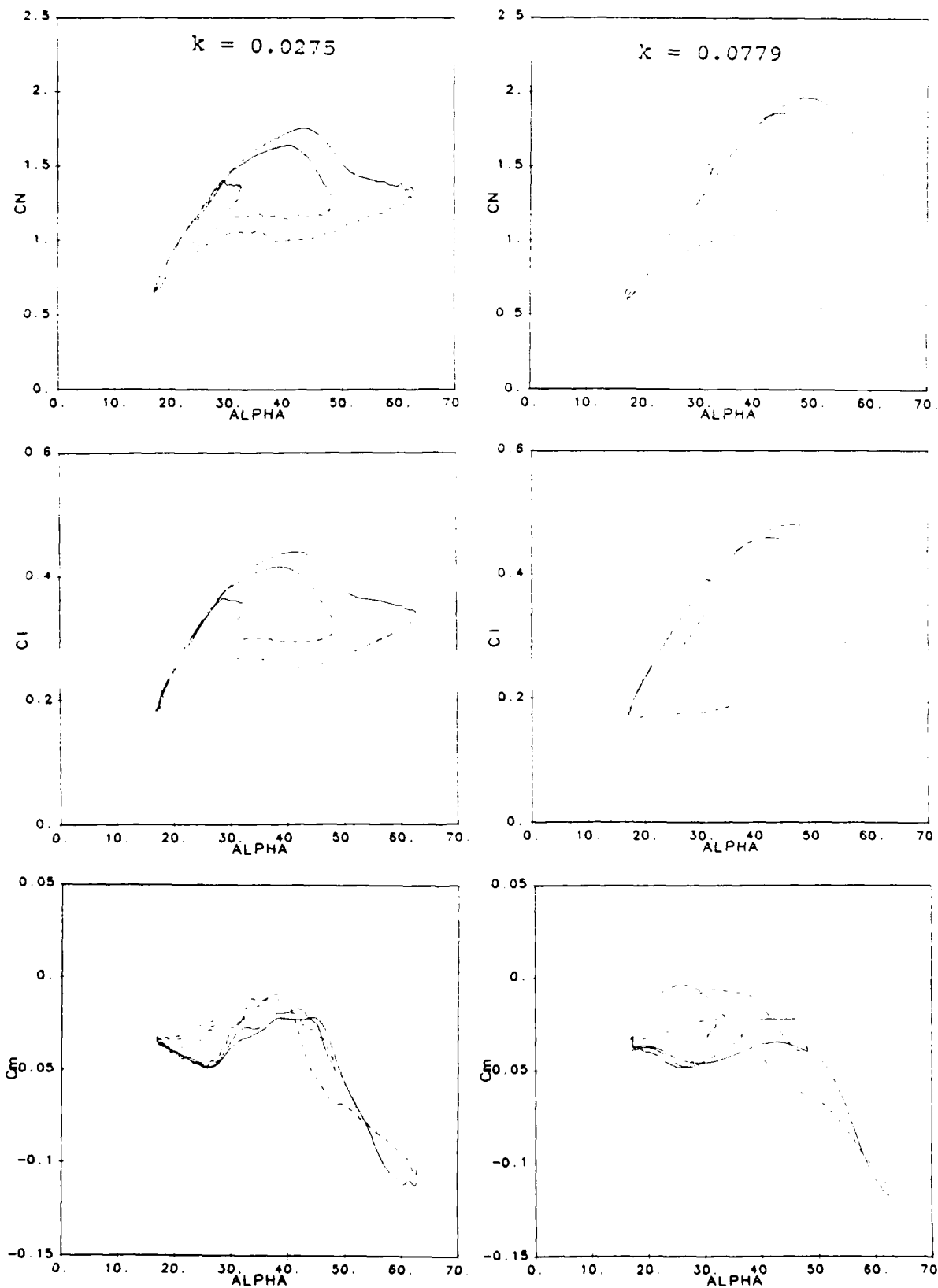


Fig. 6-12 Effect of Peak Angle for a Fixed Starting Angle in ADF Tests of the $70^\circ/30^\circ$ Cranked Wing

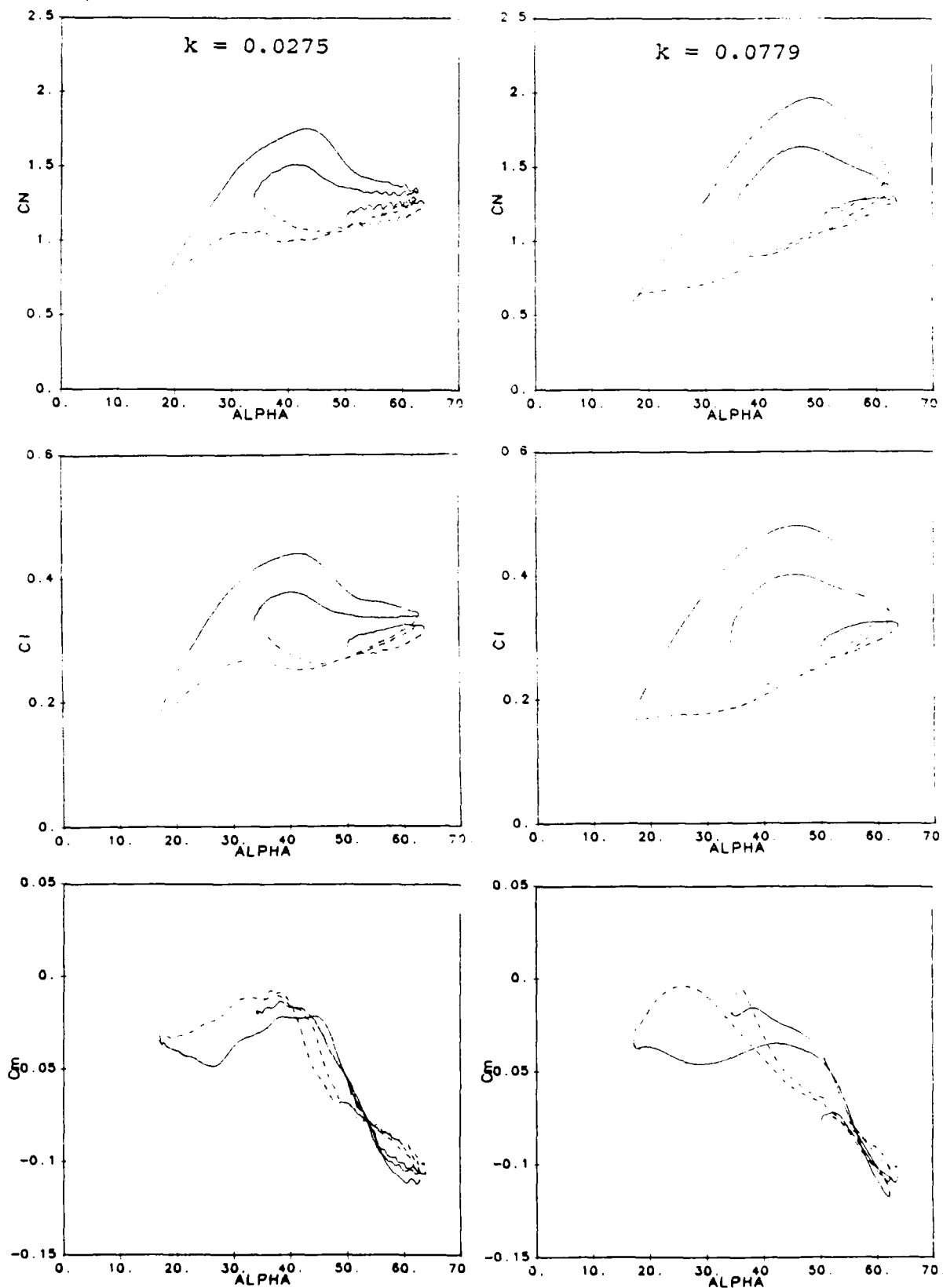
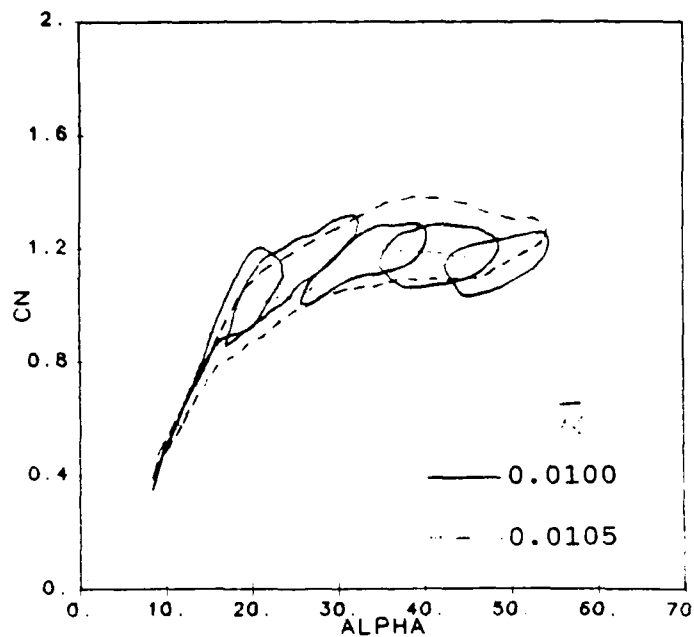
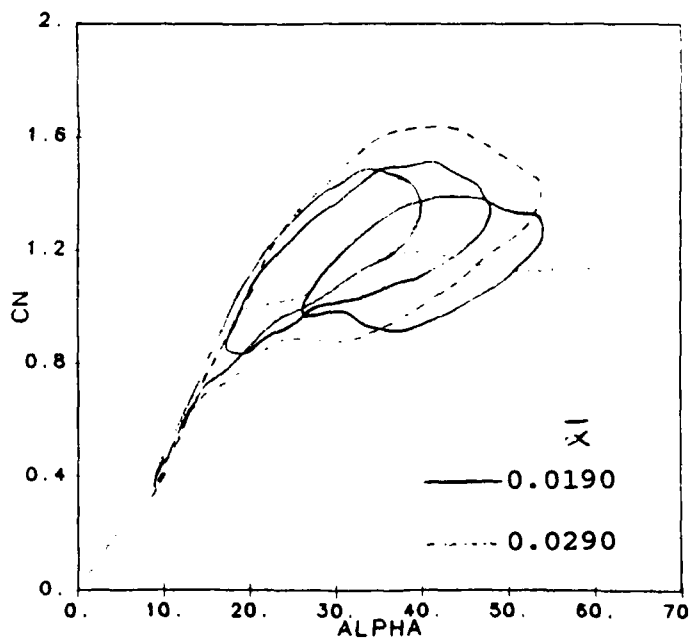


Fig. 6-13 Effect of Starting Angle for a Fixed Peak Angle in ADF Tests of the 70°/30° Cranked Wing

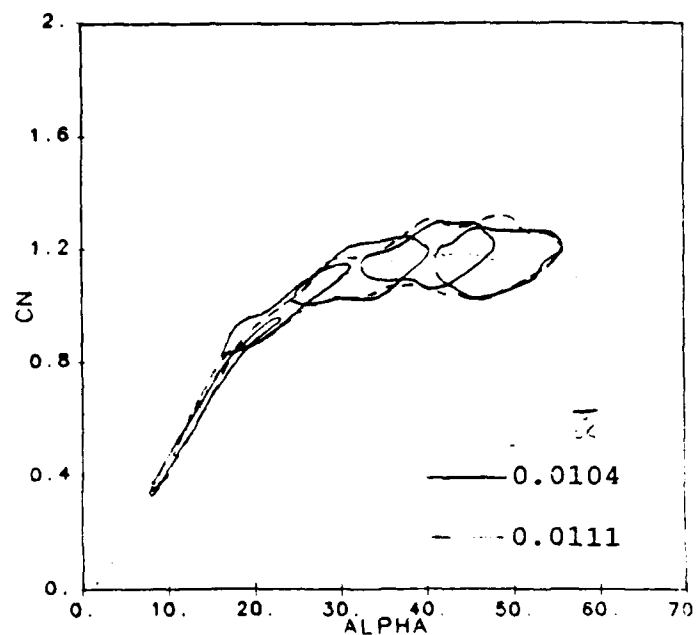


(a) Low Frequency, $k = 0.0249$

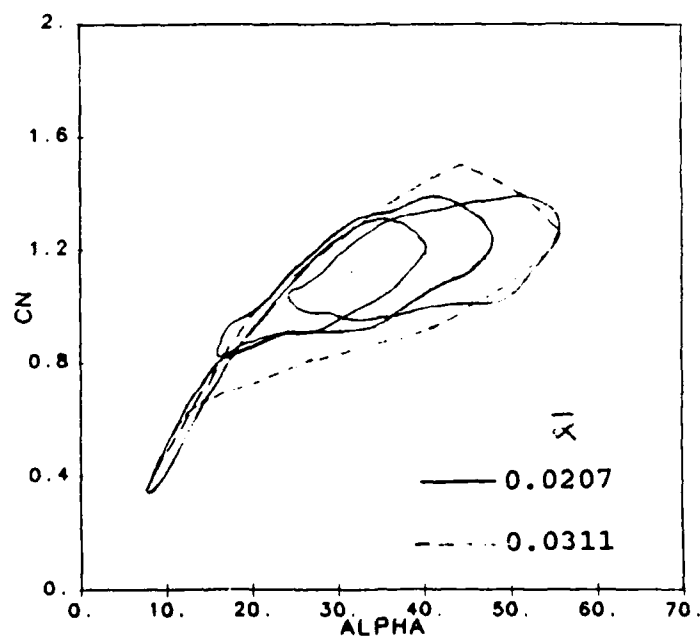


(b) High Frequency, $k = 0.0704$

Fig. 6-14 Time History Effects in ADF Tests of the Straked Wing at Similar $\bar{\alpha}$ Values and an Incidence Range of 8° to 56°

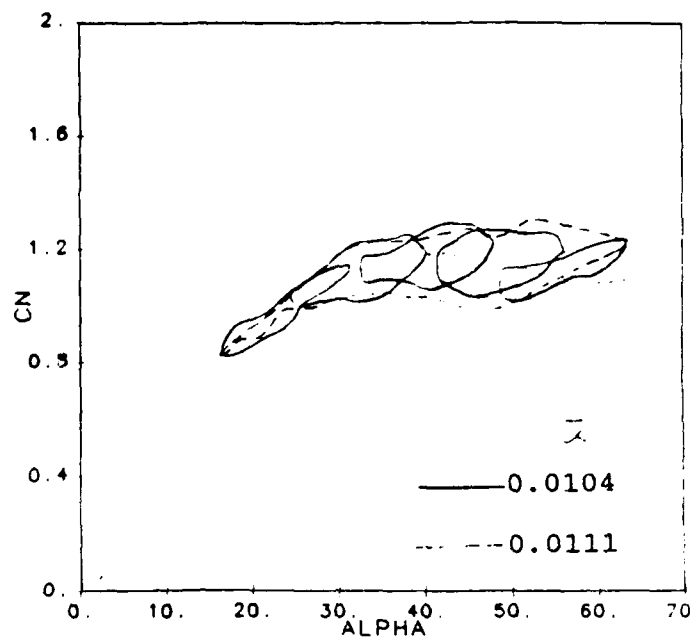


(a) Low Frequency, $k = 0.0268$

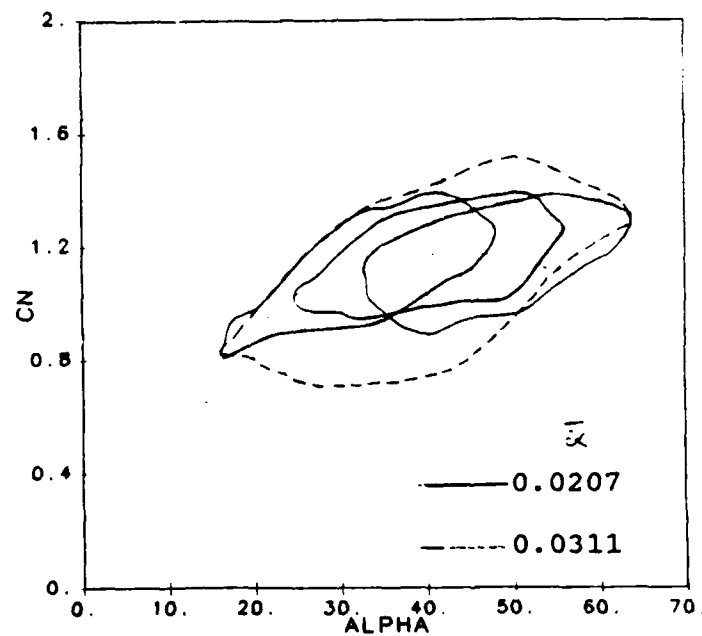


(b) High Frequency, $k = 0.0802$

Fig. 6-15 Time History Effects in HFF Tests of the Straked Wing at Similar $\bar{\alpha}$ Values and an Incidence Range of 8° to 56°

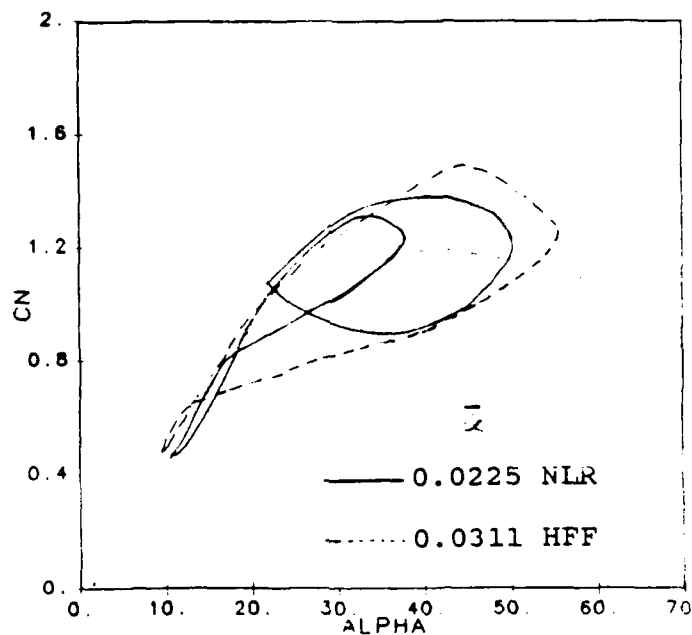


(a) Low Frequency, $k = 0.0268$

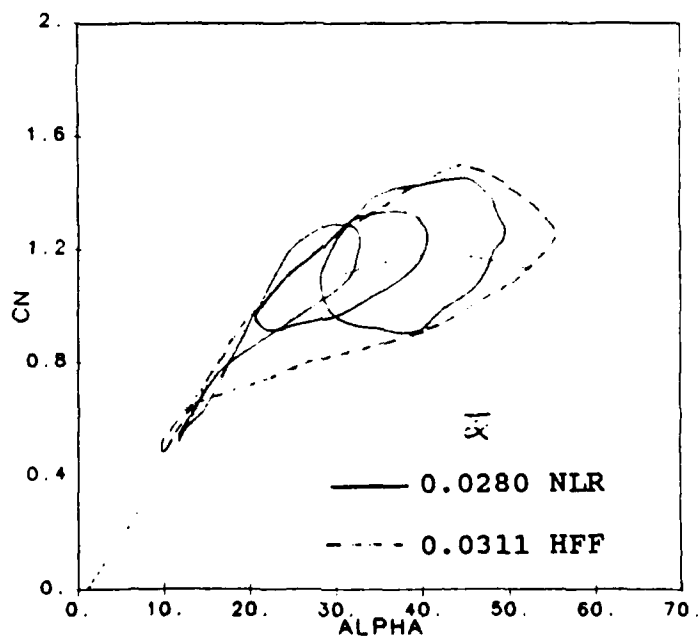


(b) High Frequency, $k = 0.0802$

Fig. 6-16 Time History Effects in HFF Tests of the Straked Wing at Similar $\bar{\alpha}$ Values and an Incidence Range of 16° to 64°



(a) NLR Results for $k = 0.096$



(b) NLR Results for $k = 0.160$

Fig. 6-17 Comparison of HFF Data at High Amplitude and Frequency with NLR Results (Ref. 5) at Similar $\bar{\alpha}$ values at Two Frequencies

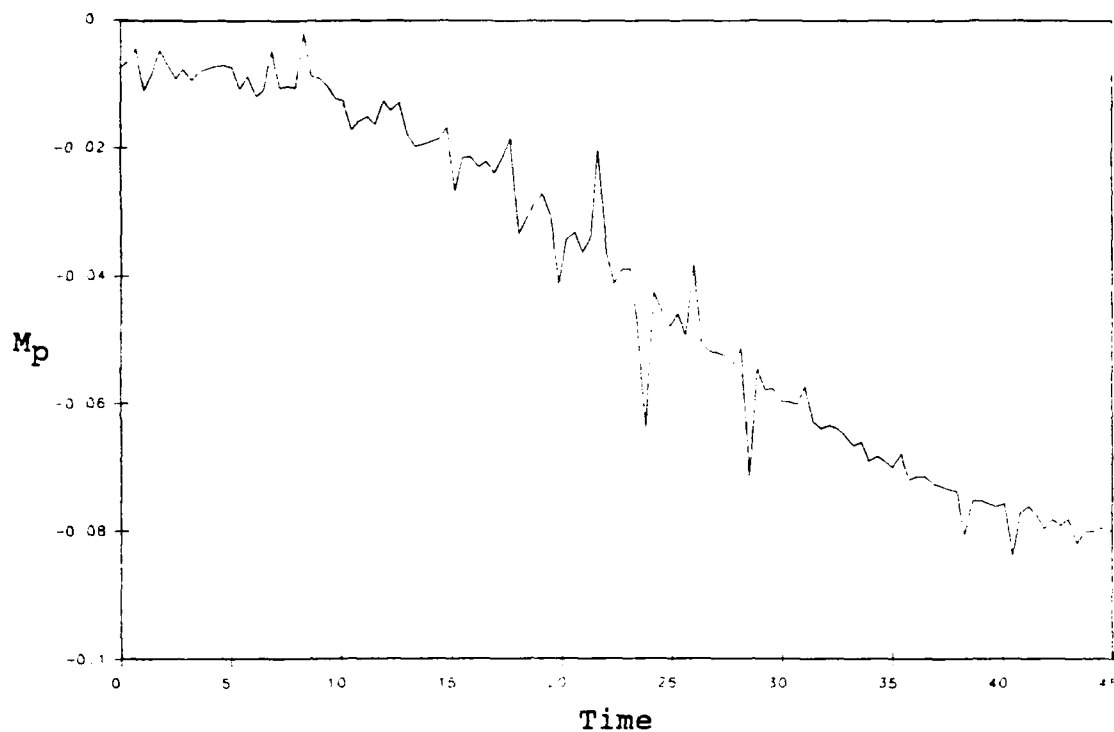


Fig. 6-18 Time History of Pitching Moment for an 86.2 sec Pitch/Pulse of the Straked Wing in the HFF for $V = 0$ FPS

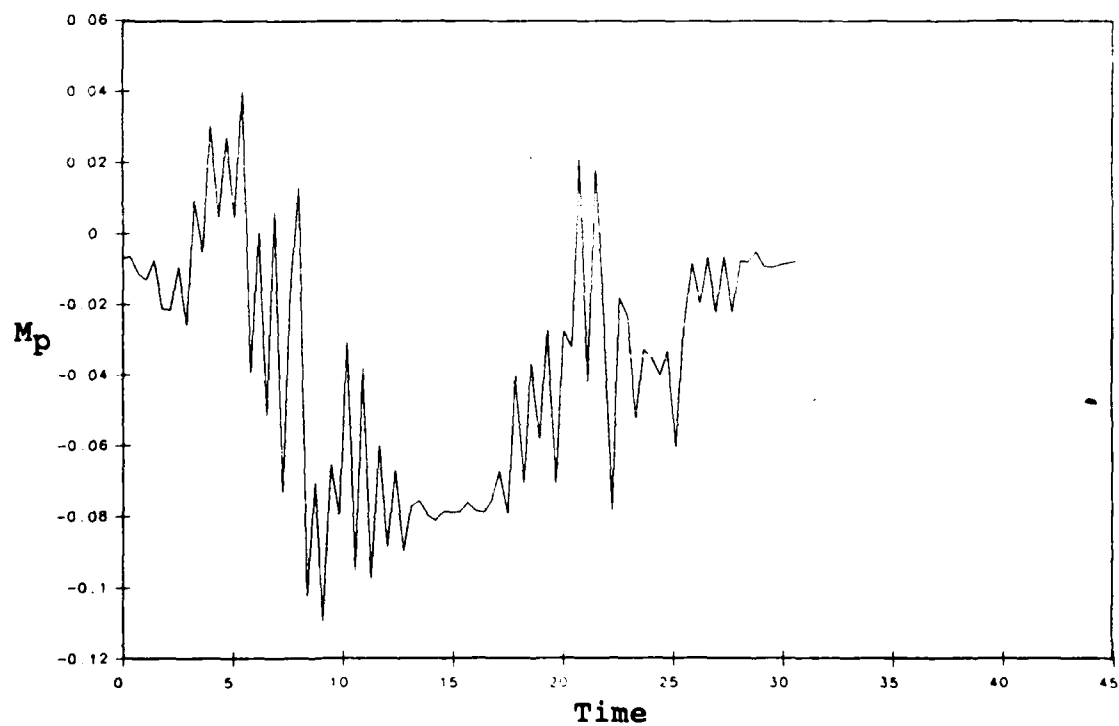


Fig. 6-19 Time History of Pitching Moment for a 28.7 sec Pitch/Pulse of the Straked Wing in the HFF for $V = 0$ FPS

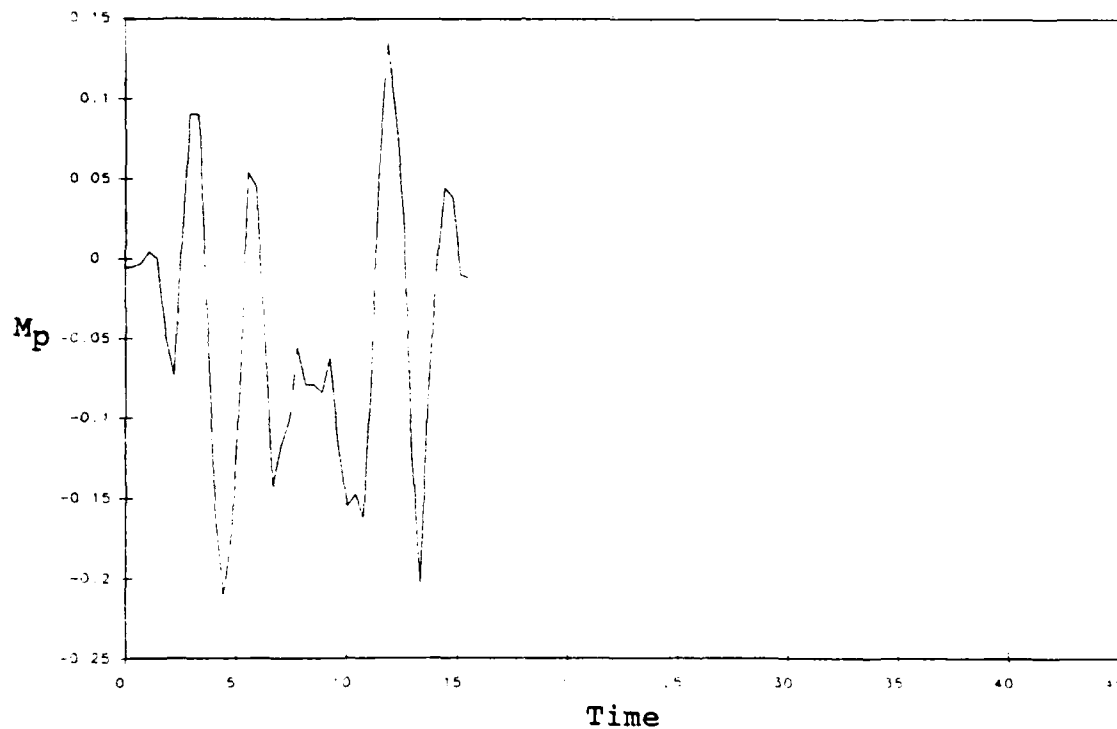


Fig. 6-20 Time History of Pitching Moment for a 15.3 sec Pitch/Pulse of the Straked Wing in the HFF for $V = 0$ FPS

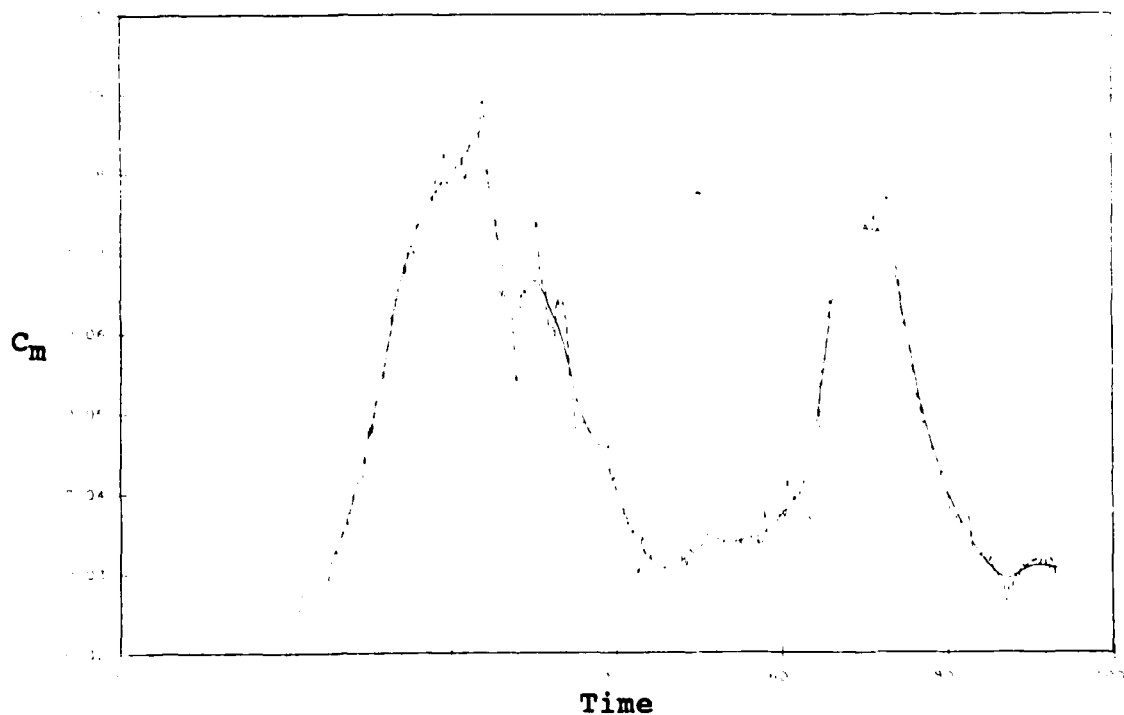


Fig. 6-21 Time History of C_m for an 87.7 sec Pitch/Pulse of the Straked Wing in the HFF for $V = 0.8$ FPS (Six Passes of the 0.25 Hz Low Pass Filter)

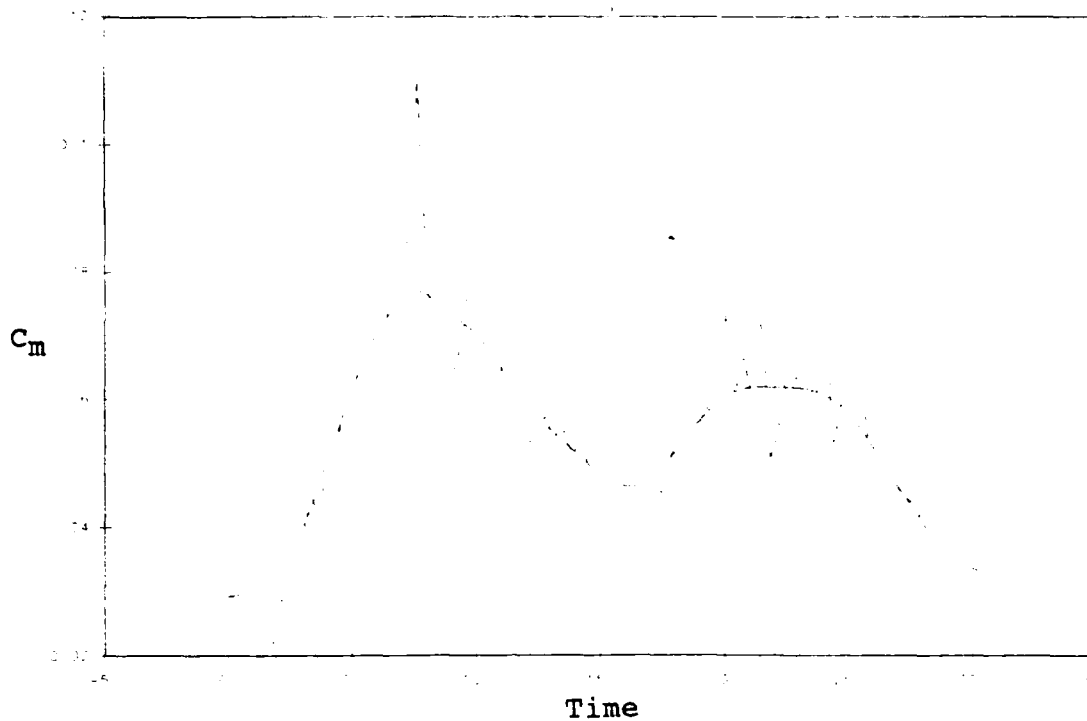


Fig. 6-22 Time History of C_m for a 30.0 sec Pitch/Pulse of the Straked Wing in the HFF for $V = 0.8$ FPS (Six Passes of the 0.25 Hz Low Pass Filter)

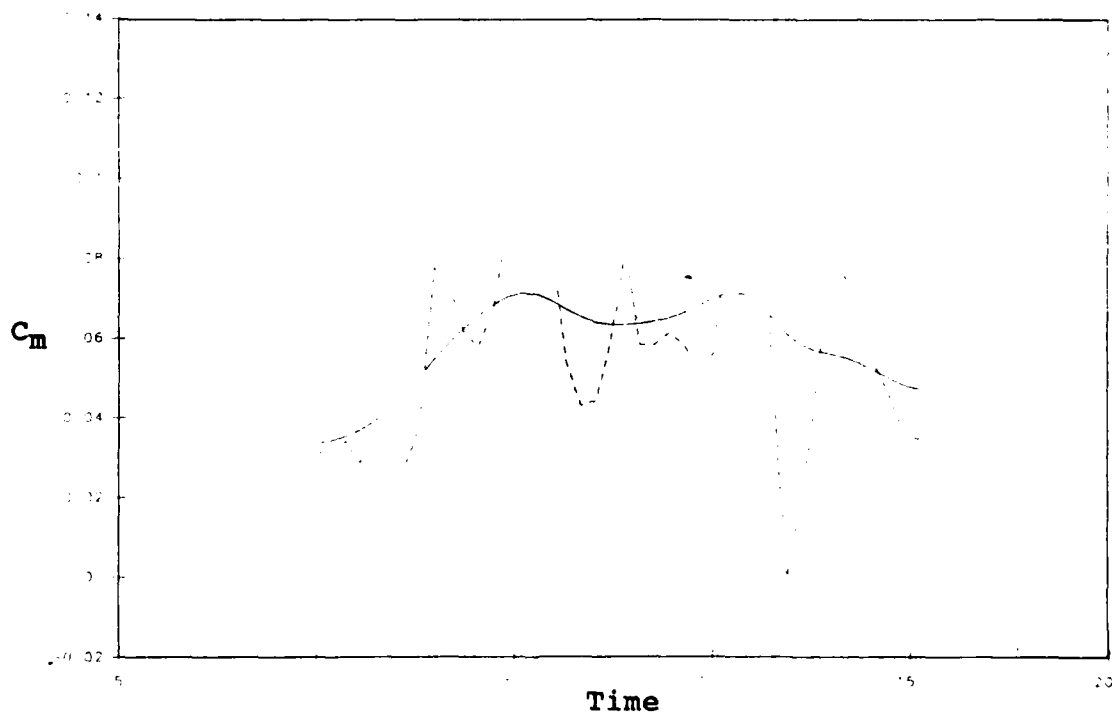


Fig. 6-23 Time History of C_m for a 16.7 sec Pitch/Pulse of the Straked Wing in the HFF for $V = 0.8$ FPS (Six Passes of the 0.25 Hz Low Pass Filter)

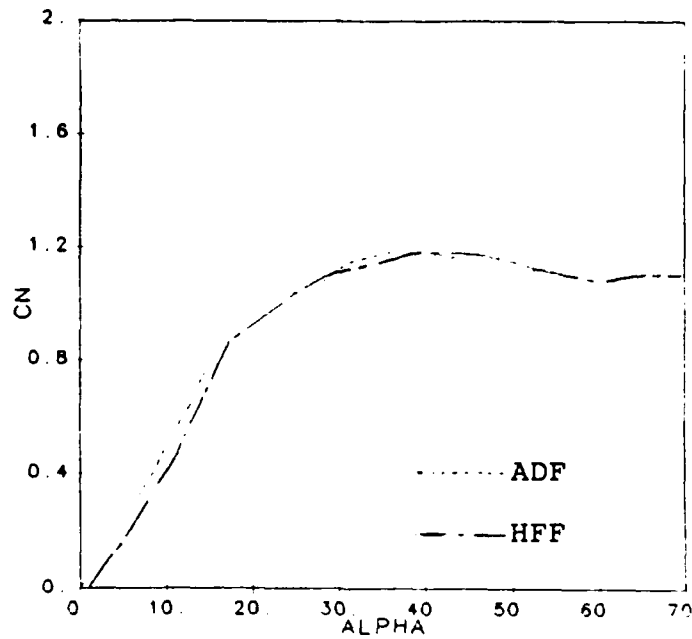


Fig. 6-24 Comparison of Steady ADF and HFF C_N Results for the Straked Wing

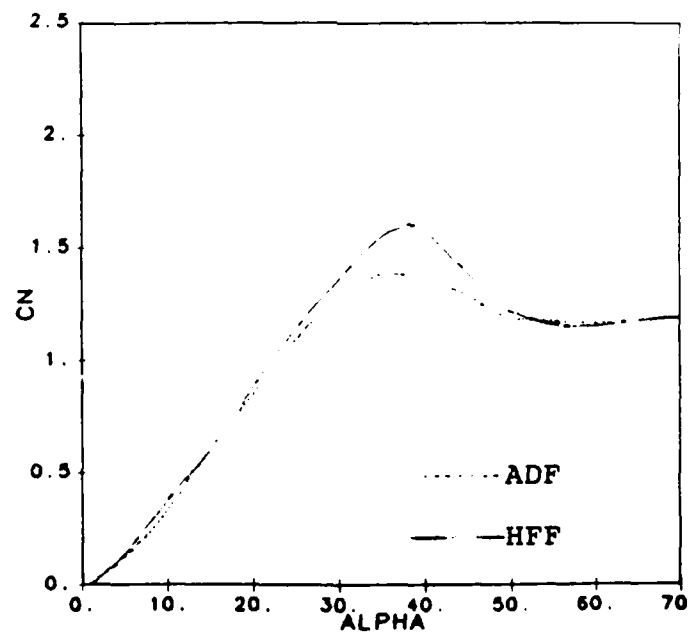
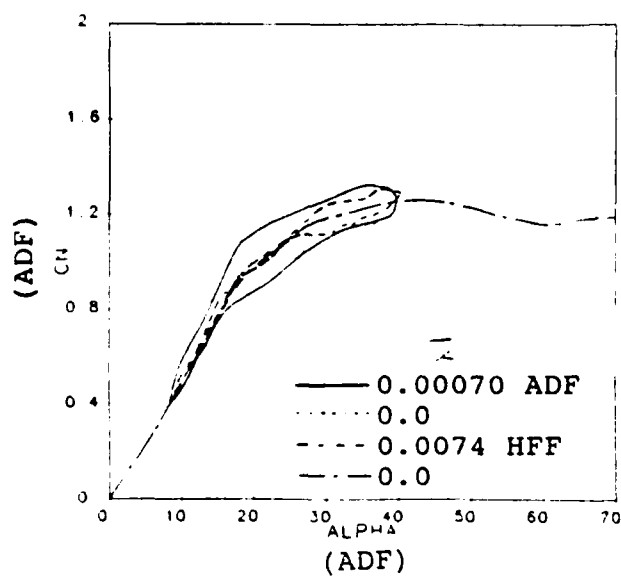
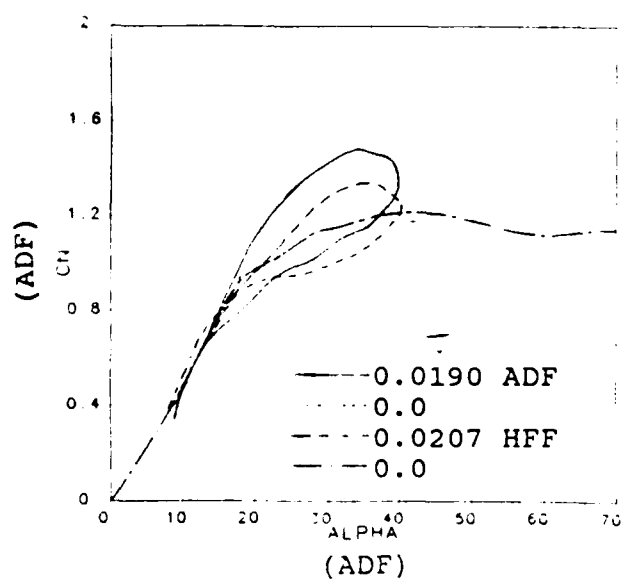


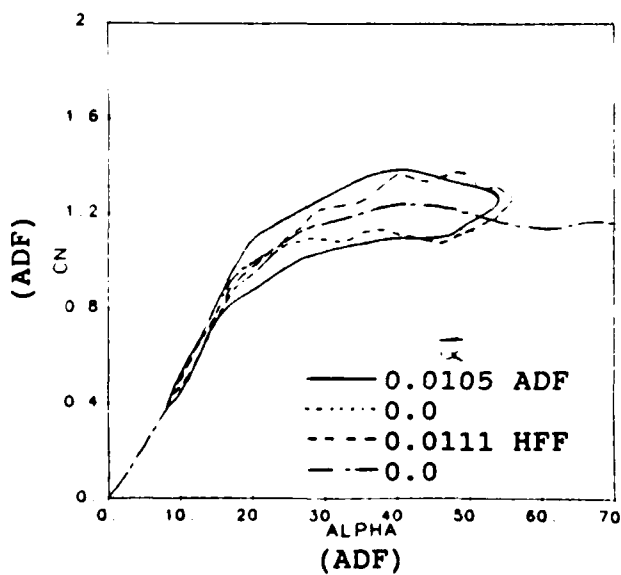
Fig. 6-25 Comparison of Steady ADF and HFF C_N Results for the 70°/30° Cranked Wing



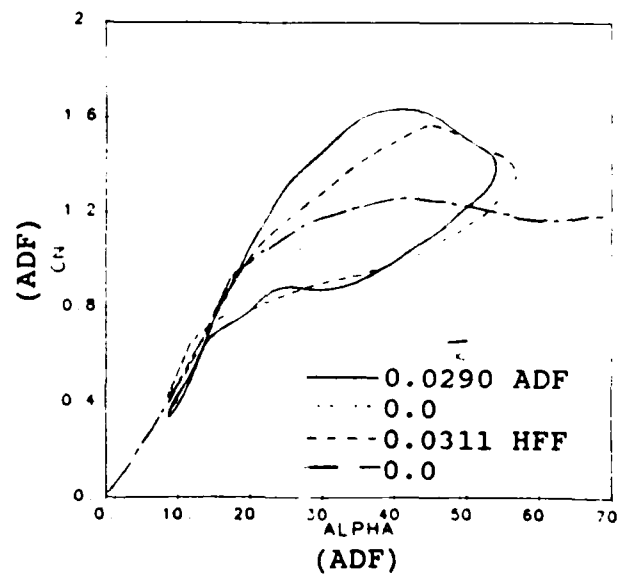
(a) Low Amplitude,
Low Frequency



(b) Low Amplitude,
High Frequency

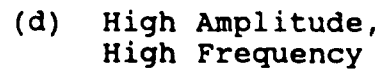
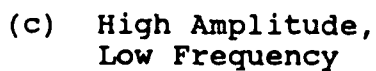
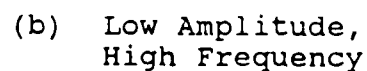
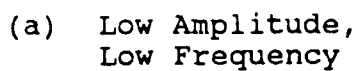


(c) High Amplitude,
Low Frequency

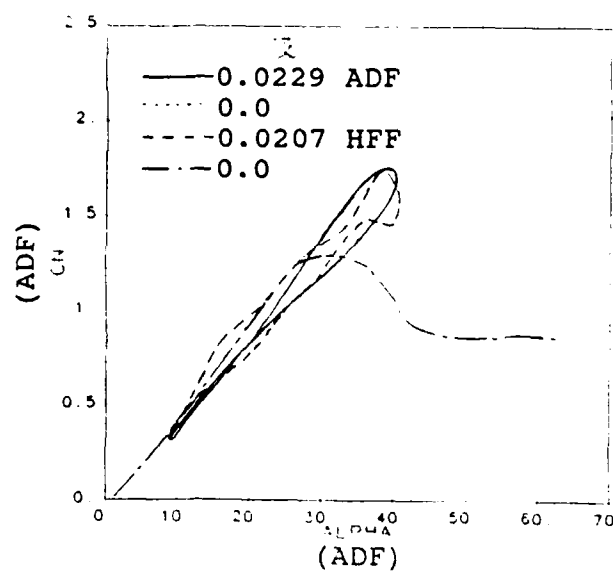


(d) High Amplitude,
High Frequency

Fig. 6-26 Comparison of ADF and HFF Results for the
Straked Wing at Two Amplitudes and Two Frequencies

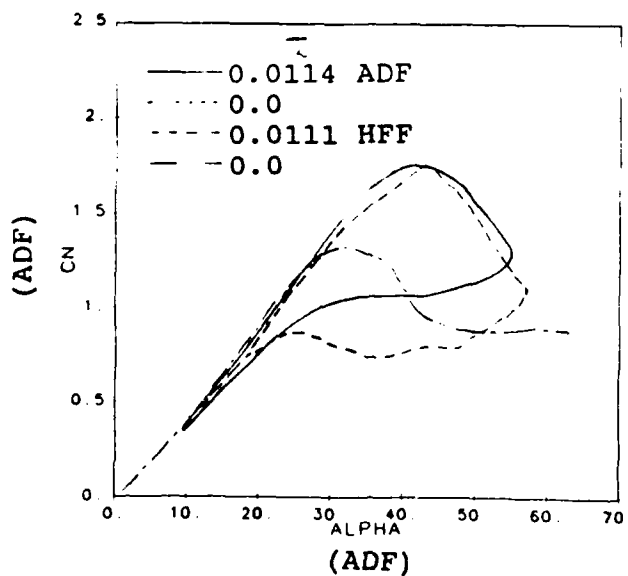


Data Not
Available for
ADF Run

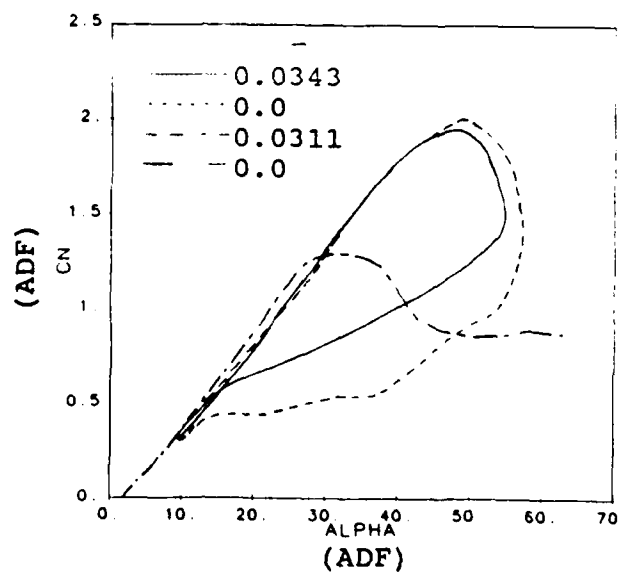


(a) Low Amplitude,
Low Frequency

(b) Low Amplitude,
High Frequency

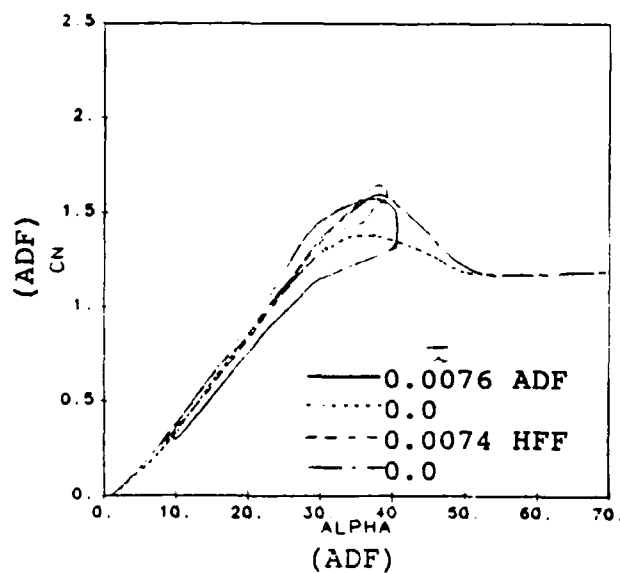


(c) High Amplitude,
Low Frequency

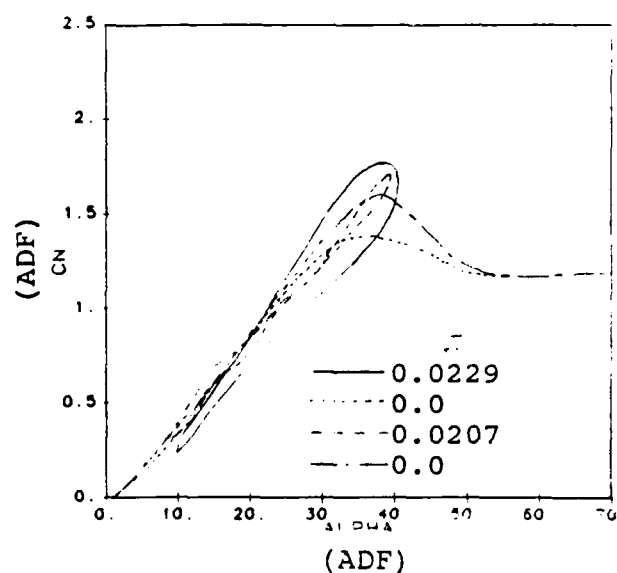


(d) High Amplitude,
High Frequency

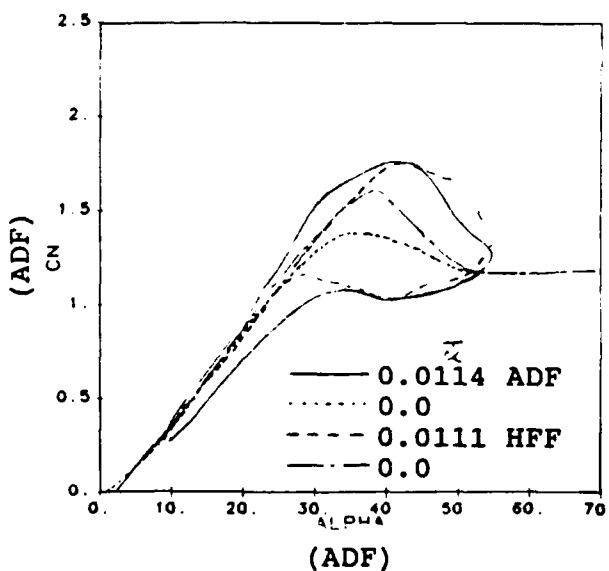
Fig. 6-28 Comparison of ADF and HFF Results for the
70° Delta Wing at Two Amplitudes and Two Frequencies



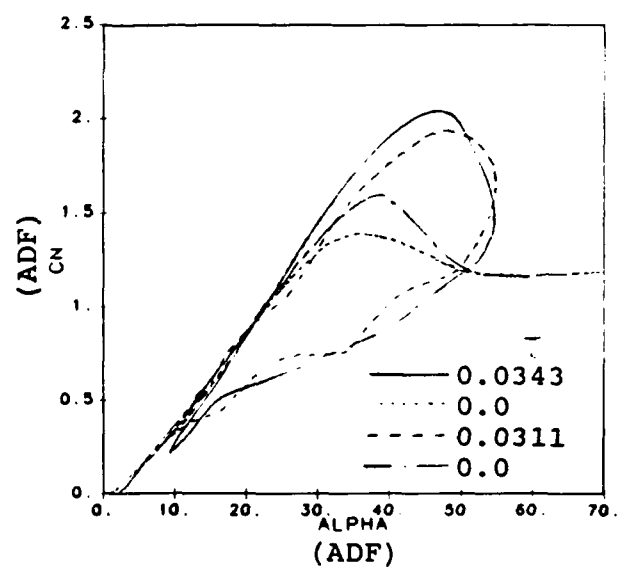
(a) Low Amplitude,
Low Frequency



(b) Low Amplitude,
High Frequency



(c) High Amplitude,
Low Frequency



(d) High Amplitude,
High Frequency

Fig. 6-29 Comparison of ADF and HFF Results for the 70°/30° Cranked Wing at Two Amplitudes and Two Frequencies

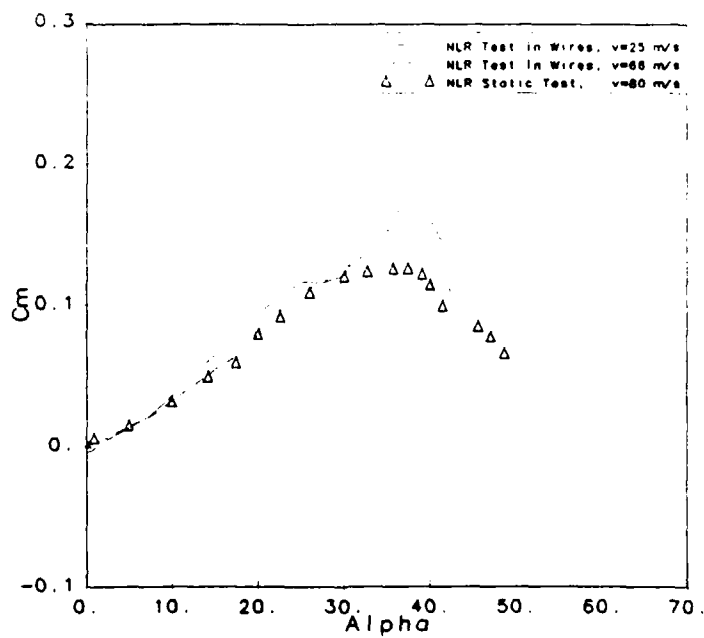
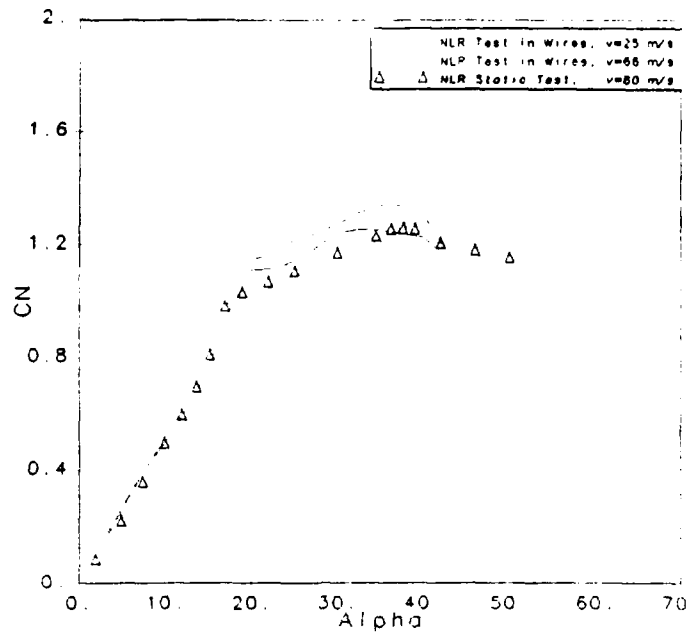


Fig. 6-30 Straked Wing Steady Results for NLR Test at Different Speeds and with Different Supports

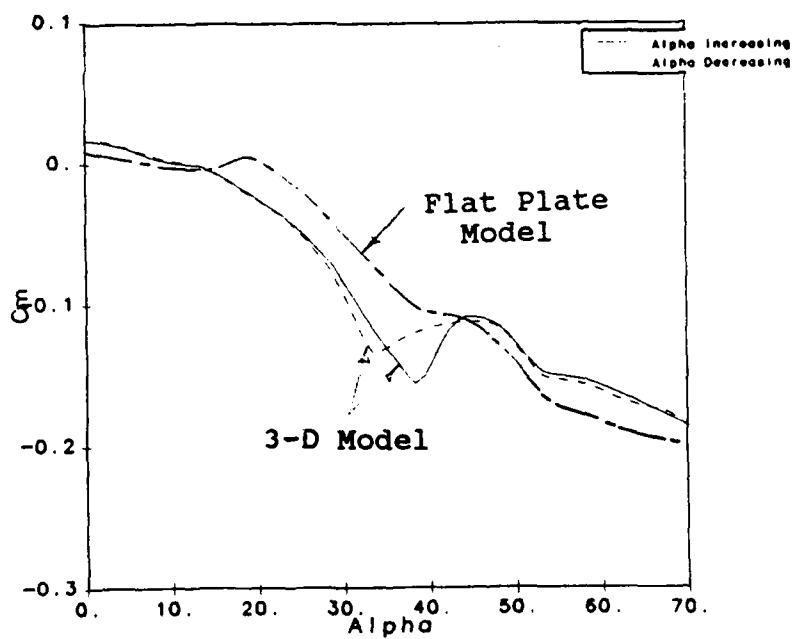
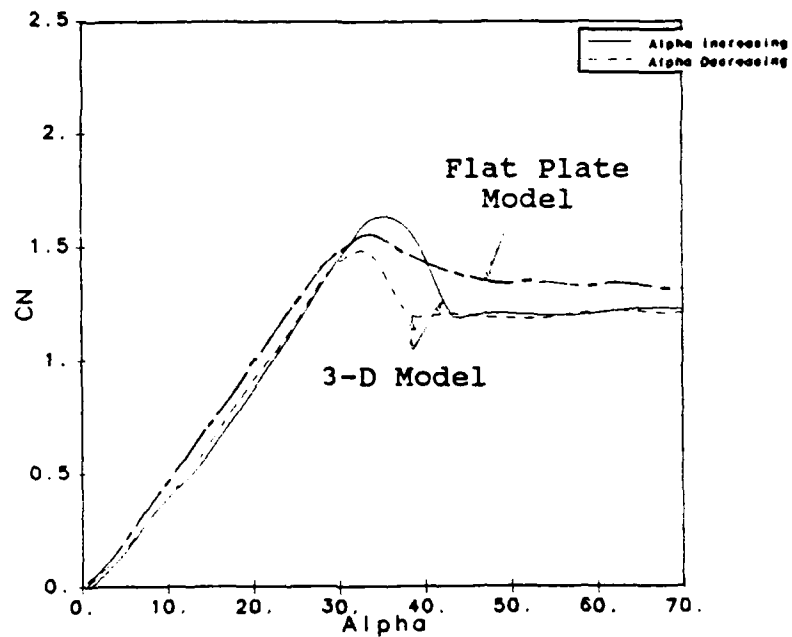


Fig. 6-31 Comparison of Steady HFF Results for the 3-D and Flat Plate E-7 Models

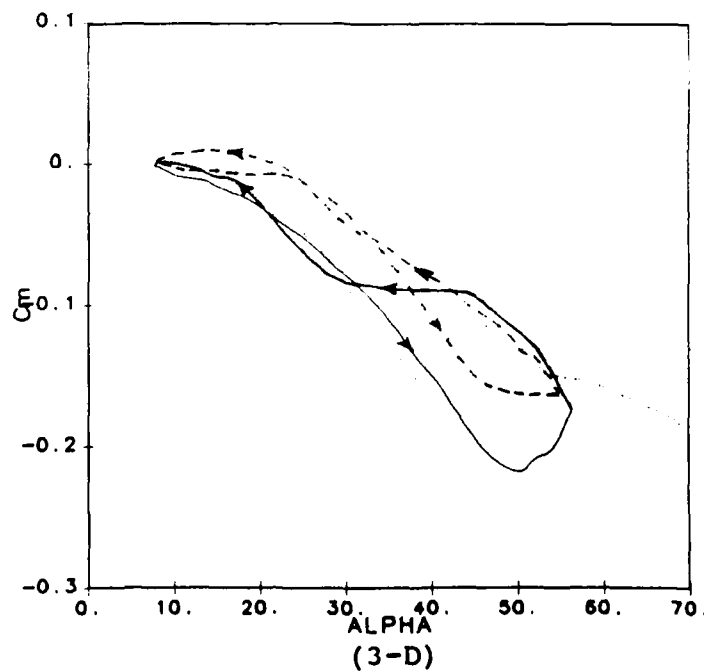
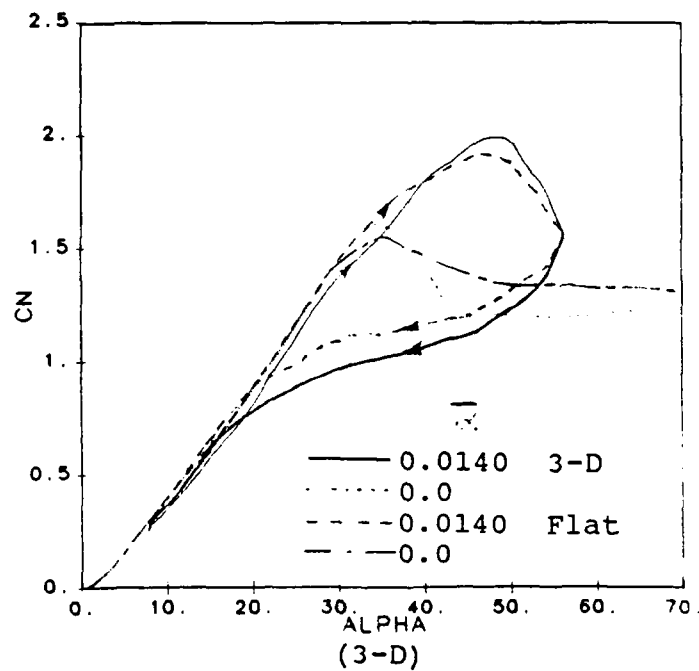


Fig. 6-32 Comparison of Unsteady HFF Results for the 3-D and Flat Plate E-7 Models, $k = 0.0333$ (Based on $C_r = 10.47''$)

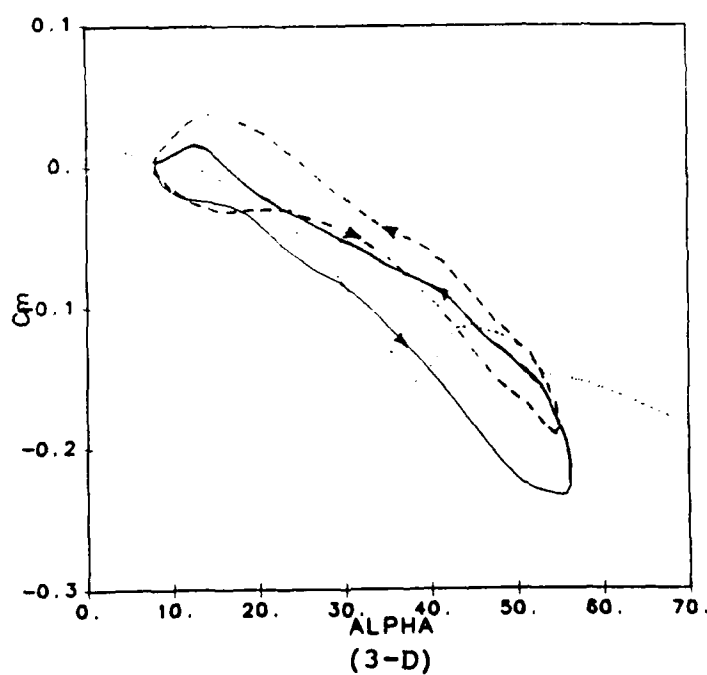
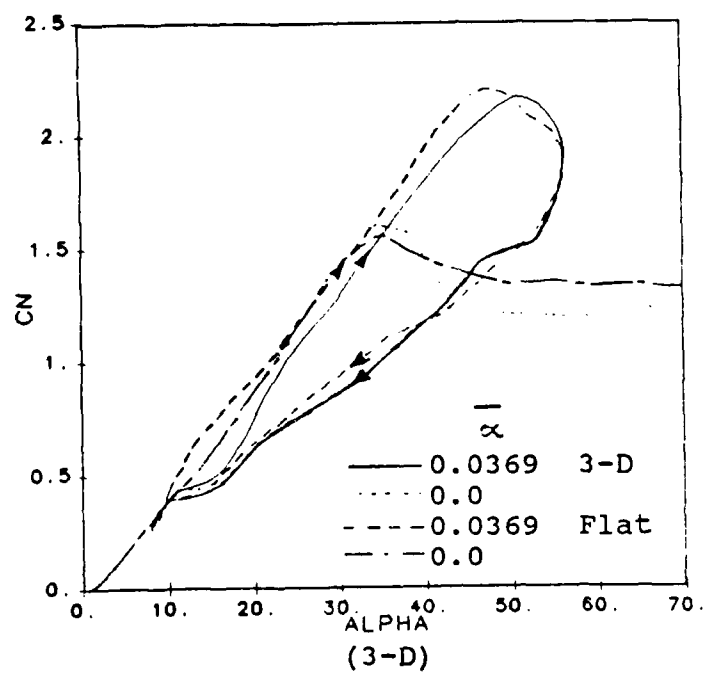
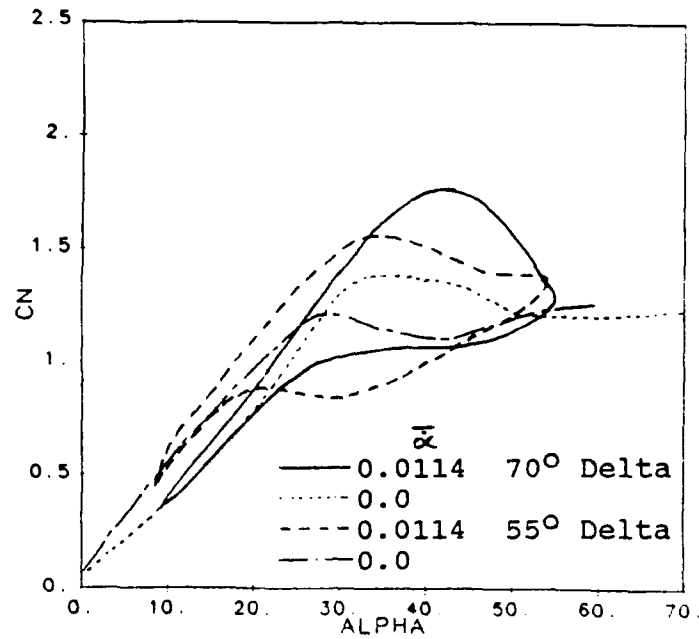
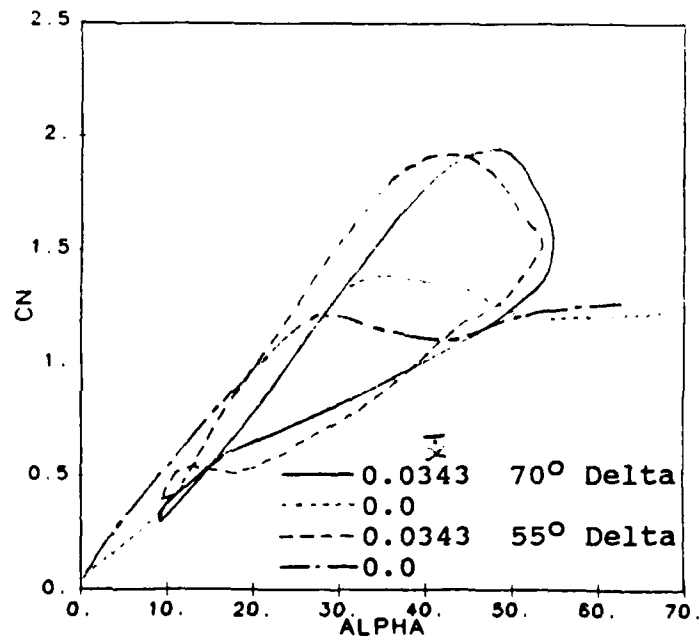


Fig. 6-33 Comparison of Unsteady HFF Results for the 3-D and Flat Plate E-7 Models, $k = 0.0882$ (Based on $C_r = 10.47''$)

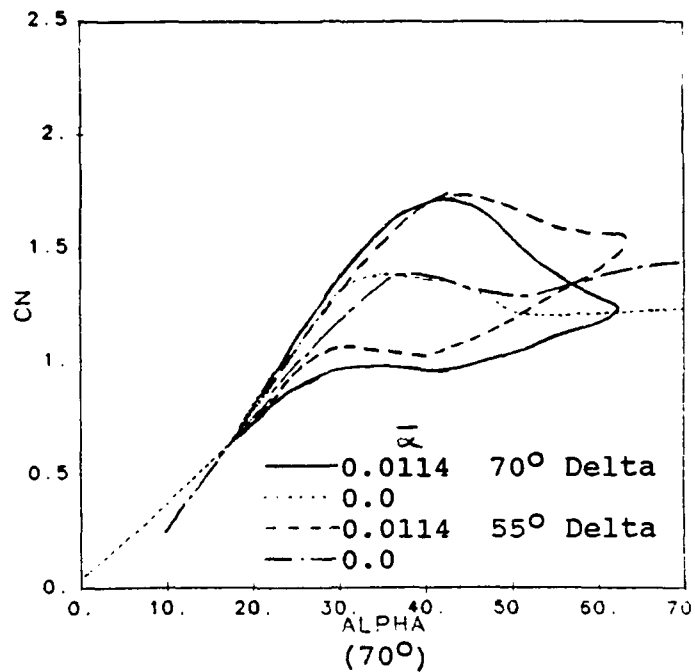


(a) Low Frequency

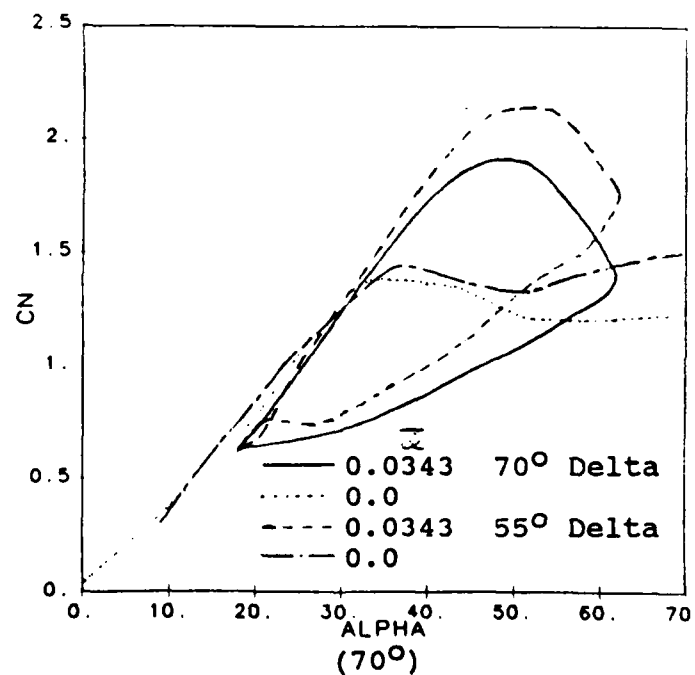


(b) High Frequency

Fig. 6-34 Comparison of Unsteady ADF Results for the 70° and 55° Delta Wings at Two Frequencies - Unshifted

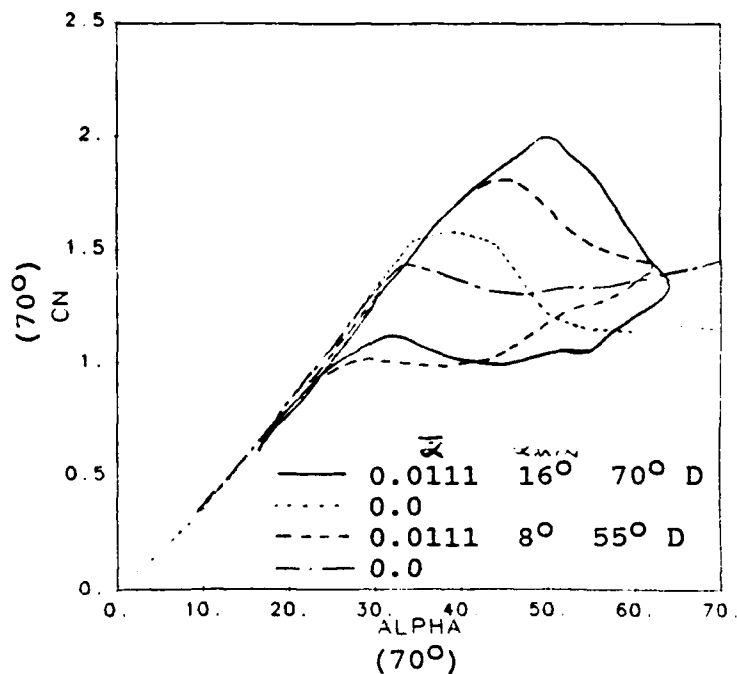


(a) Low Frequency

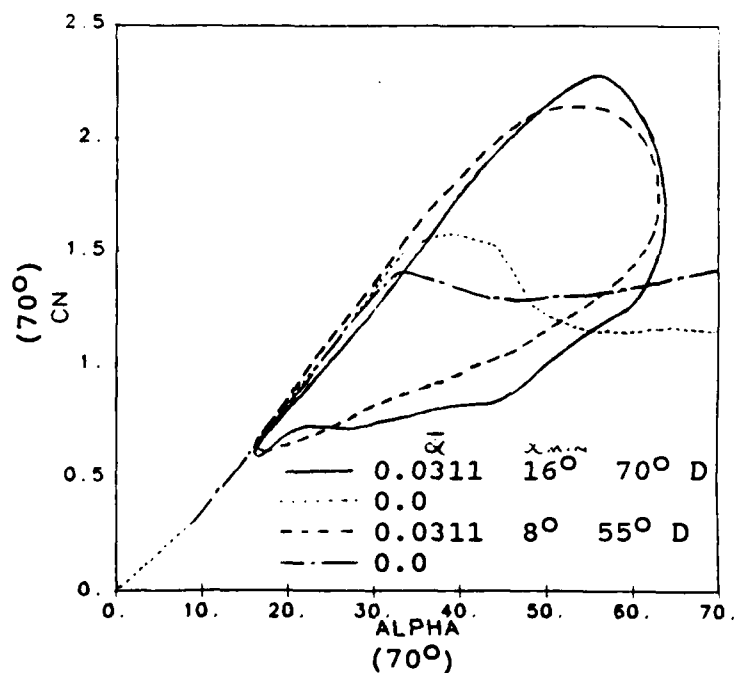


(b) High Frequency

Fig. 6-35 Comparison of Unsteady ADF Results for the 70° and 55° Delta Wings at Two Frequencies - Shifted ($\alpha_{\min} = 8^\circ$ for 55° Delta and $\alpha_{\min} = 16^\circ$ for the 70° Delta)

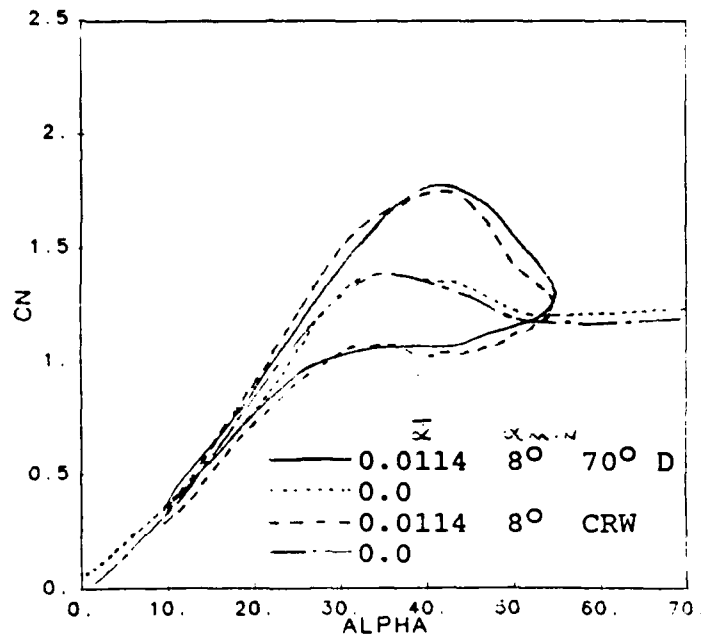


(a) Low Frequency

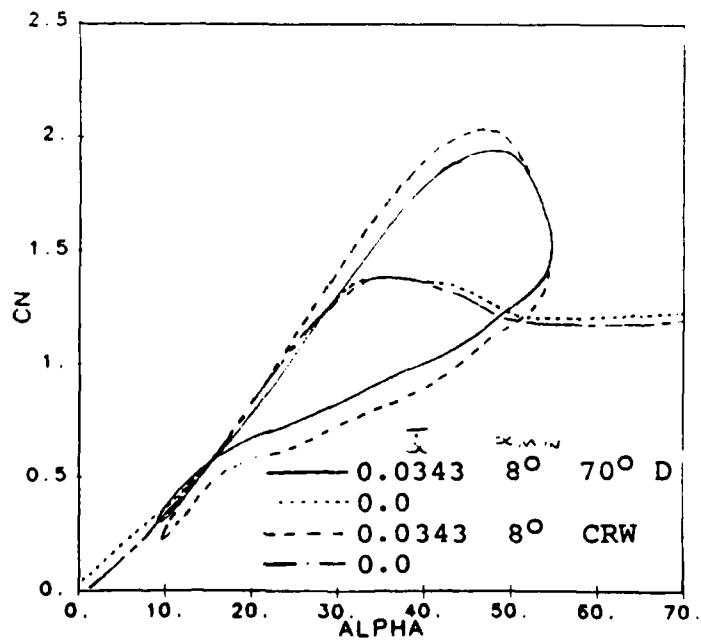


(b) High Frequency

Fig. 6-36 Comparison of Unsteady HFF Results for the 70° and 55° Delta Wings at Two Frequencies - Shifted ($\alpha_{min} = 8^\circ$ for 55° Delta and $\alpha_{min} = 16^\circ$ for 70° Delta)

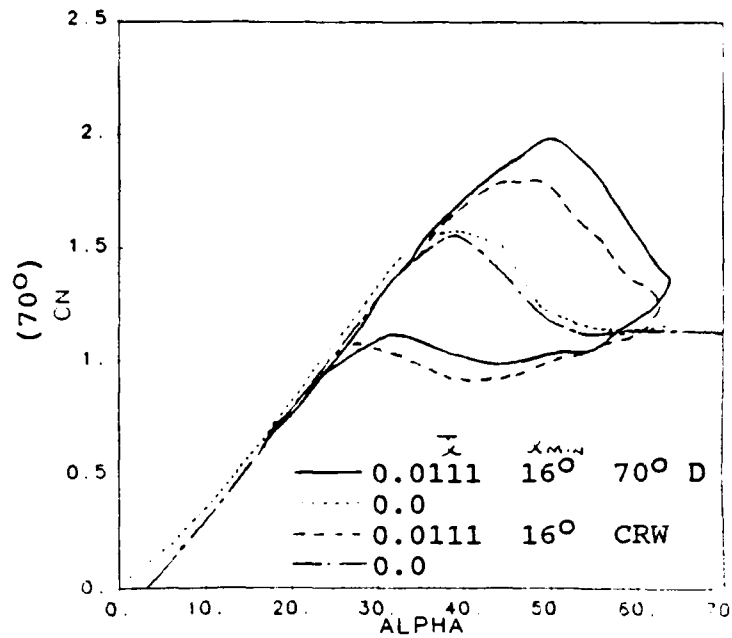


(a) Low Frequency

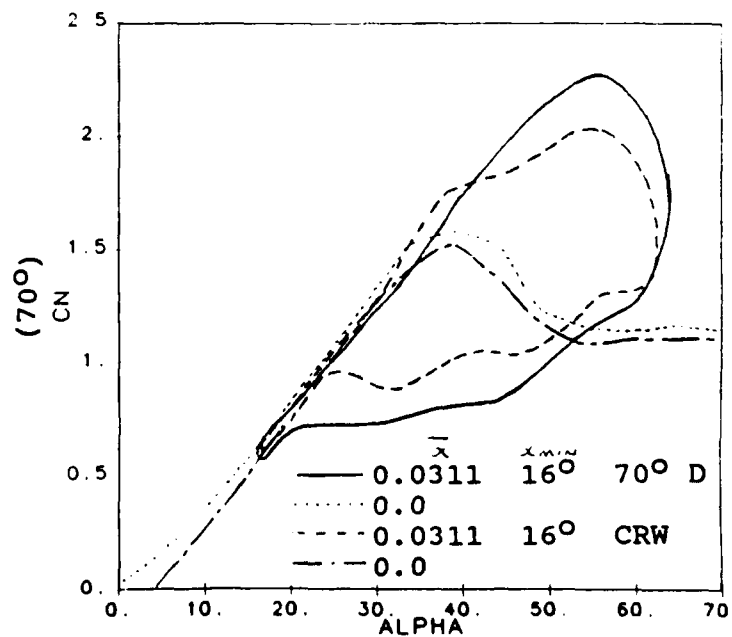


(b) High Frequency

Fig. 6-37 Comparison of Unsteady ADF Results for the 70° Delta and Cranked Wings at Two Frequencies - Unshifted ($\alpha_{\min} = 8^\circ$)



(a) Low Frequency



(b) High Frequency

Fig. 6-38 Comparison of Unsteady HFF Results for the 70° Delta and Cranked Wings at Two Frequencies - Unshifted ($\alpha_{min} = 16^\circ$) but Shifted in C_N

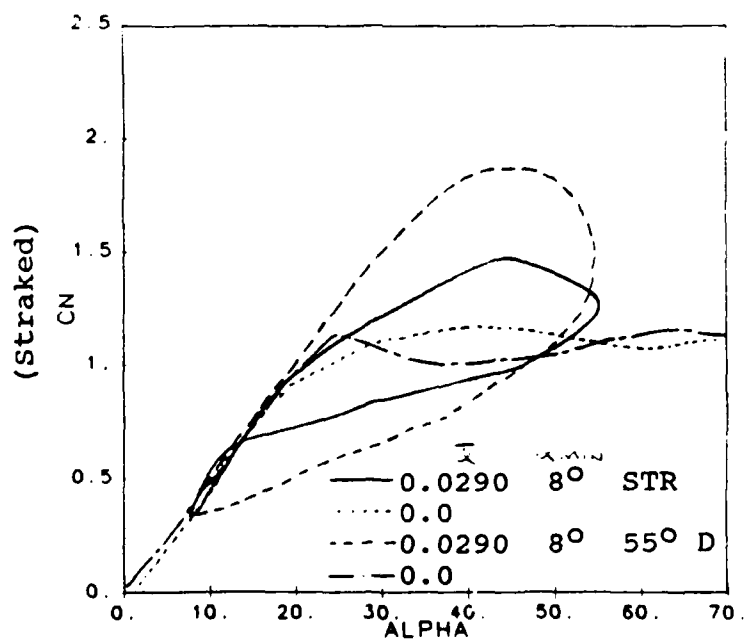
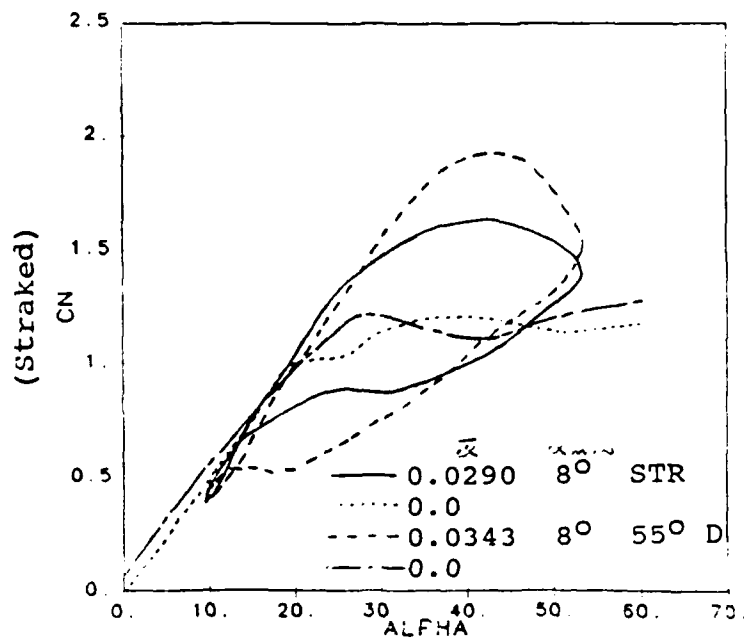
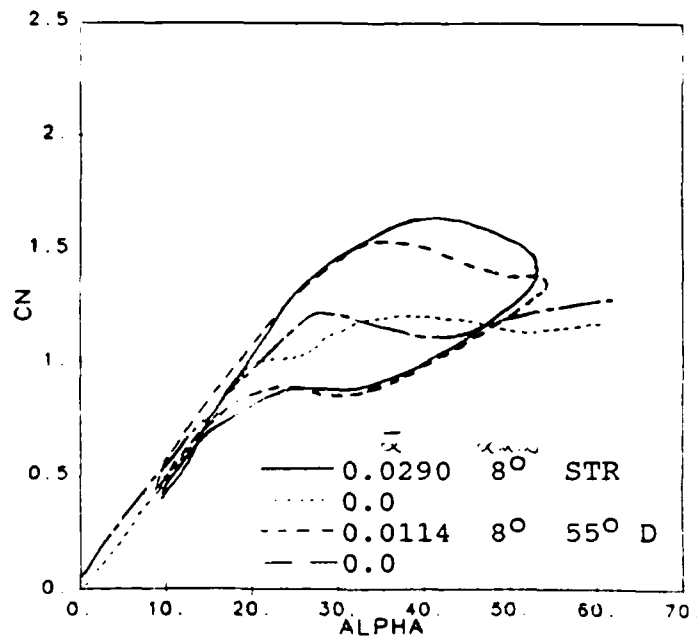
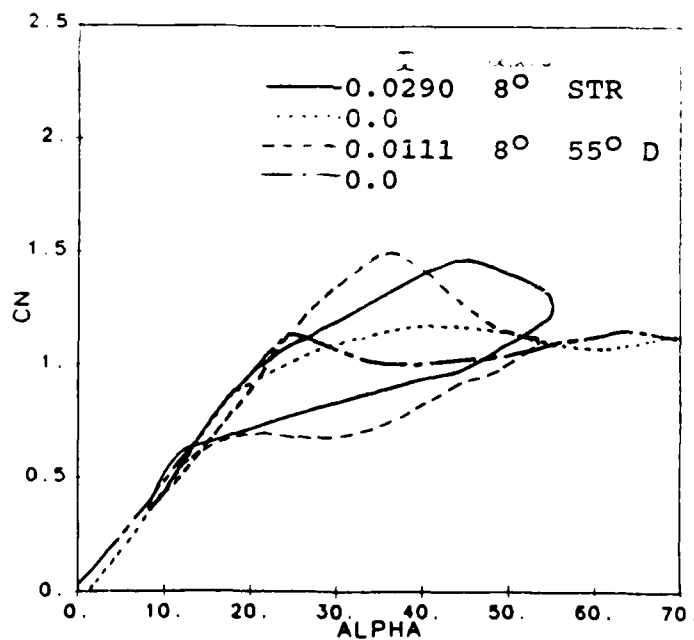


Fig. 6-39 Comparison of Unsteady ADF and HFF Results for the Straked and 55° Delta Wings at the High Frequency



(a) Mixed Frequencies, ADF Results



(b) Mixed Frequencies, HFF Results

Fig. 6-40 Comparison of Unsteady ADF and HFF Results for the Straked and 55° Delta Wings at Mixed Frequencies (Low Frequency for 55° Delta and High Frequency for Straked)

A P P E N D I X

WALL INTERFERENCE AND BLOCKAGE CORRECTIONS AT HIGH INCIDENCE AND BALANCE/SUPPORT INTERFERENCE EFFECTS IN THE WATER TUNNEL (excerpted from Ref. 6)

This appendix contains excerpted discussions from Ref. 6 in which two important aspects of water tunnel force testing were covered. The first covers the development of wall interference and blockage corrections that were applied at angles in excess of the value at which the wing totally stalled. The second covers the investigation to determine the effect of balance/support interference as a means of explaining certain discrepancies noted in pitching moment correlations.

A.1 Wall Interference and Blockage Corrections at High Alpha

Results for variation of the normal force coefficient, C_N , with incidence, α , for the large disk, small disk and three-dimensional E-7 model are shown in Figures A-1, A-2 and A-3 respectively. These data were obtained with the "constant q_0 " technique (described in Section 3.7) and are otherwise uncorrected. Shown also in Figure A-1 are the C_N results extracted from Hoerner (Ref. 9, p. 3-16) as denoted by the symbols. Up to maximum C_N , the agreement is excellent which verifies the concept just described for angles below that of total flow separation. Beyond that point, which is about 40° , the force falls abruptly in agreement with Ref. 9 but begins to diverge with increasing α . For decreasing α , starting at 90° , the static hysteresis is observed which is also in agreement with Ref. 9.

Results for the small disk shown in Figure A-2, are below the data of Ref. 9 up to total flow separation at 40° . Beyond that point, after the abrupt decrease between 38° and 43° , a less pronounced but similar diverging tendency is seen as was observed with the large disk. Likewise C_N results for the 3-D E-7 model are shown in Figure A-3. With exception of a lower value of maximum C_N , which is attributed to Reynolds Number effects, the trends are almost identical to those for the large disk. As is suggested by these comparisons, it is convenient to separately discuss the trends over the low alpha range from 0° to total flow separation, α_{ts} , and the high alpha range from α_{ts} to 90° .

The low alpha range is characterized by well ordered flows over the model with wake cross-sectional areas that are significantly less than that of the model planform area. This holds true even within the range of burst vortex flow since the

free stream is still being deflected as indicated by increasing C_N with increasing α . Model planform area to test section area ratios, A_{mt} , are 0.0994, 0.0668 and 0.1042 for the large disk, small disk are 3-D E-7 model respectively. (Total projected area, including the nose and nozzle, was used for the 3-D E-7 model.) Since the A_{mt} values for the large disk and 3-D E-7 models are near 10% and the small disk is 6.7%, the difference in trends between water tunnel data and calibrating data could be attributed to an area effect. However, the low values of C_N for the small disk are believed to be caused by balance/support interference on the smaller model which is less significant on the larger models.

Comparing C_N for the large and small disks at 0° , it is seen that the former shows $C_N = 0$ as it should be for a flat plate where as the latter shows $C_N = -0.02$. The negative lift at 0° is attributed to the negative camber effect produced by the balance and support mounted on the model lower surface. At higher angles, upstream blockage produced by the support struts increases, thereby lowering pressures on the lower surface and reducing C_N . These effects are diminished on models of higher aspect ratio as well as larger size. They are also evident in pitching moment at $\alpha \approx 0^\circ$ as will be discussed later.

The high alpha range is characterized by chaotic wake flows typical of a perpendicular flat plate. The constant value of C_N for $\alpha > \alpha_{ts}$ as shown by the data from Ref.'s 9 and 10 (Figs. A-1 and A-3), is indicative of a flow field structure relative to the model that does not change with incidence. The divergence of C_N shown by the water tunnel data is therefore attributed to an increased blockage created by a significant expansion of the wake that occurs with total flow separation at α_{ts} . The wake blockage effect would be expected to be a function of the model area parameter, A_{mt} , as is verified by the small and large disk results in Figures A-1 and A-2. Due to the magnitude of this effect, a correction was developed for application at angles larger than α_{ts} .

The normal force coefficient at 90° incidence for flat plates of aspect ratio of 3.5 or less is constant at 1.17 as shown by Hoerner (Ref. 9, p. 3-16). This convenient piece of information was used to develop a correction technique for the water tunnel forces at $\alpha = 90^\circ$ which was extended down to α_{ts} through a simple geometric relation. C_N vs α was measured for four other models which included the straked wing model, two delta wings of 55° and 70° sweep, and a cranked wing with $70^\circ/30^\circ$ inboard/outboard sweeps. All of these models had aspect ratios of less than 3.5, hence all should exhibit a C_N of 1.17 at $\alpha = 90^\circ$ and any deviation would be attributed to the wake blockage effect.

The results of the correlations for the eight models at $\alpha = 90^\circ$ are summarized in Table A-1. In addition, the ratio of C_{N90° for the HFF test to the ideal value or, in the case of the 3-D E-7 model, the value from a large scale test at $\alpha = 90^\circ$, is shown plotted vs A_{mt} in Figure A-4 for the eight models. A correlative parameter, C_w , was developed on the basis of a wake expansion factor that would account for the flow acceleration produced by the wake blockage. It was assumed that the higher velocity in the vicinity of the model due to wake expansion, V_w , could be calculated as

$$V_w = V_c \left(\frac{A_t}{A_t - C_w A_m} \right) = \frac{V_o}{1 - C_w A_{mt}} \quad (A-1)$$

where V_o was the upstream undisturbed velocity, A_m the model planform area and A_t the test section area. (In the case of these correlations, V_o was taken to be the value for the model at zero incidence and assumed constant in order to be consistent with the "constant q_o " technique.) The C_w parameter is analogous to the contraction coefficient as defined for flows through an orifice plate.

The relationship between C_N and C_w was established through q such that

$$q_w = \frac{\rho V_w^2}{2} = \frac{\rho}{2} \left(\frac{V_o}{1 - C_w A_{mt}} \right)^2 = \frac{q_o}{(1 - C_w A_{mt})^2} \quad (A-2)$$

which leads to

$$(C_{N90^\circ})_{corr} = (C_{N90^\circ})_{unc} \frac{q_o}{q_w} = (C_{N90^\circ})_{unc} (1 - C_w A_{mt})^2 \quad (A-3)$$

Equation A-3 represents the final correction for C_N as measured in the water tunnel at $\alpha = 90^\circ$. Thus, for exact correlation of the HFF test data shown in Table A-1 with the referenced data, the ideal value of C_w , denoted as C_w^* , can be obtained from

$$\frac{1}{(1 - C_w^* A_{mt})^2} = \frac{(C_{N90^\circ})_{HFF}}{(C_{N90^\circ})_{REF}}$$

or

$$C_w^* = \frac{1}{A_{mt}} \left[1 - \sqrt{\frac{(C_{N90^\circ})_{REF}}{(C_{N90^\circ})_{HFF}}} \right]$$

This value of C_w^* is also included in Table A-1 for each model and, as can be seen, ranges from a low of 1.18 for the small disk

to 1.77 for the flat E-7 model. The average value is 1.52, however, if the small disk is eliminated since it has some questionable support interference, the average value is 1.57. This latter value correlates exactly with the 3-D E-7 model in which the highest confidence is held, and it correlates well with four other models.

The line shown in Figure A-4 was calculated with $C_w = 1.57$ as

$$\frac{(C_{N90^\circ})_{HFF}}{(C_{N90^\circ})_{REF}} = \frac{1}{(1 - 1.57 A_{mt})^2}$$

which correlates well with most of the data. Therefore $C_w = 1.57$ was chosen as the value to be used to correct all water tunnel normal force data for angles greater than α_{ts} . Corrections to pitching moment data were also accomplished with the same equations assuming that the wake blockage had negligible effect on the center of pressure.

The next step was to determine the appropriate variation of the correction function between α_{ts} and 90° . Examination of the data in Figures A-1, A-2 and A-3 indicated that the function varied from 1.0 at α_{ts} to the value at 90° in a parabolic manner. In fact, it was determined that the variation could be well represented by a sine curve such that

$$(C_N)_{corr} = (C_N)_{unc} (1 - C_w A_{mt} \sin \alpha')^2, \alpha \geq \alpha_{ts} \quad (A-4a)$$

where

$$\alpha' = 90^\circ \left(\frac{\alpha - \alpha_{ts}}{90^\circ - \alpha_{ts}} \right) \quad (A-4b)$$

Equations A-4 are the final form for blockage corrections that were applied to water tunnel force and moment data for $\alpha_{ts} \leq \alpha \leq 90^\circ$.

A.2 Balance/Support Interference Effects

The effects of balance/support interference on pitching moment at low angles were identified by comparing C_{mo} values at $\alpha = 0^\circ$ for the flat plate models. Since C_{mo} should be exactly zero for these models, the measured increment, ΔC_{mo} , represents the summation of pitching moment due to (1) the balance "bump" on the bottom surface of the wing, (2) support interference and (3)

the displacement of flat plate drag, C_{d0} , above the pitch axis. In equation form this relationship becomes

$$\Delta C_{M0} = \Delta C_{Mob} + \Delta C_{Mos} + \frac{C_{d0} Z}{C_r} \quad (A-5)$$

where

ΔC_{Mob} = Pitching moment coefficient due to the balance "bump" or camber

ΔC_{Mos} = Pitching moment coefficient due to support interference

Z = Displacement of the flat plate wing mean plane above the balance reference axis

C_r = Reference length for non-dimensionalizing the pitching moment.

Defining

$$\begin{aligned} \Delta M_{ob} &= (q_0 A_m C_r) \Delta C_{Mob} \\ \Delta M_{os} &= (q_0 A_m C_r) \Delta C_{Mos} \end{aligned}$$

Equation 5 becomes

$$\Delta C_{M0} = \frac{1}{A_m C_r} \left[\frac{\Delta M_{ob}}{q_0} + \frac{\Delta M_{os}}{q_0} \right] + \frac{C_{d0} Z}{C_r} \quad (A-6)$$

Although C_{d0} was not measured, its effect was small and assuming its value to be 0.015 was sufficiently accurate for this investigation. Thus, the sum of ΔM_{ob} and ΔM_{os} could be estimated from the measured values of ΔC_{M0} for the various models with Equation A-6 rewritten as

$$\frac{\Delta M_{ob/s}}{q_0} = \left[\frac{\Delta M_{ob}}{q_0} + \frac{\Delta M_{os}}{q_0} \right] = A_m C_r \left[\Delta C_{M0} - \frac{0.015 Z}{C_r} \right] \quad (A-7)$$

The ΔC_{M0} , geometric data and resulting $\Delta M_{ob/s}/q_0$ values are shown in Table A-2 for all seven of the flat plate models. Assuming that the absolute value of pitching moment is independent of the flat plate model planform geometry, the values of $\Delta M_{ob/s}/q_0$ should be the same for all models. With exception of the 70° delta model, all values fell within a relatively narrow range of 2.96 to 3.64 as shown in the table. The fact

that the straked wing, 55° delta and cranked wing all fell within a very close range of 2.96 to 3.06 is encouraging as to the repeatability of the phenomenon. Planform geometry effects were suggested on the basis of the closeness of the large and small disk values, even though the small disk had an area similar to the straked wing and 55° delta wing. Also, the E-7 flat plate model which had almost the same area as the large disk but a planform more related to the straked wing and 55° delta, was an interesting example. In this case, its value of $\Delta M_{ob}/s/q_0 = 3.37$ was almost halfway between those of the large disk at 3.64 and the straked wing at 3.06.

The above results established the primary source of pitching moment errors for the flat plate models at $\alpha = 0^\circ$ in the water tunnel, as the interference produced by the balance and support system attached to the model lower surface. The consistent story implied that a correction could be established, however, problems were encountered as alpha was changed from zero. The ΔC_{mo} tended to disappear at higher angles beyond the linear attached flow region and became entangled with apparent Reynolds Number effects. At angles beyond α_{ts} , the pitching moment increment was essentially zero and the effects of balance/support interference seemed to be felt more in the normal force. Therefore no correction was established for this interference although its presence has been acknowledged.

TABLE A-1 Results for Normal Force
Correlations at $\alpha = 90^\circ$ ($V_0 \approx 0.8$ FPS)

Model	(in ²) Area	AR	Amt	HFF (C _{N90o})HFF	REF (C _{N90o})REF	Ratio	C _w [*]
Large Disk	57.28	1.281	0.0994	1.66	1.17	1.419	1.61
Small Disk	38.48	1.281	0.0668	1.38	1.17	1.179	1.18
3-D E-7	57.22	1.665	0.0993	1.70	1.21	1.405	1.57
Flat E-7	60.00	1.588	0.1042	1.76	1.17	1.502	1.77
Straked Wing	33.17	2.490	0.0576	1.40	1.17	1.197	1.49
55° Delta	34.41	2.810	0.0597	1.44	1.17	1.231	1.65
70° Delta	29.48	1.455	0.0512	1.34	1.17	1.145	1.29
Cranked Wing	31.76	1.715	0.0551	1.41	1.17	1.205	1.62

TABLE A-2 Pitching Moment Effects Due
to Balance/Support Interference

Model	Area (in ²) A_m	Ref.L. (in) C_R	Bal.Disp. (in) Δz	ΔC_{M_0}	(in#/q) $M_{OB}/S/q$
Large Disk	57.28	8.54	0.315	0.008	3.64
Small Disk	38.48	7.02	0.315	0.014	3.60
Flat E-7	57.22	7.10	0.325	0.009	3.37
Straked Wing	33.17	8.85	0.330	0.011	3.06
55° Delta	34.41	7.00	0.325	0.013	2.96
70° Delta	29.48	9.00	0.325	0.009	2.24
Cranked Wing	31.76	9.00	0.325	0.011	2.99

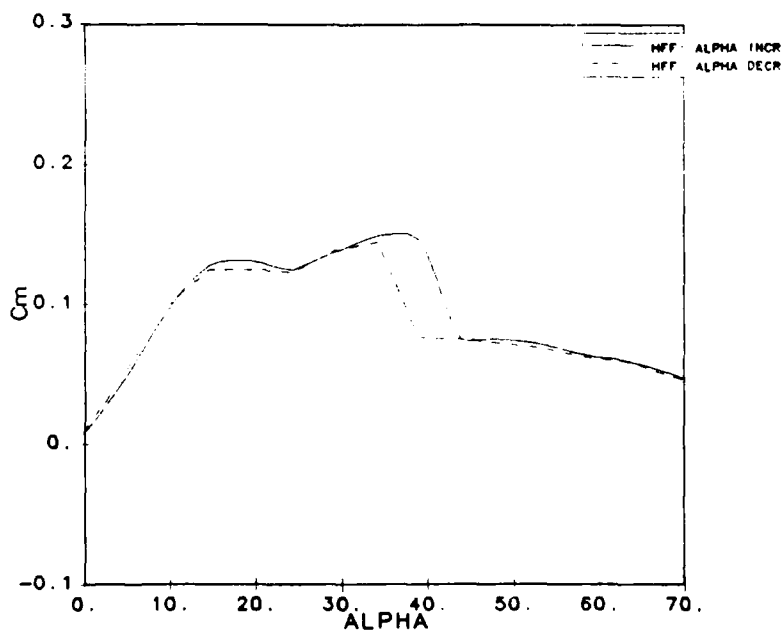
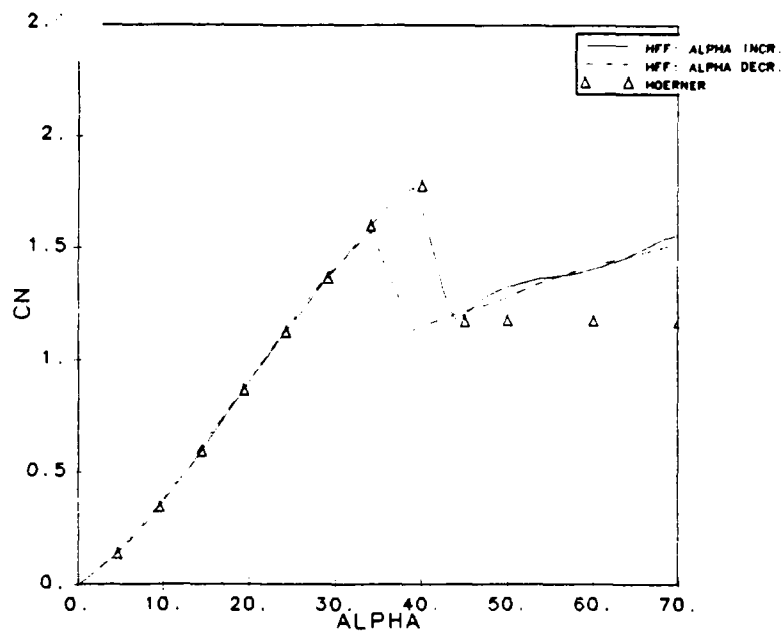


Fig. A-1 Uncorrected HFF Results for the Large Disk as Compared with Hoerner (Ref. 9)

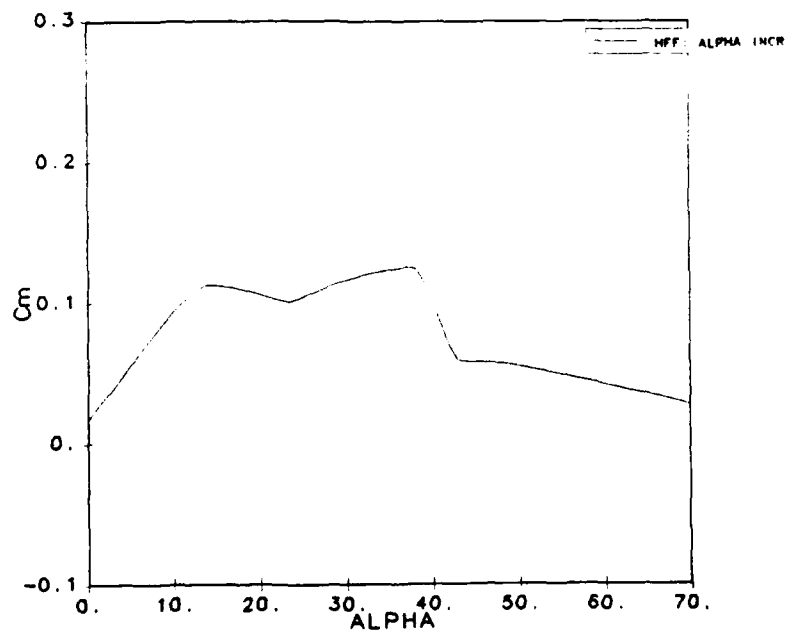
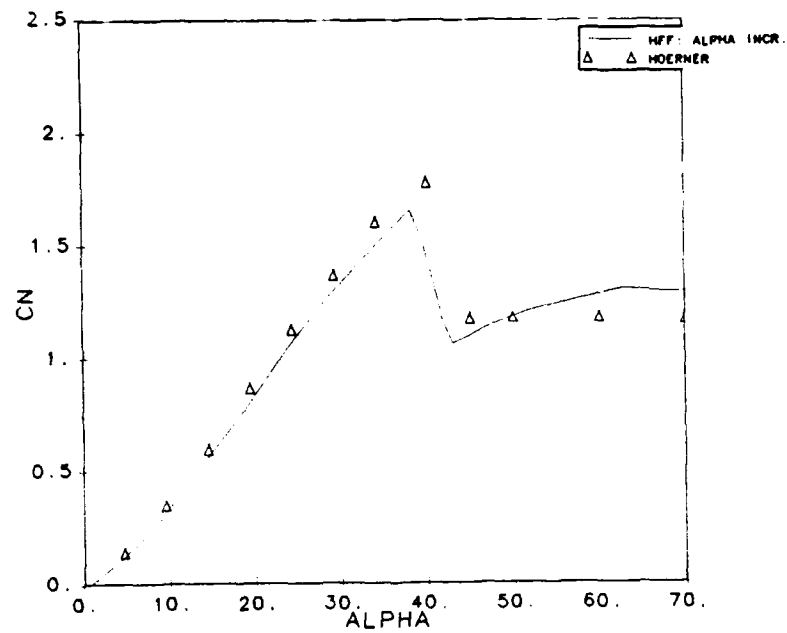


Fig. A-2 Uncorrected HFF Results for the Small Disk as Compared with Hoerner (Ref. 9)

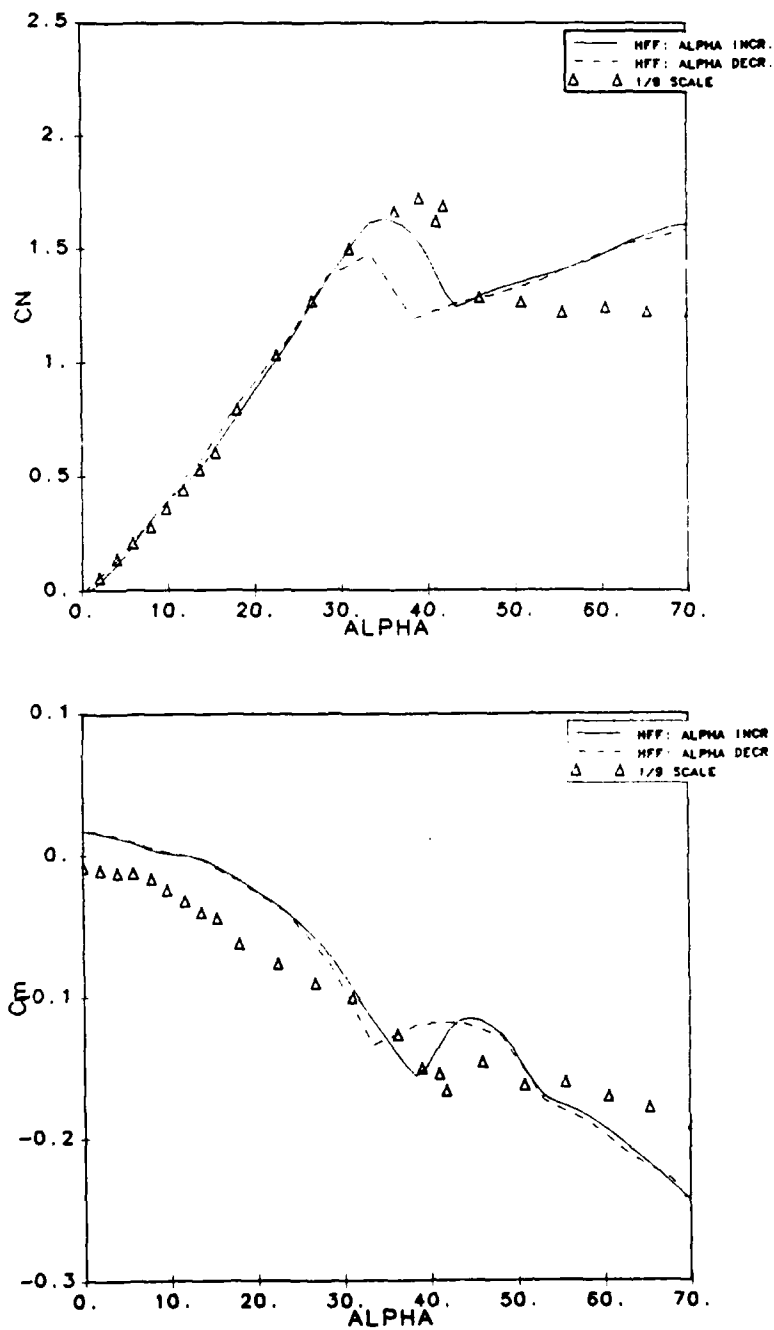


Fig. A-3 Uncorrected HFF Results for the 3-D E-7 Model
as Compared with 1/9-Scale Data (Ref. 10)

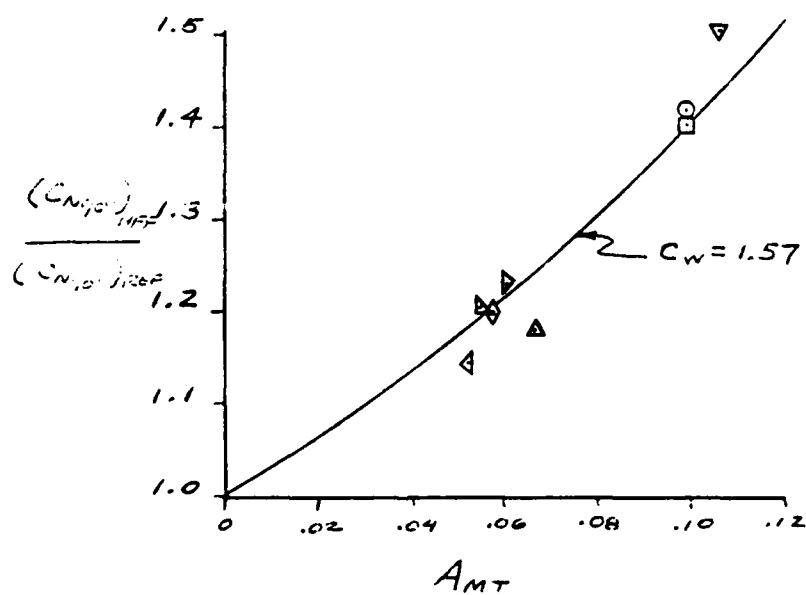


Fig. A-4 Effect of Planform Blockage on Normal Force Measured at 90° in the HFF